Dual-fuel injector design concepts through predictive numerical tools

Marilia Gabriela Justino Vaz

Thesis submitted for the fulfilment of the requirements for the Degree of Doctor of Philosophy

CITY
ST GEORGE'S
UNIVERSITY OF LONDON

School of Science & Technology

Department of Engineering

July 2025

Contents

List of Figures

List of Tables

Acknowledgements

In the first place I want to express my most sincere gratitude and recognition to all who have devoted their lives to education, sharing their knowledge daily without expecting any reward. They are the foundation of our society, shaping character and transforming generations. In special, I would want to express my gratitude to my teacher, Maria Angela, and Prof. Ramon Molina Valle. They made an extra effort to reflect the role of an educator. Without their encouragement, I wouldn't have created a solid foundation for developing this work.

I would like to express my most sincere gratitude to Prof. Manolis Gavaises and Dr. Ioannis Karathanasis for their supervision, support and guidance along the PhD thesis. Through his guidance and remarks, I improved both my personal and scientific skills. Besides, I would like to thank them for the effort for funding acquisition from the European Union Horizon-2020 and coordination of the EDEM project, especially during the Coronavirus pandemic. I would also like to thank Woodward L'Orange for giving the material means to carry out this research.

I am extremely thankful to meet the EDEM Early Stage Researchers (ESRs) that became good friends of mine. Alexander, Hesham, Marija, Mehmet, Rafael, Raffaelle and Onur, a big thanks for all shared moments, support and long talks. This international group enlarged my vision about the world and the combination of different cultures.

I want to express my gratitude to my parents, Oracilia and Ataide, for providing me support and encouragement, without them I would not be who I am today. I would also like to thank my Brazilian friends for their support during the PhD period.

Last, but not least, I am particularly grateful to unfailing support and continuous encouragement from my fiancé Alex. Thank you for all the shared time together during this journey.

Declaration

I hereby declare that the content of this dissertation is original and has not been submitted in whole or in part for consideration for any other degree or qualification in this, or any other university. This dissertation is my own work, except where specific reference is made to a joint effort in the text and accordingly acknowledged. The financial support for the research reported in the dissertation was provided by the European Union's Horizon 2020 research and innovation programme under the Marie Sklodowska-Curie grant agreement No 861002.

Marilia Gabriela Justino Vaz
July 2025

Abstract

The substitution of small-medium sized Diesel engines for dual-fuel operation is one of the strategies for meeting emission regulations. For these engines, fuel flexibility is an important criteria to ensure a reliable operation. However, this leads to some disadvantages related to the injection system complexity because of the need for multiple injectors or a design with multiple nozzles or needles. A single and simple injector capable of precisely delivering fuel across the entire operation range (dual-fuel and Diesel-only modes) is the suitable solution to mitigate those drawbacks and advance the marine engine towards a more environment-friendly operation. However, an optimization process of an injector design is a dependent problem where one universal injector design cannot cover all specific demands of the engine and operation strategies for most of the cases. In this context, the main objective of the current thesis is to enhance and develop numerical tools to support the injector concept design, addressing the operation conditions relevant for fuel flexibility in marine engines. More specifically, the current work proposes models with affordable computational cost to predict in-nozzle cavitation and spray characteristics under non-reacting conditions. Therefore, a thermodynamic closure based on the National Institute of Standards and Technology data base and the Perturbed Chain Statistical Associating Fluid Theory equation of state was incorporated in the computational fluid dynamics model and validated against the experimental data from the Engine Combustion Network. Then, this model has been applied to investigate the potential of needle-tip design and underscore the in-flow conditions of each operation mode. Afterwards, this model was used to generate data for neural networks training, where the needle-tip design, conicity and needle lift are the input parameters to predict performance attributes as single values and in-nozzle cavitation as images. This CFD-assisted machine learning surrogate model demonstrates how those areas could work together for optimization tasks. Finally, an additional deep neural net-

work based on experimental data was trained to predict the spray penetration and cone angle reaching 95% accuracy. This model included 10 geometrical parameters and 3 operation conditions as input features, which differentiate it from current ones found in the literature. Overall, the numerical solutions developed in this work were tailored to support the optimization process of marine Diesel injectors, which contributes to reducing the development cycle and decision-making in the early design phases.

Present Contribution

The novelty of the present work can be summarized in the following points:

- **Potential needle tip shape modifications on in-nozzle flow characteristics for fuel flexibility on marine engines**: this work distinguishes from the previous publications by focusing on needle-tip modification for four-stroke marine Diesel injectors. The proposed needle-tips can contribute to reducing in-nozzle cavitation and to finding a compromise in terms of flow characteristics in order to use a simplified Diesel injector for Diesel-only and dual-fuel operation mode. The results reported here show the in-flow behavior at each mode and a further design insight to achieve a seamless single-injector fuel flexibility.

- **CFD-assisted Machine Learning surrogate modeling framework for cavitation prediction in marine injectors**: leveraging CFD-generated dataset to train machine learning surrogates models allows a reliable assessment of in-nozzle cavitation for marine Diesel injectors in the early design phase. The workflow developed in this study showcases how data pre-processing and appropriate model architectures can predict results similar to the CFD simulations. The image depth reduction from 24 bits to 8 bits has been a pivotal strategy to alleviate structural issues with minimal visual distinction to the human eye. To the best of the author's knowledge, this is the first time that extensive image pre-processing is considered in CFD-driven surrogate modeling framework for reliable assessment of cavitation in marine Diesel injectors.

- **Data-driven prediction of spray macroscopic characteristics based on geometric design parameters and operation conditions relevant for fuel flexibility in marine engines**: the deep neural network presented in this work was trained with experimental data from 27 injector designs in conditions relevant to fuel flexibility. This made it possible to include 10 geometrical parameters in parallel to 3 operation conditions as input features. To the best of the author's knowledge, this is the first time that a model included 10 geometrical parameters to predict spray characteristics. This uniqueness allows their use to on-the-fly explore the design range for marine injectors, which offers an advantage over the current semi-empirical models or neural networks.

- **Industrial impact**: this thesis has an added value during the pre-development injector design phase at Woodward L'Orange. The predictive models developed in this work had their conceptualization based on design parameters, which allow engineers to assess the robustness of the design variations in early design phases. This contributes to forecasting non-intuitive relationships, accelerates the design cycle and lowers development costs. Besides, the time gained allows the CFD simulation to be used more effectively in the later stage and the incorporation of better fluid properties via NIST REFPROP and PC-SAFT EoS increases their dependability.

Throughout my research, the prior contributions have been wrapped in four peer-reviewed publications (newest fist):

- Justino Vaz, M.G., Karathanassis, I., Gavaises, M. and Mouokue, G., "Data-Driven Prediction of Spray Macroscopic Characteristics for Marine Injectors using Neural Networks", Fuel, 2025, doi: 10.1177/14680874251398815.

- Justino Vaz, M.G., Karathanassis, I., Gavaises, M. and Mouokue, G., "Influence of Needle-Geometry Design on In-Nozzle Flow Characteristics for Fuel Flexibility on Marine Engines", International Journal of Engine Research, 2025 doi: 10.1016/j.fuel.2025.136736.

- Justino Vaz, M.G., Geber, E., Koukouvinis, F., Karathanassis, I., Rodriguez Fernandez, C., Gavaises, M. and Mouokue, G., "Numerical Simulation of Multicomponent Diesel Fuel Spray Surrogates Using Real-Fluid Thermodynamic Modelling", SAE Technical Paper 2022-01-0509, 2022, doi: 10.4271/2022-01-0509.

Partial results on the topic of the second paper were presented at an International Workshop :

- Justino Vaz, M.G., Karathanassis, I., and Gavaises, M., ”Impact of Needle Tip Geometry on Pilot Diesel Injection”, 7th Workshop of the International Institute for Cavitation Research (IICR), MAICH Conference Centre, Chania, Greece, 15-16th June 2023.

Nomenclature

Abbreviations

ANN Artificial Neural Network

BD Base Design

CFD Computational Fluid Dynamics

CO_2 Carbon Dioxide

CR Common Rail

CVC Constant Volume Chamber

DBI Diffuse Backlight Illumination

DDI Diesel Direct Injector

DF Dual-Fuel

DFICE Dual-Fuel Internal Combustion Engines

DNS Direct Numeric Simulation

DoE Design of Experiment

ECN Engine Combustion Network

EDA Exploratory Data Analysis

EDEM Experimentally validated DNS and LES approaches for fuel injection, mixing and combustion of dual-fuel engines

EoS Equation of State

FIE Fuel Injection Equipment

GAN Generative Adversarial Network

GM Generative Model

GPU Graphic Processing Unit

HC Hydrocarbon

HEM Homogeneous Equilibrium Model

HFO Heavy Fuel Oil

HPHT High Pressure High Temperature

HRM Homogeneous Relaxation Model

ICE Internal Combustion Engine

LES Large-Eddy Simulation

LHS Latin-Hypercube Sampling

LReLU Leaky ReLU

MAPE Mean Absolute Percentage Error

ML Machine Learning

ML-GGA Machine Learning-Grid Gradient Ascent

MSE Mean Squared Error

NG Natural Gas

NIST REFPROP National Institute of Standards and Technology Reference Fluid Thermodynamic and Transport Properties Database

NOx Nitric Oxides

PC-SAFT Perturbed Chain Statistical Associating Fluid Theory

PCA Principal-Component Analysis

PIML Physics-Informed Machine Learning

PLN Pump-Line-Nozzle

PM	Particulate Matter
POD	Proper Orthogonal Decomposition
QUICK	Quadratic Upwind Interpolation of Convective Kinematics
RANS	Reynolds-Averaged Navier-Stokes
ReLU	Rectified Linear Unit
RGB	Red Green Blue
ROM	Reduced-Order Models
RP	Rayleigh-Plesset
SAFT	Statistical Associating Fluid Theory
SCA	Spray Cone Angle
SGS	SubGrid-Scale
SMD	Sauter Mean Diameter
SS	Schneer and Sauer
SST	Shear-Stress Transport
STP	Spray Tip Penetration
SVD	Singular-Value Decomposition
SVM	Support Vector Machine
TKE	Turbulent Kinect Energy
UDF	User-Defined Functions
UDRGM	User-Defined-Real-Gas-Model
URANS	Unsteady Reynolds-Averaged Navier-Stokes
VAE	Variational Autoencoder
VCO	Valve Covered Orifice
VLE	Vapor Liquid Equilibrium

VV Vapor Volume

VVF VaporVolume Fraction

WLO Woodward L'Orange

XPCI X-Ray Phasecontrast Imaging

ZGB Zwart-Geber-Belamri

Greek symbols

α Volume Fraction

Δ Del Operator

κ Turbulent Kinetic Energy

μ Molecular Viscosity

ρ Density

σ Prandtl number

τ Stress Tensor

ω Specific Turbulent Dissipation Rate

Latin symbols

A Area

c_p Heat Capacity

C_a Area Coefficient

C_c Contraction Coefficient

C_d Discharge Coefficient

C_v Velocity Coefficient

D Diameter

D_m Mass Diffusion Coefficient

D_T Thermal Diffusion Coefficient

E	Energy
F	coefficient
F_1	Model Blending Function
h	Enthalpy
J	Mass Diffusion Flux
k_{eff}	Total Effective Thermal Conductivity
K	K-factor or orifice conicity
L	Length
$\dot{m}_f$	Mass flux
$\dot{M}_f$	Moment flux
n	Number of Samples
n_{holes}	Number of Spray Holess
n_c	Number of concordat pairs
n_d	Number of discordant pairs
P	Pressure
P_κ	Rate of Production of κ
P_ω	Rate of Production of ω
R	Radius
$\mathbb{R}^2$	Coefficient of Determination
S	Strain Tensor Magnitude
S_c	Schmidt number
t	Time
T	Temperature
u	Theoretical Velocity

v Velocity

y_{fuel} Fuel Mass Fraction

Subscripts

a Area

air Air

b Bubble

c Concordant

cond Condensation

d Discharge

d Discordant

eff Effective

fuel Fuel

Holes Holes

in Inlet

l Liquid

m Mass

nuc Nuclei

o Orifice

out Outlet

t Turbulent

th Theoretical

T Thermal

v Vapor

v Velocity

vap Evaporation

Chapter 1

Introduction

This thesis summarizes my contributions as Research Engineer at Woodward L'Orange (WLO) in Stuttgart, Germany, within the Computational Fluid Dynamics (CFD) Team. WLO is a renowned manufacturer and provider of Fuel Injection Equipment (FIE) for large Diesel engines. Their products, most notably Common Rail (CR) systems and Marine Injectors, are utilized in maritime vessels, power generation facilities, heavy-duty vehicles, and many other applications. Throughout my three years at WLO, my research concentrated on enhancing the CFD methodology while minimizing computational costs and providing computational methods to assist the design and optimization of Marine Diesel injectors.

1.1 Background and motivation

Global warming is a major issue of the current century and the transportation sector contributes approximately 24% of carbon dioxide (CO_2) emissions due to the burning of fossil fuels [106]. Moreover, it is also responsible for emissions hazardous to health such as particulate matter (PM) and nitric oxides (NOx) [59]. As a consequence, strict emissions legislations (EURO VI in Europe and Tier IV in US) have been implemented [60, 24], increasing the demand for more environmentally friendly solutions. In order to be compliant with such mandates, there is a strong focus on either hybridizing or fully electrifying engines fed with sustainably gained electric energy. However, electrification is not a suitable option for marine transport and heavy-duty Diesel applications.

The challenges for widespread electrification reside on an intersection of existing marine legislation, technological limitations, and economic considerations [200, 10].

The strict marine safety regulations, which include high-voltage systems, battery energy density, and fire threats, are hindering their adoption [22]. The rising design complexity and price for electric vessels, along with the constraints posed by standardized charging infrastructure and the complexities of international power systems, present obstacles for long-distance electric transport [65, 220]. Hence, replacing conventional Diesel engines with dual-fuel Internal Combustion Engines (DFICE) is a practical and viable solution complying with regulatory emissions requirements in the marine sector [63].

In DFICE strategy, the primary fuel with a high-octane number provides most of the energy power. Natural Gas (NG) [64] and Hydrogen are potential options to partially replace Diesel fuel in DFICE as primary fuel, being a promising approach with respect to energy conversion efficiency, power density and pollutant emission behavior [59, 94]. The secondary one, usually Diesel in small amount, acts as an ignition source, also termed as pilot injection. Conversely, even not being a new technology, DFICE still raises important questions due to the heterogeneous character of the entire process [73].

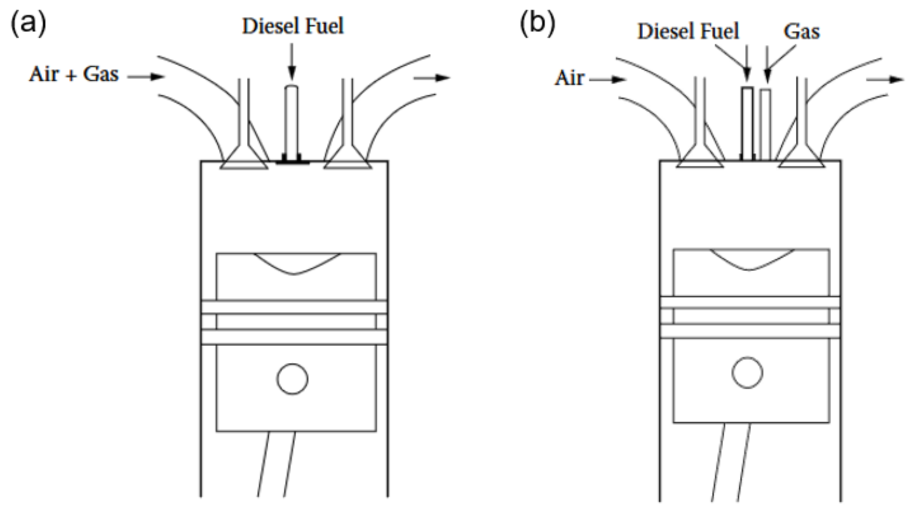

Figure 1.1: Schematics of mixture formation for dual-fuel applications: (a) External mixture formation, (b) Internal mixture formation [111]

The DFICE operation can be categorized based on the mixture formation as internal and external as illustrated in Figure 1.1. In the case of external mixture formation (Figure 1.1a), a mixture of air and fuel gas is admitted during the intake phase, with the fuel gas being introduced in the intake system via a central mixture formation or port fuel injection. For internal mixture formation (Figure 1.1b), only air is admitted during the gas exchange phase, and the gas and Diesel fuel are injected directly into the combustion chamber. In both cases, the gas/air mixture is ignited by the compression of the small Diesel amount.

These configurations of DFICE present the challenges in the employment in marine engines. In parallel, only a partial replacement by DFICE is presently feasible, since fuel flexibility is still an important criterion to ensure reliable operation. Currently, maritime vessels primarily operate using either Diesel-only or in a dual-fuel mode with a gas fuel as primary fuel [248]. This allows, under certain conditions, a smooth transition between the two modes while the engine is running [283]. This versatility provides safe operation in case of issues during dual-fuel operation, such as abnormal combustion but also facilitates the compliance with emission regulations in control areas and the fuel selection according to cost and availability [274, 282].

This fully flexible configuration imposes constraints related to the injection system complexity [206]. Specifically, it requires the use of multiple Diesel injectors, with at least one being located in a decentralized manner in the combustion chamber [284], or an injector with a complicated geometric design featuring multiple nozzles or needles [61]. The optimal solution would be a single and simple Diesel Direct Injector (DDI) that efficiently delivers fuel for the entire range of engine operations. This includes delivering small quantities for dual-fuel mode and larger quantities for Diesel-only mode. This dual requirement poses challenges in terms of injector design, cost and durability. Although it is possible to utilize the same Diesel injector for both modes, it is still necessary to carefully evaluate and optimize the injector performance and flow capacity for each mode [218].

In the last three decades, extensive research has been carried out to elucidate in-nozzle flow during fuel injection. Experiments can provide a representative visualization of the two-phase flow field within real geometries or transparent nozzle replicas. However, those measurements are quite challenging at high pressure/temperature conditions, with only a limited number of studies in the literature. CFD simulations can provide complementary information under realistic injection conditions. Nonetheless, numerical simulations can be computationally demanding and time-consuming, particularly for high-fidelity approaches [5].

In this respect, the integration of Machine Learning (ML) into the injection design process is a feasible aid for accelerating and enhancing the numerical capabilities by learning from experimental data and CFD simulations. In summary, an assortment of predictive and efficient numerical methods are indeed required for further development of injectors, especially for improving the single and simple injector design for higher efficiency in Diesel-only and dual-fuel mode. Therefore, this thesis aims to develop support tools for the pre-development design phase of marine injectors.

1.2 State-of-the-art

The prediction of Diesel injector performance involves phenomena with different spatial and temporal scales. The internal flow structures, such as flow separation and cavitation, determine the hydraulic performance and strongly influence the subsequent spray atomization process. And both internal and external flow are mainly defined by the operation conditions and geometric design parameters. Although considerable advances have been achieved in injector modeling via CFD simulations and experimental diagnostics, those methods can be time and/or resource consuming. As a consequence, a rapid prediction of the relationships between injector design, internal flow physics and external spray behavior still remains an open challenge. Therefore, this section reviews the current understanding of the governing physical mechanisms, the numerical approaches used to model them and recent developments in ML.

1.2.1 Diesel injectors and nozzle design parameters

Marine engines are commonly designed to operate in Diesel-only or dual-fuel mode in order to ensure fuel flexibility and a safe operation in the event of a gas supply failure. In principle, two Diesel injectors or complex Fuel Injection Equipment (FIE) are required to introduce both the pilot and full-load fuel quantities into the combustion chamber. Figure 1.2 shows a comprehensive concept overview of the dual-fuel configuration for the Diesel injection. The double injector configuration (Figure 1.2a) requires two Diesel fuel systems and imposes significant design effort to place both injectors in the cylinder head. They may utilize the existing Pump-Line-Nozzle (PNL) or Common Rail (CR) system, allowing more flexibility in the system configuration. Since a compact and symmetrical injection is preferred, their combustion process is a compromise between the two systems, in which one mode is penalized with a decentralized nozzle position [208].

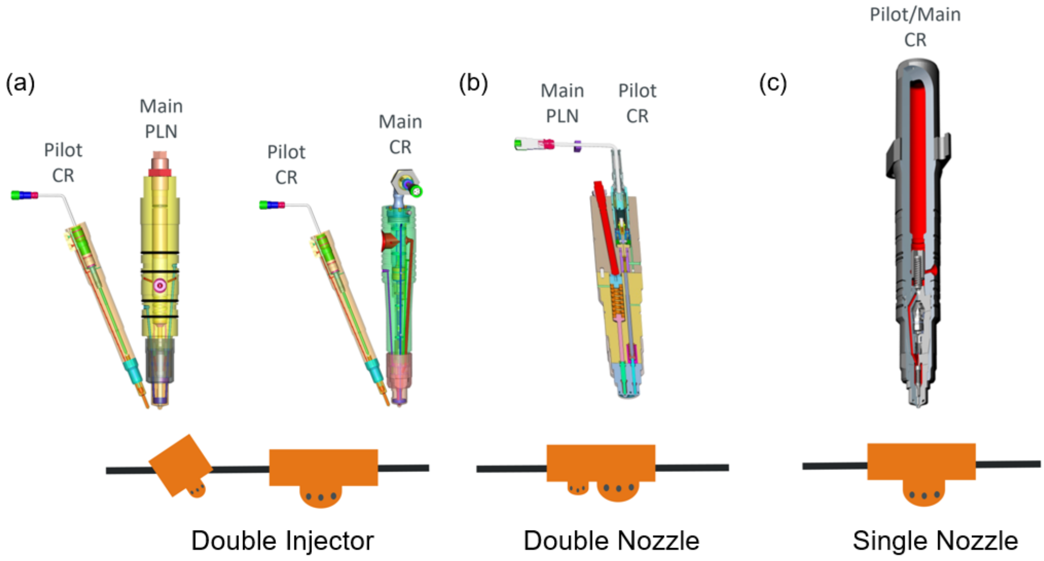

Figure 1.2: Diesel injectors arrangements for the integration of Diesel-only and dual-fuel modes: (a) Double injector, (b) Double nozzle, (c) Single nozzle

In case of a double nozzle (Figure 1.2b), a complex injector system is required to operate two needles and as consequence, this increases the injector housing and nozzle diameter in the cylinder head. Normally, this configuration conjugates the PNL and CR system. Since both nozzles are better centrally placed, the pilot injection and main injection are optimized for an efficient combustion which is better than the double injector. Nevertheless, an elegant option is the single nozzle with one nozzle and needle (Figure 1.2c), which simplifies the FIE, reduces weight and volume, and potentially lowers costs. It does not require additional effort for placement in the cylinder head and can use the CR system. The central position allows a fully symmetric combustion process, being a wide range injector concept.

However, this injector architecture presents technical challenges due to the significant differences in injection and flow characteristics between the two modes [40]. Precisely metering both large and small fuel quantities can be difficult, increasing the risk of nozzle clogging and emphasizing the necessity to compromise spray characteristics, particularly at low flow rates. In order to accomplish fine atomization and proper mixing with the gas fuel, dual-fuel operation often necessitates higher injection pressures in comparison to the Diesel-only mode. Nevertheless, the same injector needs to handle the pressure requirements of Diesel-only mode while maintaining optimal performance.

The injector nozzle is the interface between the injection system and the combustion chamber, playing a decisive role in the emission and power trade-off. In

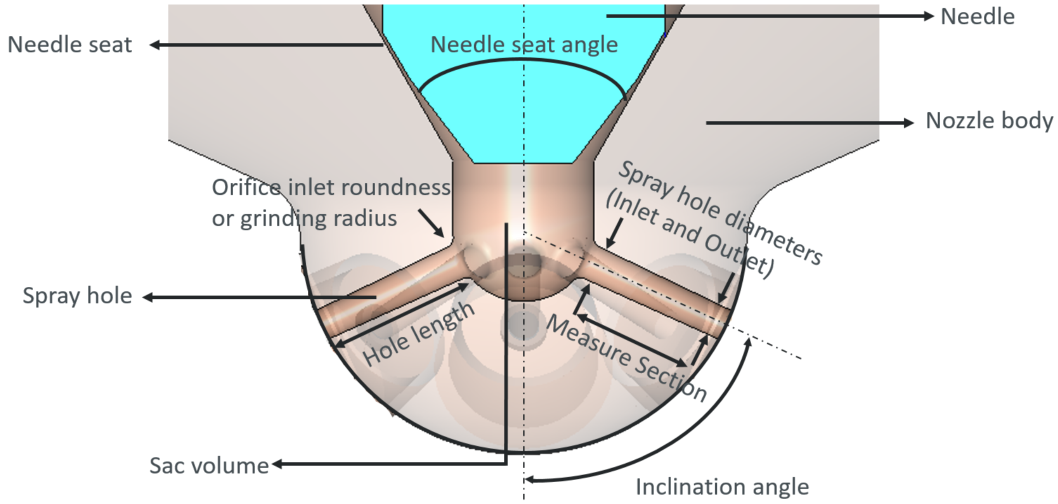

Figure 1.3: Schema of injector nozzle, needle and their main geometrical features

its base configuration, as shown in Figure 1.3, dynamics and operation conditions have a crucial role on cavitation and spray characteristics. The understanding of the nozzle geometry influence and its link to cavitation is a key point to mitigate the current issues with a single nozzle for marine fuel flexibility.

The geometry of the needle seat, needle-tip, needle lift and the inlet of the spray hole alter the internal flow, can constrict the effective flow passages and as a consequence, increase the flow velocity [273]. The flow restriction at the needle seat exerts a minimal influence in comparison to the spray hole diameter during maximum needle lift, particularly under prolonged injection duration with rapid opening times in marine injectors [81]. The larger flow passage and smoother flow path lead to reduced velocity gradients and low impact in case of needle eccentricity. As a consequence, the flow presents a more uniform distribution of flow across the spray holes, which contributes to a more symmetrical and stable spray pattern [105].

In contrast, at low needle lift, the flow experiences significant velocity gradients due to the restricted passage. High velocities and pressure differentials near the solid wall lead to cavitation, particularly near the spray hole inlet [48]. Consequently, the flow may not be uniformly distributed through the orifice, which could result in a non-uniform spray pattern. The needle movement also causes significant changes in mass flow rate and can create hysteresis effects, with pronounced differences in the flow structure compared to high needle lifts [38, 309].

The effective volume of the sac hole also plays a role in vortex formation, cavitation and unsteady flow [7, 38]. A larger sac tends to have a more stable flow with less turbulence due to the pressure fluctuations dampening [155]. However, the larger sac volume might lead to the remaining fuel slowly dripping out into the combustion chamber after an injection event and contributes to an increase of hydrocarbon emissions [121].

Therefore, efforts have been made to reduce the existing sac hole volume [225, 148]. A smaller sac volume creates a more confined flow path, accelerating the fuel through confined passages. However, it also might lead to more localized and intense cavitation near the needle seat [155]. It also makes the design susceptible to flow fluctuations, manufacturing tolerances and needle misalignment [71]. The sac type directly influences the internal flow structure and the presence of string cavitation can lead to a more dispersed spray with a wider cone angle and finer atomization [93].

The spray hole diameter directly controls the fuel quantity delivery and a four-stroke marine injector often presents a layer of spray holes normally distributed along the nozzle axis. The multi-hole injector can contribute to a complex flow structure inside the sac hole due to the spray hole interactions [7]. Larger spray hole diameters usually result in increased spray penetration and mass flow rate [296, 222]. However, they can also lead to coarse spray droplets and promote a less effective fuel mixing. On the other hand, smaller diameters often produce finer droplets and widen the spray cone angle. Those factors promote a better air entrainment and atomization process for Diesel injection [178]. The design of the spray hole diameter is always a balance between fuel delivery and spray flow characteristics. While reducing the spray hole diameter can contribute to reduce cavitation, excessive small diameters may over-constrain the flow and limit the injection rate.

The grinding radius and spray hole shape support balancing the diameter effects and cavitation control [232]. The degree and quality of grinding largely determine the degree of flow separation and the pressure loss coefficient in the spray hole inlet, being crucial for cavitation and hole to hole variations [52]. The fillet radius is an important manufacturing parameter and it is often shaped by hydro-erosive grinding [145].

The taper ratio of the spray hole inlet to the outlet can contribute to mitigating the geometric cavitation [70]. This ratio is known as K-factor (K) or orifice conicity. Nozzles exhibiting higher conicity tend to reduce turbulence and cavitation within the spray hole in contrast to cylindrical (straight) designs [252]. They also tend to increase the discharge coefficient and flow area [184], but these factors can be affected by other design parameters. However, the geometric cavitation commonly present in cylindrical spray holes aids in removing the injector deposition, which can impact on the injector performance, increase emissions and lead to injector failure in extreme cases [17, 148]. The K-factor can be mathematically defined in terms of the inlet diameter D_{in} and outlet diameter D_{out} of the spray hole as illustrated in Figure 1.3 and Equation 1.1:

$$K - factor = \frac{D_{in}[\mu m] - D_{out}[\mu m]}{MeasureSection[mm] * 10} \tag{1.1}$$

As described in this sub-chapter, previous investigations have establish the influence of individual geometrical parameters on in-nozzle flow and hydraulic performance. However, most studies analyse these parameters independently and under specific operating conditions. As a consequence, the understanding of the combined influence of injector nozzle geometry on the resulting internal flow structures remains relevant for marine injectors operating under both Diesel-only and dual-fuel conditions.

1.2.2 Cavitation and compressibility effects

Cavitation in Diesel Injectors

The rail pressure of the Diesel direct injection system has exceeded 250 MPa, with projections indicating potential increases up to 350 MPa to enhance engine performance and compliance to emissions regulations [293]. This strategy poses challenges for the design of injectors in Diesel engines and DFICE applications. High-pressure gradients induce flow acceleration and, in combination with changes in flow direction, generate low-pressure regions and recirculation zones within the injector internal flow. When the liquid fuel pressure decreases below the saturation pressure, a phase transition from liquid to vapor occurs and bubbles appear as a macroscopic indication of liquid breakdown or cavitation [128].

Cavitation in Diesel injector nozzles manifests in two principal forms: string cavitation and geometrical-induced cavitation, as depicted in Figure 1.4. String cavitation consists of filament-like vortical formations that can substantially modify flow conditions, particularly at low needle lifts, resulting in enhancing the spray angle due to the helical flow [7]. Geometrical-induced cavitation is generated due to the abrupt changes imposed by injector nozzle design on the flow such as entrance corner radius and spray hole diameter [187]. It is commonly appearing as a film-like sheet cavity and this cavitation form is more stable and less influenced by operational conditions [250].

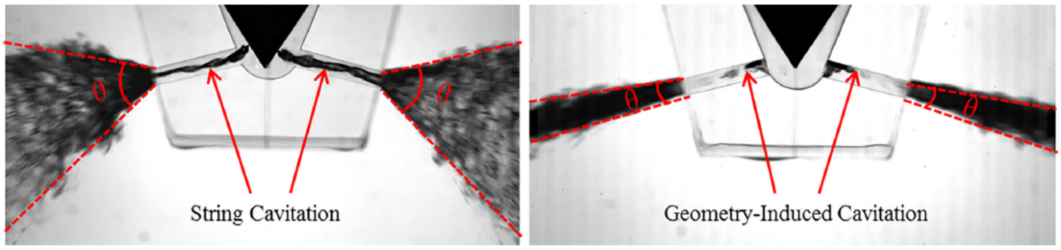

Figure 1.4: Experimental images of cavitation patterns in a transparent nozzle: string cavitation (left) and geometry-induced cavitation (right) [33].

Cavitation in fuel injectors can both enhance and decrease performance. Bubbles contribute to variations in fuel delivery from cycle to cycle [156] and cavitation bubbles within the spray hole may enhance the spray cone angle and velocity coefficient [184]. The collapse of these bubbles at the spray hole exit enhances the primary break-up and subsequent atomization, as well as the spray cone angle [185]. Nonetheless, their collapse near solid surfaces releases energy that can inflict damage on the injector walls, lead to erosion, and in severe situations, deterioration of injector performance and eventual injector failure [123].

Advances in numerical modeling and experimental techniques have improved the understanding of cavitation dynamics, aiding in the design of more efficient Diesel injectors. Experimental studies often utilize transparent nozzle replicas in real-size or enlarged nozzles combined with advanced imaging techniques to directly observe cavitation inside Diesel injectors. Gavaises et al. [72][70] used high speed imaging visualization to characterize the cavitation structures inside an enlarged transparent Diesel injector with different shapes of injector holes. Cavitation images of VCO nozzles with tapered and cylindrical spray holes were acquired, where the string cavitation is completely eliminated in tapered nozzles at high needle lift as pressure inside the injector spray hole does not fall below the saturation pressure. Cao et al. [33] also used high speed imaging to characterize string and geometry-induced cavitation in the transparent nozzle. Karathanassis et al. [110] combined Diffuse Backlight Illumination (DBI) and Schlieren imaging to visualize the in-flow for Engine Combustion Network (ECN) spray D [57]. A mild cavity sheet was detected in this single-hole transparent nozzle. However, the spray cone fluctuation and the highly-transient Schlieren structures, which were caused by density gradients, were well depicted in this study. Furthermore, Tekawade et al. [254] utilized X-ray tomographic reconstruction to visualize the two-phase flow inside ECN spray C [57] at engine-like operation conditions. They observed that geometric-induced cavitation raised in ECN spray C mainly in regions of manufacturing imperfections.

Concerning the phase change modeling, two main approaches are available in the literature, each with distinct methodologies and applications. The first one is the non-equilibrium models, solving one or more transport equations for the volume fraction. The Schnerr and Sauer(SS) [233] and Zwart-Gerber-Belamri (ZGB) [307], for example, account for the cavitation process by modeling the mass transfer between liquid and vapor phases; a simplified Rayleigh-Plesset (RP) equation estimates the phase change rate. The Homogeneous Relaxation Model (HRM) [25] accounts a finite rate of phase change, assuming a finite relaxation time of the vapor fraction towards its equilibrium value. The second group of the models is based on thermodynamic equilibrium considerations of the liquid-vapor mixture, where the phase change has a negligible time scale, depending only on the thermodynamic state. The Homogeneous Equilibrium Model (HEM) is one representative example, where thermal equilibrium between liquid and vapor is assumed. One drawback of those models is associated with the tuning of constants based on the conditions or configurations.

Battistoni et al. [19] studied the effects of needle off-axis motion and in-nozzle flow for a mini-sac Diesel injector. The mass exchange was modeled based on a HRM and included the non-equilibrium flash boiling process. Koukouvinis et al. [123] investigated the erosion inside Diesel injectors due to cavitation. The mass transfer rates for condensation and evaporation were covered via ZGB model. The vapor/liquid mixture was treated as compressible due to the mass transfer term and the fuel viscosity and density described as function of pressure via Tait Equation of State (EoS). Cristofaro et al. [42] modeled the cavitation erosion with a two-phase model Eulerian approach. A non-equilibrium mass transfer model, which was derived from a simplified version of the RP equation for the single bubble dynamics, was implemented in the commercial CFD solver AVL FIRE. Santos et al. [76] investigated cavitation and air entrainment during pilot injection of Diesel injector nozzles using the ZGB cavitation model. The liquid phase is modeled as compressible phase based on the calibration oil ISO4113 measurements. The simulation was able to replicate the main flow features, which were observed experimentally, with good quality, such as sac flow recirculation and voids due to geometrical and vortical cavitation.

Another important aspect of cavitation modeling is turbulence, since both mutually affect each other. Turbulence is associated with chaotic and unsteady fluid motion with high Reynolds numbers. It involves a wide range of interacting eddies, from large energy-containing scales of fluid motion down to very small dissipative scales, where energy is dissipated due to viscous effects [266]. Design features can increase the turbulence, especially near walls, raising local shear stress and turbulent kinetic energy. As a consequence the local pressures can drop, promoting cavitation inception and growth [124]. On the other hand, the formation and collapse of cavitation bubbles introduce unsteady, small-scale turbulence and disrupt established flow patterns. Those collapse events, especially during needle closing, generate additional turbulence and pressure waves [309].

Accurately modeling those phenomena requires models that properly capture both turbulence and cavitation effects. Large Eddy Simulation (LES) predicts the unsteady dynamics and detailed features of cavitating flows, resolving large and small scales below the mesh resolution (sub-grid scales) [292]. However, the elevated computational cost required to achieve this higher spatial and temporal resolution make this model impractical for industrial research-and-development time-frames [188]. Unsteady Reynolds-Averaged Navier-Stokes(URANS) extends the Reynolds-Averaged Navier-Stokes (RANS) turbulence models by solving the equations in an unsteady (time-dependent) manner, allowing for some large-scale, low-frequency unsteady flow features to be resolved. Their accuracy to predict cavitation in high-pressure operation conditions has been improved due to the integration of enhanced models such as density-correct, multi-phase and mesh refinement to capture the small-scale cavitation structures [58, 123]. Those modifications offer a practical compromise for accuracy and computational cost, making them highly suitable for industrial engineering applications [124].

Therefore, the selection of a cavitation model is not only a question of prediction accuracy but also a balance between computational efficiency and intended application. The same applies for turbulence modeling. LES provides a detailed information about turbulence interactions by resolving large and small scales. However, it remains computationally demanding for industrial design optimization studies. On the other hand, URANS approaches offer a practical compromise and reduce the computational cost. Nevertheless, they inevitably rely on modeling assumptions regarding turbulence closure and phase change, where better fluid properties description could enhance these modeling approaches. As a consequence, CFD simulations suitable for injector optimization must balance physical fidelity and computational affordability. To this end, surrogate models derived from CFD simulations could be a complementary alternative for enabling rapid design-space exploration during the early stages of injector development.

Compressibility modeling

At high injection pressures the variation of the fluid properties cannot be neglected and the liquid phase should be treated as compressible. Modelling the fuel as compressible fluid is normally linked with the increase of computational cost. The Barotropic model is largely applied at those conditions [309]. However, it may lead to deviations since the liquid density variations are only modelled as a function of pressure [203]. As the pressure drops, the fuel expands, which induces cooling due to the Joule-Thomson effect. In addition, shear stresses cause fuel heating, which make it relevant to calculate the fuel property variations as a function of pressure and temperature [122].

In order to properly capture properties variation, real-fluid EoS need to be considered. The Cubic EoS family, including the Soave [243] and Peng-Robinson models [191], has been commonly employed due to the trade-off between computational efficiency and accuracy [279, 290]. The Cubic EoS formulation extends the ideal gas law by including elements that account for intermolecular forces, specifically the Van der Waals dispersion forces. Their precision decreases in conditions with strong association between molecules and under high pressure and high temperature (HPHT) [261, 177]. However, despite their compromised accuracy, they are frequently adopted due to their low computational cost [290].

The Statistical Associating Fluid Theory (SAFT) is one alternative for high pressure/temperature conditions, addressing various intermolecular interactions such as dispersion, association, and chain formation by incorporating the Helmholtz free energy contribution into its formulation [36]. Within the SAFT framework, the Perturbed Chain Statistical Associating Fluid Theory (PC-SAFT) EoS is the most prominent variant, wherein the Helmholtz free energy term is utilized for hard spheres [80]. Consequently, PC-SAFT predictions exhibit more accuracy than Cubic

EoS regarding thermodynamic and transport fuel properties [192]. However, they are also more computationally demanding than Cubic EoS [279].

In order to reduce the calculation time and save computational cost, tabulated methods are common techniques applied in fluid dynamic simulations [131, 216]. This method involves pre-calculating thermodynamic properties for a range of temperatures and pressures and storing them in a look-up table. Vidal et al. [267] analysed the effect of high pressurization on the cavitation development for a 8-component Diesel fuel surrogate, comparing two fluid properties models: Batotropic and PC-SAFT EoS. The tabulated approach was used for the PC-SAFT EoS modeling, incorporating the Vapour-Liquid Equilibrium calculations to cover the preferential cavitation of the fuel components. The inclusion of thermal effects improved the simulation accuracy, allowing to identify the tendency of lighter Diesel components to cavitate more than the heavy ones. Rodriguez et al. [214, 213] computed the thermodynamic properties of four multi-component Diesel surrogates with air mixing at temperatures typical for high pressure injection systems using PC-SAFT EoS. They were able to simulate transcritical and supercritical Diesel injection in a compressible density-based solver with high accuracy.

1.2.3 Machine Learning and CFD

Machine Learning in fluid dynamics

CFD has been continuously growing and becoming more affordable to support numerical modeling in industrial applications. However, it still has room for improvement, especially in areas for turbulence modeling, multiphase flows and numerical methods [217]. The elevated computational resources and computational time represent the biggest challenge to resolve the smallest spatiotemporal features in high fidelity simulations. Therefore, reducing the computational cost while generating fast and accurate results is a crucial aspect across many fields of science and engineering.

Even an exponential growth of computational power will not reduce this need and alternative solutions have gained attention in the last years [165]. Simplified models, ML techniques and hybridized models become an attractive perspective to accelerate the CFD simulations. ML is a branch of artificial intelligence focusing on algorithms capable of learning from data. They can be mainly classified in four categories in terms of learning process: Supervised learning, Semi-supervised learning, Unsupervised learning and Reinforcement learning [74].

In the Supervised learning the algorithm learns from labeled data to predict outcomes or classify data, in opposition to Unsupervised learning where the goal is to find patterns or groups in unlabeled data. The Semi-supervised learning is a bridge between the two previous approaches that uses a mix of labeled and unlabeled data for training. Finally, in Reinforcement learning, the algorithm learns by interacting with an environment and receiving feedback (rewards).

Various ML algorithms are present in the literature, including Random forest, Support Vector Machine (SVM), Decision trees, Gaussian process regression, K-nearest neighbor, k-means and Artificial Neural Networks (ANNs). There is not an universal algorithm because the optimal choice depends on the specific CFD application and data characteristics [181]. However certain models such as ANN consistently show strong performance in CFD applications due to their capability of highly non-linear predictions [68]. This preference is partly a result of advancement in computational power, especially regarding graphics processing units (GPUs), which contribute to the neural network handling large data sets.

Those learning processes have been used widespread across fluid mechanics research in the last years and can be summarized in three main areas [268]. Accelerating Direct Numerical Simulations (DNS) is the first relevant area, where surrogate models substitute or enhance CFD tasks to reduce the execution speed and/or resource consumption. Deep learning has been used, for example, to estimate spatial derivatives in coarse-grid resolution [16], improve fifth-order finite-difference schemes [247] and solving Poisson equation in incompressible flows [256][235].

Turbulence modeling is the second one, which focuses on improving the accuracy of RANS and LES. In particular, many studies have applied ML models to directly model the Reynolds stresses anisotropy tensor [137], correction factor for the turbulence production [302], mean-flow features reconstruction [67][88], closure of subgrid-scale (SGS) stress [153] and other applications. The third area is the low-fidelity representation of complex flows via Reduced-order models (ROMs). Proper Orthogonal Decomposition (POD), Principal-Component Analysis (PCA) and Singular-Value Decomposition (SVD) are common techniques applied in combination with data-driven models [144]. They construct a set of orthogonal basis functions or modes to capture the most important dynamics or features of a high-dimensional system [30].

Learning from data offers transformative benefits to reduce the computational cost of CFD simulations. However, the efficient couple work is still challenging and in some points unclear. Critical thinking is necessary since those algorithms will always provide an answer based on the input data independent of the relevance of the data for the proposed task. Hence, coupling CFD-ML imposes concern about reliability, generalization and the need for careful validation.

Purely data-driven ML models often struggle with extrapolation, error accumulation in time-dependent simulations, and handling turbulent flows. They normally require large, high-quality datasets for training, which can be expensive to generate [86]. Physics-informed ML (PIML) incorporates physical equations during training, which results in more stable and data-efficient predictions [236]. Despite the advantages, the evaluation of high-order derivatives leads to performance loss and solvability issues, making this field of ML not mature enough to handle real-world problems [39]. Hence, traditional CFD remains essential for accuracy and reliability for highly complex, turbulent, or novel flows, with ML best used as a complement rather than a full substitute.

ML-CFD integration has less impact on computational times while enhancing robustness and generalization. This integration can support the turbulence modeling through the optimization of model coefficients [291, 135], learn closure terms [260] or source [56] terms and, inserted into CFD solvers, accelerate RANS convergence [180] and wall models for LES [143]. They also have been applied to automatic mesh generation [303], optimization of mesh adaptation [280] and estimating boundary conditions [69].

An alternative strategy is not only the integration of ML-CFD to accelerate the numerical solver but also as data generator. The CFD simulations provide detailed descriptions such as velocity distributions, cavitation morphology and hydraulic characteristics. This numerical results can be used to train surrogate models preserving information about the dominant injector physics. Such workflow combines the predictive capabilities of CFD simulations with the computational efficiency of ML, where this association could enhance design optimization studies. Despite its potential, the CFD-assisted ML models have not been fully investigated for marine Diesel injectors. This is mostly due to possible challenges regarding dataset generation, generalization and possible dimensionality discrepancy between input and output parameters.

Generalization and data set size

Generalization is the ability of ML models to make accurate predictions or decisions on unseen data after being trained on a specific dataset by applying the learned patterns. The most generalizable or best accuracy model is a balance between two sources of error: bias and variance as illustrated in Figure 1.5. Bias is an error from incorrect assumptions in the learning algorithm. High-bias models are missing important patterns and tends to underfitting the training data. In contrast, variance relates the excessive sensitivity of the model to small fluctuations, introducing false relationships due to increased fitting of the noise as well as real trends [29]. This high degree of flexibility is connected to high variance, where the model overfits the training data and at the same time underperformes on unseen ones.

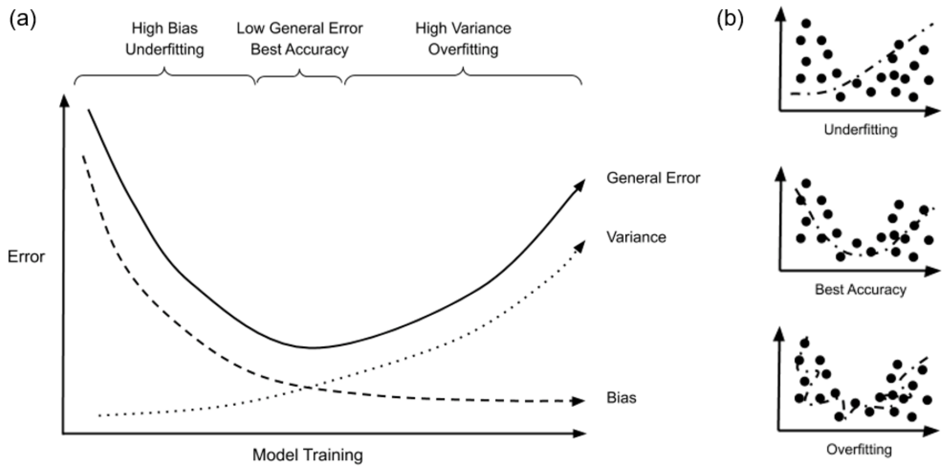

Figure 1.5: Bias-variance tradeoff in Machine learning models (b) Illustration of underfitting, best accuracy and overfitting the training data [41][204].

In general, complex models (more layers, parameters, or capacity) raise the risk of overfitting, while low complexity leads to underfitting. Furthermore, the training data must be both representative in terms of relevant features and covering the solution space. Increasing training size only improves generalization to a certain limit. Moreover, training data is limited in certain cases and Regularization techniques are essential for improving generalization. They prevent overfitting by adding constraints or penalizing model complexity (like weight decay, dropout, and early stopping), which discourage it from fitting noise in small datasets and promote a more generalizable solution.

Training on a limited number of training data points has been the subject of some studies. Badra et al. [13] used a Machine Learning-Grid Gradient Ascent (ML-GGA) approach to optimize a piston bowl geometry. The calculations from the CFD model were used as ML-GGA training data and the best designs identified by the ML-GGA were calculated via CFD. This loop was repeated until it achieved convergence. They also analysed the cross-validation error as function of the size of the training data, where 56 training cases gave the maximal acceptable error. Porch et al. [194] tested and validated three machine learning methods to optimize a large gas engine pre-chamber design: Random forest, SVM and ANN. The variation of six design parameters was done via CFD simulations. The models were capable to predict the behavior of engine pre-chambers and the ANN presented the highest prediction accuracy among the models analysed.

Koukouvinis et al. [125] investigated a numeric parametric variation of the operations conditions of Spray A from ECN, with a total of 20 CFD cases. This matrix of cases was used to train an ANN to predict the time evolution of the spray and its macroscopic characteristics. Mondal et al. [158] explored the influence of the needle lift, dynamic viscosity and level of non-condensable gas on the injection condition. Their combination generated a matrix of 60 cases, which were calculated via CFD for in-nozzle flow and spray modeling. The in-nozzle flow data was used to train a DNN to predict the flow field at the nozzle exit, generating a boundary condition for the spray modeling.

1.2.4 Spray macroscopic characteristics prediction

The traditional methods for predicting Spray Tip Penetration (STP) and Spray Cone Angle (SCA) often rely on empirical correlations and semi-empirical models due to their simplicity and moderate accuracy. In contrast, CFD simulation offers detailed physical modeling, capturing complex spray dynamics. However, they are very sensitive to model settings and mesh quality, requiring significant computational resources. ML models have been emerging as an alternative solution due to their consistently higher accuracy and better generalization than empirical formulas and less computational demand than CFD simulations. A common characteristics of both semi-empirical correlations and existing ML models is the limited inclusion of geometrical parameters for predicting the spray development. As a consequence, the use of the current models for design optimization studies are very restricted.

Brief overview on semi-empirical spray penetration models

Wakuri et al. [269] and Dent [46] were among the first to establish semi-empirical models utilizing experimental data to establish a foundational knowledge of spray penetration. Wakuri et al. [269] derived a spray penetration correlation utilizing the moment theory. Their formulation defined penetration as a function of the spray angle and the square root of the product of the spray hole diameter and time. Dent [46] maintained square root dependence and incorporated the effects of both evaporating and non-evaporating conditions in his formulation by considering the ambient temperature.

Hiroyasu and Arrai [97], along with Naber and Siebers [167] progressed the research, and their contributions can be classified as classical models. Hiroyasu and Arrai [97] presented a more advanced methodology by categorizing the formulation of spray penetration into two separate regions: pre-break-up and post-break-up. Their formulation was based on experimental data and Levich's jet disintegration theory and continues to serve as a foundation for numerous enhanced models. Naber and Siebers [167] significantly modified the Wakury et al. [269] formulation together with Hiroyasu and Arrai [97]. They established a correlation for non-vaporizing spray penetration based on a theoretical model derived from penetration time and length scales. Their correlation considers factors like ambient gas density and injection pressure. A significant contribution of their study is the inclusion of a term related to the injector opening time, which influences the initial penetration and enhances predictions in the near-nozzle region.

Similar to Hiroyasu and Arrai, Desantes [47] categorized the Diesel spray penetration into two distinct regions, presenting a formulation based on basic fluid dynamic principles and dimensional analysis. Their model takes the impact of parameters such as ambient gas density, injection pressure, and nozzle equivalent diameter on spray penetration into consideration, while also taking the spray cone angle and its effect on penetration length into account.

For large marine-type injectors, Najar et al. [170] proposed a model correlating the spray penetration as a function of the cumulative injected mass, providing an alternative viewpoint to conventional time-dominated studies. Zhang et al. [298] also provided a formulation specifically tailored for large-sized injectors. They developed updated correlations for the model proposed by Hiroyasu and Arrai [97]. These correlations take variables such as ambient gas density and temperature, which are essential for marine engine applications into account.

In summary, typical parameters among these formulations often incorporate injection pressure (or a related metric such as momentum flux), nozzle orifice diameter, and ambient gas density. However, they remain limited in applying more geometrical factors to their formulation. These shared parameters reflect the fundamental physical factors influencing spray development, such as the initial momentum of the fuel jet, the resistance imposed by the surrounding gas, and the duration of injection.

Brief overview on semi-empirical spray angle models

Similar to the spray penetration, early models for spray cone angle often relied on simplifying assumptions, for example treating the spray as a solid cone with a constant angle. As experimental data became more accessible, researchers began to integrate empirical correlations. Wakuri et al. [269] incorporated elements of both empirical correlations and moment theory in their formulation, where the ambient gas density has a significant impact on the spray cone angle.

The work of Reitz and Bracco [209] may not provide an explicit formula for the cone angle. However, their research frequently emphasizes the interaction among liquid jet instability, aerodynamic forces, and droplet formation, which together influence the overall spray shape and dispersion. Thus, establishing a fundamental comprehension of the mechanisms that control spray formation and development, which subsequently affect the resulting cone angle. Varde et al. [264] have enhanced the comprehension of spray behavior, specifically the impact from nozzle geometry, using the spray hole length and diameter ratio L/D. These investigations frequently study the correlation between spray angle, injection pressure, orifice dimensions, and the characteristics of both the liquid and the surrounding gas.

The formulation of Hiroyasu and Arai [97] is a part of a more comprehensive model that also incorporates STP. However, they proposed a simplified model that assumes a constant spray cone angle prior to the primary breakup of the spray. Naber and Siebers [167] provide insights into the relationship between the spray cone angle and other spray characteristics. Although they do not offer a specific formula for the cone angle, their research establishes a framework for comprehending its correlation with spray penetration and dispersion, especially in connection to gas density and vaporization effects. According to Arrègle et al. [12], the spray cone angle is affected primarily by injection pressure, ambient gas density, spray hole geometry (length and diameter), and needle lift. Unlike earlier investigations that prioritized the spray hole diameter as the most relevant geometrical parameter, they found that spray hole length-to-diameter ratio was the significant geometric parameter in their study.

Overall, parameters which are commonly evaluated in these formulations typically include injection pressure, spray hole geometry (diameter and length or related ratios), and the density ratio between the fuel and the surrounding gas. Moreover, backpressure is a critical factor in these formulations, as it influences the penetration and dispersion of the spray. Nevertheless, the specific dependencies and exponents in these correlations may vary, reflecting differences in experimental setups, measurement techniques, and the conditions investigated.

Brief overview on spray characteristics prediction via machine learning

ML models can predict spray penetration and cone angle by learning complex relationships between input parameters and resulting spray behavior. This allows fast and accurate predictions under different operation conditions in comparison to semi-empirical models, learning complex interactions without requiring extensive manual calibration. Nowruzi et al. [179] have investigated different architectures of ANNs to estimate the average spray penetration and cone angle of a single nozzle injector. The input parameters for training the supervised feed-forward network using the back-propagation method included nozzle diameter, injection pressure, injection profile, back pressure, and ambient temperature.

Hwang et al. [101] employed a regression model to predict the liquid penetration length, liquid width, and three-dimensional distribution of spray liquid fraction of a multi-hole gasoline injector. Their model included nine input features (fuel properties such as density and viscosity, along with ambient variables), showing a good agreement with experimental data. Lie et al. [141] derived a mathematical equation for spray penetration via a back-propagation neural network for Biodiesel and Diesel mixtures. They modeled a single-hole injector, where the input parameters were the fuel characteristics and injection pressure. This model was subsequently enhanced by Richards and Emekwuru [212] due to the limited experimental training data. They mitigated overfitting problems from the prior model with a systematic approach to uncertainty.

Khan et al. [116] evaluated the efficiency of four machine learning methods (random forest, extreme gradient boosting, multilayer perceptron, and elastic net) in predicting spray penetration and angle. Although their study focused on single and dual hole injectors, they utilized only two geometric characteristics as inputs: normalized nozzle outlet diameter and conicity, hence simplifying those injectors to single hole configurations in their models. Zhang et al. [301] examined the sensitivity of parameters in a generic algorithm backpropagation neural network for predicting spray penetration, comparing its performance with semi-empirical methods. Their model utilized experimental data from a single hole injector, with the ANN model incorporating operational variables and fuel properties as input parameters.

In general, ML offers superior accuracy and flexibility for spray macroscopic prediction compared to empirical models, especially via neural networks, which are able to handle highly nonlinear relationships and complex interactions. However, an elevated number of input parameters increases the data needed for effective generalization, and potentially leading to overfitting, especially with limited data. Also constraints and cost requirement for data acquisition may restrict the inclusion of numerous input parameters [103, 116]. If data is scarce for certain classes, their inclusion could introduce noise and reduce accuracy. Besides, the additional parameters can demand more computational resources, and collinearity among geometric parameters can destabilize models, hindering interpretability and accuracy [301].

1.3 Problem context and gap from previous research

CFD simulations can provide a comprehensive picture of the flow field inside the injector and spray development. Capturing these dynamics with high-fidelity models often requires advanced modeling techniques and in consequence significant computational resources and time. Furthermore, experimental testing may still be necessary as CFD simulations often require empirical data for model validation. Those high demands increase the gap between state-of-the-art scientific solutions and standard capabilities of commercial software, which is mostly applied in industrial workflows. Narrowing this difference with an affordable computational cost means that industrial applications can benefit from more precise simulations, leading to better decision-making and bringing innovations faster to the market.

A further step can be taken via fast numerical methods. Semi-empirical models can predict spray behavior with certain limitations. These models often simplify the underlying physics to make those equations more tractable, compromising their accuracy and generalization outside the range of the original experiments. Those simplifications restrict their use during the pre-development phase of injector design. Besides, Semi-empirical spray models are more commonly developed for light-duty applications due to their dominance in the market. Heavy-duty marine injectors often operate over a much wider range of conditions than light-duty injectors, making the extrapolation or tuning of those models a time-consuming process without guaranteeing accurate results.

Moreover, numerous studies have investigated the influence of nozzle geometries such as diameter, spray hole shape and grinding radius on the internal flow of Diesel injectors. Those studies underscore the importance of geometrical parameters in shaping the internal flow patterns and influence on cavitation. However, some points still require further investigation when applied to an optimization problem. Some of those finds can be case dependent and the interconnected behavior of geometrical parameters can sometimes be contradictory. Overall, the optimization of the injector design needs to ensure a precise fuel delivery and good atomization, while issues such as in-nozzle cavitation or uneven distribution should be minimized. However, the interplay between injector design, operation conditions and performance is a complex and non-linear topic and the existing methods to predict or detect the inflow characteristics require elevated time and resources.

1.4 Thesis objectives and outline

The aim of this thesis is to develop an integrated numerical framework that supports the design and optimization of marine Diesel injectors capable of operating efficient under both dual-fuel and Diesel-only conditions. The proposed framework combines CFD simulations, experimental data and ML surrogate modeling to predict relationships between injector geometry, in-nozzle flow behavior, cavitation development and spray characteristics. The surrogate models derived enable rapid design space exploration during the early stages of injector development. The injector type explored in this study is typically used for small to medium sized four-stroke marine engines, with an average displacement volume of 5L per cylinder. The main objectives of this thesis can be summarized as follows:

- To propose a CFD methodology that properly capture compressible effects while maintaining a reduced computational cost.

- To apply the proposed methodology to investigate the influence of needle-tip geometry on nozzle hydraulic performance optimization for fuel-flexibility operation.

- To generate a physics-based CFD database describing the interaction between key injector design parameters and cavitation behavior.

- To develop a workflow and investigate the feasibility of CFD-assisted ML surrogate models for predicting cavitation characteristics while mitigating issues due to CFD data limitation and dimensionality discrepancy.

- To develop and validate a data-driven ML model for predicting spray macroscopic characteristics using operational and geometrical parameters as input features.

- To develop and present a set of numerical tools for design optimization that enables rapid design-space exploration during early-stage injector development for fuel-flexibility operation.

The main body of the thesis has been divided into five chapters:

Chapter 2 introduces the computational methodology. The governing equations along with the employed assumptions are described for the CFD model, where the tabulated thermodynamic closure is coupled to the flow solver. The ML approaches are also discussed, focusing on the data preparation requirements and neural networks architecture strategies.

Chapter 3 validates and applies the CFD model to investigates the influence of needle-tip geometry on the internal flow characteristics of marine Diesel injectors. The physics-based understanding of how the geometrical modification affects in-nozzle flow is addressed in order to use a single and non-complex Diesel injector.

Building upon these findings, **Chapter 4** develops a ML surrogate models trained on CFD-generated data. The presented data pre-processing strategies mitigates models issues due to data limitation and dimensionality discrepancy. Therefore, this chapter translates the physics capture by the CFD into efficient predictive models subtile for rapid design exploration of in-nozzle flow.

Chapter 5 extends the models from the internal nozzle to the external spray. In this case, experimental measurements provide a suitable data source for training the surrogate model for spray macroscopic characteristics. This chapter represents the final step of the proposed framework, linking injector geometrical parameters and operation conditions to spray performance.

Collectively, these contributions establish a unified numerical framework to enable efficient design-space exploration during early design phase of marine Diesel injectors operating under fuel-flexibility conditions. Finally, **Chapter 6** outlines the conclusions of the current work and future perspectives.

Chapter 2

Computational methodology

In this chapter the physical, mathematical and numeric modeling of the current work is presented. First, the set of governing equations and models of the CFD methodology are introduced, followed by the ML method.

2.1 Computational Fluid Dynamics

The CFD simulations are performed using the commercial software ANSYS Fluent©. The theoretical background and numerical implementation are described in detail in the ANSYS Fluent Theory Guide [9] and in standard fluid dynamics textbook [198]. In this work, a homogeneous mixture multiphase formulation is employed to represent the three components existing in Diesel injection: liquid fuel, fuel vapor and ambient gas (nitrogen). The phases are assumed to be in a local mechanical and thermal equilibrium, sharing common velocity, pressure and temperature fields in each computational cell. Under these assumptions, the flow field is described by the mixture continuity, momentum and energy equations, together with volume fraction for the secondary phases. The liquid-vapor interface is represented through a diffuse-interface approach, while phase change between liquid and vapor fuels is modeled using a cavitation model. The governing equations are closed using thermodynamic and transport properties supplement to the solver, where the properties of the liquid fuel are implemented through external User-Defined Functions (UDFs) to incorporate the PC-SAFT EoS tabulated calculations. The resulting system of equations are solved iteratively via a pressure-based solver using the Pressure-Velocity Coupled algorithm. All numerical simulations are performed in a three-dimensional configuration.

2.1.1 Mass Conservation

The differential formulation for the mass conservation is shown in Equation 2.1.

$$\frac{\partial \rho}{\partial t} + \nabla \cdot (\rho \vec{v}) = 0 \tag{2.1}$$

where ρ is the mixture density, $\vec{v}$ is the mass averaged velocity as given in Equations 2.2 and 2.3,and the ∇ represents the Del operator. The mixture properties are calculated as volume fraction weighted average of the individual phases.

$$\vec{v} = \frac{\sum_{k=1}^{N} \alpha_k \rho_k \vec{v_k}}{\rho} \tag{2.2}$$

$$\rho = \sum_{k=1}^{N} \alpha_k \rho_k \tag{2.3}$$

where N is the number of phases. α_k and ρ_k are the volume fraction and density of phase k respectively. In the present formulation, three phases are interpenetrating and a control volume constraint in each cell must be taken into consideration as $\alpha_l + \alpha_v + \alpha_{air} = 1$, where $\alpha_l, \alpha_v, \alpha_{air}$ are respectively the volume fraction of liquid fuel, air and vapor fuel in a cell.

Cavitation

A liquid at constant temperature can be exposed to a decreasing pressure, which may fall below the saturated vapor pressure. The process of rupturing the liquid by a decrease of pressure at constant temperature is called cavitation. The liquid also contains the micro-bubbles of non condensable (dissolved or ingested) gases, or nuclei, which under decreasing pressure may grow and form cavities. In such processes, very large and steep density variations happen in the low-pressure/cavitating regions. In this work, the effect of dissolved non-condensable gas in the liquid phase is not taken into consideration, excluding the gaseous cavitation due to the expansion of non-condensable gas bubbles. The air is treated as a non-condensable gas phase and does not participate in the liquid-vapor phase change source terms. Consequently, cavitation mass transfer is modeled only between the fuel liquid and vapor phases as shown in Equation 2.4.

$$\frac{\partial \alpha_v \rho_v}{\partial t} + \nabla \cdot (\alpha_v \rho_v \vec{v}) = R_e - R_c \tag{2.4}$$

where R_e and R_c are source terms relative to the mass transfer between liquid and vapor phase. Zwart-Gerber-Belamri [307] approach was selected to model this process. This model is based on Rayleigh-Plesset equation [28] to compute the source terms (R_e and R_c) due to cavitation bubble expansion and collapse as shown in Equation 2.5 and Equation 2.6.

$$R_e = F_{vap} \frac{3\alpha_{nuc}(1-\alpha_v)\rho_v}{R_b} \sqrt{\frac{2}{3} \frac{p_v - p}{\rho_l}} \quad \text{if} \quad p < p_v \tag{2.5}$$

$$R_c = F_{cond} \frac{3\alpha_v \rho_v}{R_b} \sqrt{\frac{2}{3} \frac{p_v - p}{\rho_l}} \quad \text{if} \quad p > p_v \tag{2.6}$$

where F_{vap} is the evaporation coefficient and F_{cond} is the condensation coefficient. Both coefficients are empirical calibrated, where in this work the values 50 and 0.01 are used respectively. α_{nuc} is the volume fraction associated with the nuclei contained in the liquid that is $5.0e^{-4}$ and R_b is the bubble radius $1.0e^{-6}m$.

2.1.2 Momentum conservation

Momentum

The momentum conservation in an inertial (non-accelerating) reference frame can be described as shown in Equation 2.7.

$$\frac{\partial(\rho\vec{v})}{\partial t} + \nabla \cdot (\rho\vec{v}\vec{v}) = -\nabla p + \nabla \cdot (\bar{\bar{\tau}}) \tag{2.7}$$

where p is the static pressure and $\bar{\bar{\tau}}$ is the stress tensor, which represents the moment transfer due to all the turbulent fluctuations for RANS equations. $\bar{\bar{\tau}}$ is calculated as shown in Equation 2.8.

$$\bar{\bar{\tau}} = \mu[(\nabla\vec{v}) + \nabla\vec{v}^T] \tag{2.8}$$

where μ is the molecular viscosity.

Turbulence closure

Large Eddy Simulation (LES) is a widely employed approach to capture turbulence across scales in injector flows [292]. However, due to the associated high computational cost [188], LES is still impractical for industrial research and development time scales. On the other hand, over the last years, RANS and URANS models have become more sophisticated, thus presenting a satisfactory time compromise and acceptable agreement with experimental results such as mass flow rate, velocity profiles, and vapor distribution [92, 252, 201, 82]. Their accuracy to predict cavitation in high-pressure operating conditions has been improved due to the integration of enhanced turbulence and cavitation models, as well as advancements focusing on more realistic representations such as density-correct models, multi-phase models and mesh refinement to capture the small-scale cavitation structures near the nozzle exit [58, 123].

Hence, the turbulence closure is carried out using the Shear-Stress Transport (SST) $k-\omega$ model, where the turbulent kinetic energy and specific dissipation rate can be defined as described in Equation 2.9 and Equation 2.10.

$$\frac{\partial \rho k}{\partial t} = \frac{\partial}{\partial x_j}[(\mu + \sigma_k \mu_t)\frac{\partial k}{\partial x_j}] + P_k - \rho\beta * k\omega \tag{2.9}$$

$$\frac{\partial \rho \omega}{\partial t} = \frac{\partial}{\partial x_j}[(\mu + \sigma_\omega \mu_t)\frac{\partial \omega}{\partial x_j}] - \rho\beta * k\omega^2 + P_\omega + 2(1-F_1)\rho\sigma_{\omega 2}\frac{}{\omega}\frac{\partial k}{x_i}\frac{\partial \omega}{x_i} \tag{2.10}$$

where P_k represents the rate of production of k, ω is specific turbulent dissipation rate, P_ω is rate of production of ω , σ_ω is the turbulent Prandtl number for the rate of dissipation ω and F_1 is a model blending function.

In addition, a correction is applied to turbulent viscosity to account for the two-phase mixture compressibility effects [205], as follows in Equation 2.11

$$\mu_t = f(\rho)\frac{a_1 k}{max(a_1\omega, SF_2)} \tag{2.11}$$

where a_1 is a constant assumed as 5/9, the density ρ is replaced with a function $f(\rho)$ as described in Equation 2.12, S represent the strain tensor magnitude ($S \doteq \sqrt{2S_{ij}S_{ij}}$) with the components S_{ij} and the additional functions calculated as shown in Equation 2.12-2.14

$$f(\rho) = \rho_v + (\frac{\rho_v - \rho_m}{\rho_v - \rho_l})^n(\rho_l - \rho_v) \tag{2.12}$$

$$F_2 = tanh(arg_2^2) \tag{2.13}$$

$$arg_2 = max(\frac{2\sqrt{k}}{0.09\omega y}, \frac{500v}{y^2\omega}) \tag{2.14}$$

2.1.3 Energy conservation

In compressible flows or flows that involve heat transfer, an additional equation for energy conservation needs to be solved. The conservation of energy within the mixture can be formulated as the following form as shown in Equation 2.15.

$$\frac{\partial \rho E}{\partial t} + \nabla \cdot [v(\rho E + p)] = \nabla \cdot ((k_{eff}\nabla T) + (h\vec{J}) + (\bar{\bar{\tau}} \cdot \vec{v})) \tag{2.15}$$

where ρ is the mixture density, $\vec{v}$ is the velocity vector field, p is the pressure, y_{fuel} is the fuel mass fraction, T is the temperature and h is the enthalpy as a function of pressure and temperature. The total energy, E, is the sum of internal energy and the kinetic energy and can be described as shown in Equation 2.16.

$$E = h - \frac{p}{\rho} + \frac{1}{2}\vec{v} \tag{2.16}$$

Also, the total effective thermal conductivity, k_{eff}, is calculated as a function of pressure and temperature, as formulated in Equation 2.17.

$$k_{eff} = k + \frac{c_p \mu_t}{Pr_t} \tag{2.17}$$

where c_p is the heat capacity of the mixture and Pr_t is the turbulent Prandtl number.

2.1.4 Thermodynamic closure

The thermodynamic properties of the liquid fuel are calculated using the PC-SAFT EoS. The PC-SAFT EoS is based on perturbation theory, in which a reference fluid is defined to calculate the repulsive contribution. The reference fluid is composed of spherical segments comprising a hard-sphere fluid that then forms molecular chains to create the hard-chain fluid. The attractive interactions, which are perturbations to the reference system, are accounted for with the dispersion term [80]. Hence, the liquid phase thermodynamic properties can be defined as functions of the residual Helmholtz energy and its derivatives. The transport properties were estimated using the residual entropy scaling method for dynamic viscosity [146] and for thermal conductivity [98].

In order to reduce the computational cost associated with property calculations using the PC-SAFT EoS, the thermodynamic and transport properties of the fuel were calculated prior to the CFD simulations and stored in structured tables, decoupling the evaluation during flow calculation and, thus, speeding-up the simulation [216]. The thermodynamic table is generated using in-house code and implemented into the commercial software ANSYS Fluent© via the UDFs: User-Defined-Real-Gas-Model (UDRGM). Besides, the compressible effects of the vapor phases (fuel vapor and inert ambient as nitrogen) were derived using National Institute of Standards and Technology (NIST) Reference Fluid Thermodynamic and Transport Properties Database (REFPROP) for their thermodynamic properties [133]. The tabulated approach with all modifications described in this chapter increased the computational time by approximately 8-10% relative to the constant properties formulation. However, this increase is negligible relative to the order of magnitude cost increase in computational cost associated with direct EoS evaluations.

2.1.5 Numerical solution

The ANSYS Fluent© is a control-volume-based technique, which consists of dividing the domain into discrete control volumes using a computational grid. Ansys Fluent© will solve the governing integral equations for the conservation of mass, momentum, energy and other scalars such as turbulence and chemical species in a control-volume-based technique. The discretization of the governing equations is done with a second order upwind scheme, except for the transport equation and mass diffusion flux of the fuel. Besides, the gradients are computed via Least Squared Cell Based method and the pressure interpolation via Body Force Weighted scheme.

In transient simulations, the governing equations are also discretized in time by an implicit manner. For complex flow configurations, the implicit schemes are recommended since they increase robustness and numerical stability [285]. As previously mentioned, the solution is obtained via Pressure-Velocity Coupling solver. The momentum equations and the pressure-based continuity equation are solved in a closely coupled manner, in which the convergence rate significantly improves compared to the segregated algorithms. Additionally, this requires the usage of more memory as a result of storing all momentum and pressure-based continuity equations when solving the velocity and pressure fields. The iterative Pressure-Velocity

Coupling can be outlined in six steps:

- Update fluid properties based on the current solution.
- Solve simultaneously a system of momentum and pressure-based continuity equations using the recently updated values of pressure, velocity field and the mass-flux.
- Correct face mass fluxes, pressure, and the velocity field.
- Solve the equations for additional scalars.
- Update the source terms arising from the interactions among different phases.
- Check for the convergence of the equations.

These steps are continued until the convergence criteria for the absolute values of the normalized residuals are achieved (10^{-4}) .

2.2 Machine Learning

The ML workflow is a structured process for generating predictive models from data by comprising several phases as depicted in Figure 2.1. The first stage involves outlining the problem by addressing the scope and feasibility of machine-based problem-solving, as well as identifying the constraints in properly representing real-world or linguistic complexities. Then, the data is collected or generated, cleaned, and pre-processed. This involves handling missing values, transforming data types and feature engineering when necessary. The data is normally scaled to ensure quality and suitability for the chosen machine learning algorithm. The processed data is subsequently divided into training and testing sets to facilitate model training and performance evaluation on unseen data, respectively.

The machine learning algorithm must be selected based on the problem type (e.g., regression, classification) and the characteristics of the data. The selected method is trained on the training dataset to learn the underlying patterns and correlations, with hyperparameters adjusted accordingly. Thereafter, the trained model undergoes evaluation on the testing dataset to determine its accuracy and generalizability and to identify any issues such as overfitting or underfitting. Finally, the model is deployed for real-world use, incorporated into an application or used

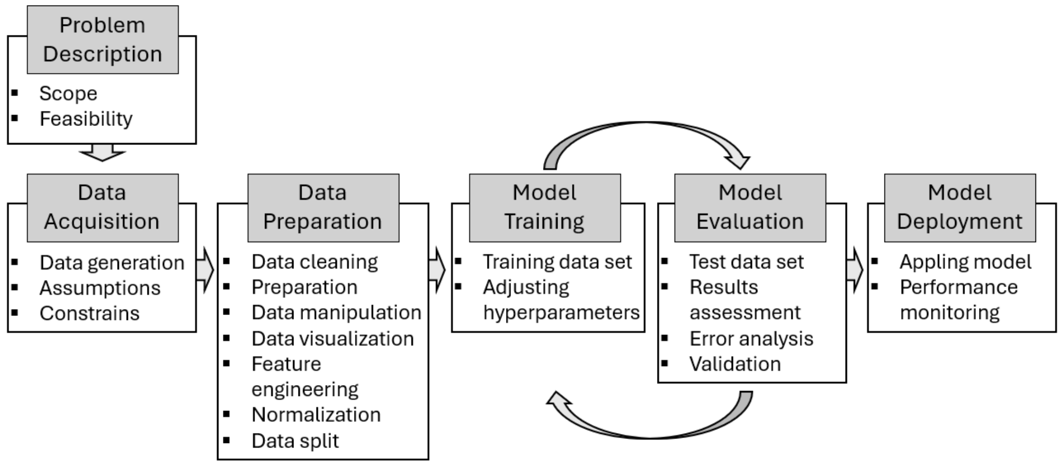

Figure 2.1: General ML workflow illustrating the systematic process of problem definition, data preparation, training, evaluation, and model deployment.

to provide predictions on novel data. Continuous monitoring and maintenance are essential to ensure the model's precision and dependability throughout time.

2.2.1 Data preparation requirements

The collection and preparation of data is a vital step in ML, as it directly impacts the model performance. These steps represent around 45% to 80-90% of the overall effort of the entire workflow [277]. Particularly when data originates from diverse sources, the preparation phase can be quite demanding to ensure the quality and success of the entire workflow. In recent years, the emphasis on data quality and management prioritization, rather than exclusively on model refinement, has gained momentum, also known as Data-centric Artificial Intelligence [295, 241].

Raw data is frequently incomplete, inconsistent, and may originate from several sources. The quality and quantity substantially affect the stages of preparation strategy. Therefore, comprehending the data's attributes and the problem area is essential at this point. Data visualization assists in feature selection and exposing potential biases at all stages of the ML workflow, not just prior to model training [219]. Exploratory Data Analysis (EDA) involves the examination of data through visual methods and summary statistics, revealing trends, uncovering patterns, and identifying anomalies, which are essential for building accurate and reliable models [163].

Besides, during data standardization, the main issues typically include insufficient data descriptions, improper formatting, duplicate entries, missing values, and outliers. Following the inconsistencies correction and the unification of the dataset, transformation techniques, including feature scaling and categorical variable encoding, ensure that the data is formatted appropriately for the selected ML algorithm. The feature scaling is the standardization of values to a range, normally 0 to 1 and can be done for example by min-max normalization as shown in Equation 2.18.

$$x' = \frac{x - min(x)}{max(x) - min(x)} \tag{2.18}$$

where x is the original value, x' is the normalized value, $max(x)$ is the maximal value in the range and $min(x)$ is the minimum one. This is especially significant in training deep learning models, because steady gradient computations are essential for effective learning, mitigating problems such as vanishing and exploding gradients [281].

Finally, feature engineering can be performed to transform raw data into significant features. Feature engineering encompasses not only the modification of current features or the extraction of new ones but also the integration of domain knowledge into the ML workflow during the creation, transformation or selection of input variables (features). Well-designed features may considerably enhance model performance by identifying heterogeneity or outliers in the addressed problem, minimizing computational costs and training duration by concentrating on the most relevant information, while also enhancing model interpretability [173, 265].

2.2.2 Deep Neural Networks

Inspired by brain synapses, ANNs and DNNs are subareas of ML that comprise numerous layers of interconnected nodes, known as neurons, which process and transmit information. Every connection between neurons has an associated weight, which is adjusted throughout the training process to learn the underlying patterns within the data [102]. The DNN is distinct from the ANN because of its deep architecture, featuring numerous hidden layers situated between the input and output layers, as depicted in Figure 2.2a, enabling it to handle more complex data and tasks [231].

The artificial neuron, or Perceptron, is a singular threshold logic unit within an ANN or DNN [74], as shown in Figure 2.2b. Each neuron receives inputs, processes them, and produces a single output. The inputs typically consist of the outputs from neurons in the previous layer, or the raw data in the case of the input layer, represented as $x = \{x_1, x_2, ..., x_n\} \in R^n$. Each input is associated with weight denoted as $w = \{w_1, w_2, ..., w_n\} \in \mathbb{R}^n$, which represents the strength of the connection. Furthermore, neurons often include a bias w_0, which is incorporated into the weighted sum of the inputs, enabling the neuron to fire even when all inputs are zero.

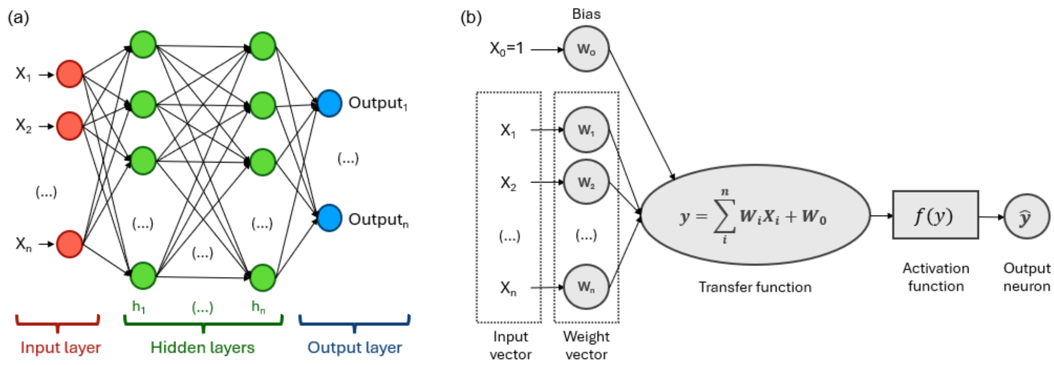

Figure 2.2: (a) Schematic topology of a Deep Neural Network, (b) threshold logic unit of an artificial neuron that computes weights or Perceptron.

The weighted sum of the inputs and the bias is then processed through an activation function as defined in Equation 2.19. The activation function introduces non-linearity into the network, enabling it to learn complex patterns [51]. The activation function sets a neural network apart from a linear regression model, giving it the capacity to model complex data. The output of the activation function becomes the output of the neuron and is thereafter assigned as input to neurons in the next layer.

$$y = \sum_{x=i}^{n} w_i x_i + w_0 \tag{2.19}$$

The most common activation functions are Sigmoid, Rectified Linear Unit (ReLU), and hyperbolic tangent (tanh). This study employed a variant of the ReLU, referred to as the LeakyReLU activation function. This function is available in the Keras library and assists in mitigating issues related to inactive neurons. Neurons may intermittently become inactive during training and allowing a minimal non-zero gradient for negative inputs mitigates the problem of "dying ReLUs" [149]. The LeakyReLU activation function is represented in Equation 2.20, where a is a learnable parameter.

$$LRelu(x) = max(0, x) = \begin{cases} x, & \text{if } x >= 0 \\ ax, & \text{if } x < 0 \end{cases} \tag{2.20}$$

An important parameter in the selection of the DNN is the number of hidden layers and neurons. A small number of layers may result in underfitting, as the network fails to sufficiently identify the inherent patterns in the data [4]. Increasing the number of hidden layers can improve the network's ability to model complex functions, however only to a certain degree. An excessive number of layers may result in overfitting, causing the network to assimilate the noise in the training data rather than the true signal. Therefore, the computational cost increases excessively without substantial improvement in accuracy [271].

The number of layers as well as the number of neurons inside each layer determine the architecture of the network. They are hyperparameters that regulate the learning process and facilitate efficient convergence. Therefore, choosing the appropriate values is essential for attaining optimal model performance. Moreover, the choice of activation function can also be classified as a hyperparameter, along with the learning rate, which regulates the step size during training; the batch size, which specifies the number of samples used in each iteration; the weight initialization method; the number of epochs; and the regularization parameters. Adjusting hyperparameters often focuses on accuracy and model loss. It is performed manually by experimentation, relying on experience, and/or through automated methods when several trials were required due to model complexity [23].

2.2.3 Generative Model

Generative model (GM) is a category of ML models capable to learning dense representations. Unlike discriminative models, which focus on distinguishing between classes, GMs aim to approximate high-dimensional data distributions and generate new similar data samples for uses like data augmentation, image synthesis, anomaly detection and creative tasks such as music generation [75, 294, 26]. Generative models, such as Variational Autoencoders (VAEs), Generative Adversarial Networks (GANs) and Normalizing Flows, are all implemented using neural networks with multiple hidden layers [26].

The base architecture of VAEs consists of an encoder, a probabilistic latent space, and a decoder as illustrated in Figure 2.3a. On the other hand, the GANs, as shown in Figure 2.3b, consist of two main components: a generator and a discriminator, which are trained simultaneously in an adversarial process. Both VAEs and GANs use a generator network, which in the case of VAEs is normally called a decoder.

The generator/decoder is a neural network that transforms lower-dimensional distribution into complex data space, enabling the creation of new and realistic samples [172].

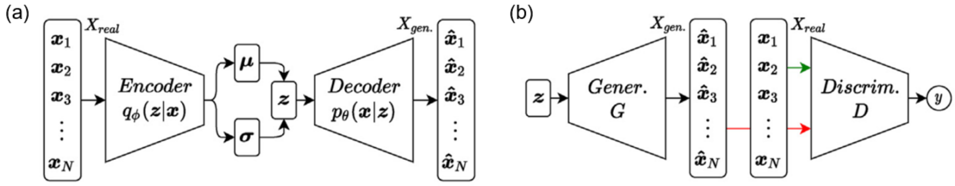

Figure 2.3: Basic architecture of some Generative Models: (a) Variational Autoencoder, where the encoder inputs and decoder output present the same distribution, (b) Generative Adversarial Networks, where generator-discriminator progressively refine image quality [249]

The generator/decoder architecture is the second ML model used in this work. The reason for choosing this model is the possibility to directly map low-dimensional (scalar or vector) inputs to complex, high-dimensional images, enabling fast and flexible image synthesis without the need for a full encoder-decoder or adversarial training setup. The general generator/decoder architecture is illustrated in Figure 2.4. The architecture typically starts with a low-dimensional vector (1D tensor of scalar values) that is passed through one or more fully connected layers to expand its dimensionality. Then, the dense layer is reshaped into a 2D or 3D tensor. This step is crucial for transforming the compact input into a format suitable for subsequent convolutional transposed layers.

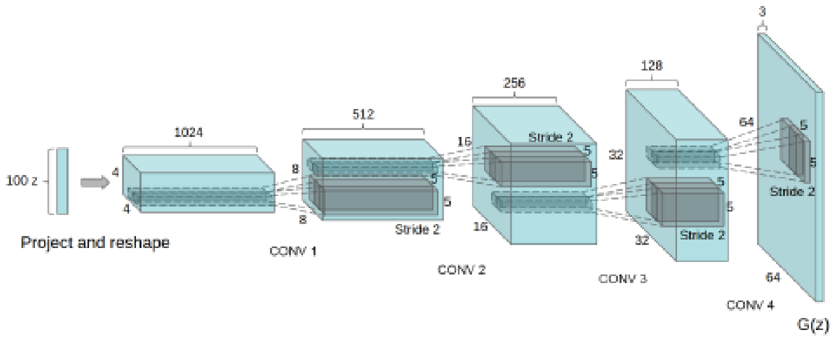

Figure 2.4: Architecture of generator/decoder with transposed convolutional layer [202].

A convolutional neural network is composed of multiple hidden layers. These layers are organized in terms of depth, width, and height [136]. Depth refers to the number of feature maps (or channels) in a layer, representing different learned features. Width and height correspond to the spatial dimensions of the feature maps. As data flows through the network, the width and height typically increase due to strided convolutions. The depth (number of feature maps) increases and decreases, allowing the network to capture a richer set of features.

The transposed convolutional layer is the core of the architecture. The layer increases the spatial dimensions of the feature maps, gradually constructing the image from coarse to fine details. Batch normalization and activation functions are commonly used after each convolutional layer to introduce non-linearity. The Batch normalization adjusts and scales the activations, normalizing the output of a layer. This process helps reduce the internal change in the distribution of network activations due to parameter updates during training [43].

The upsampling in the transposed convolutional layer is controlled via stride and padding. Stride sets the step size for moving the kernel during upsampling as shown in Figure 2.5. The dimension of a kernel, also known as filter, determines the receptive field for the transposed convolution operation [55]. Meanwhile, padding involves adding pixels around the input borders feature map before applying the transposed convolution operation, managing the spatial alignment and output size. A "valid" padding adds no extra pixels, whereas "same" padding adds pixels to ensure the output size is maintained or extended.

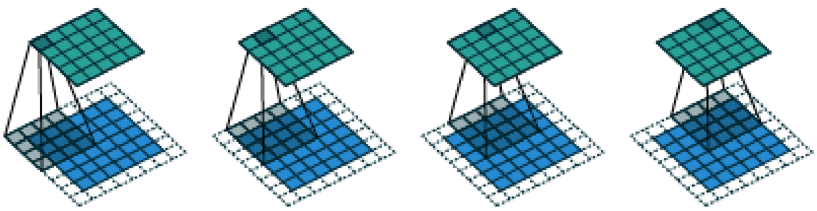

Figure 2.5: Representation of upsampling in transposed convolutional layer for a 4x4 kernel over a 5x5 input padded with 2x2 border using 1x1 strides [55].

The final layer typically uses a transposed convolutional layer to map the feature maps to the desired image size and number of channels, for example 3 channels for RGB images. Moreover, activation function and regularization techniques can be applied in a convolutional neural network to introduce non-linearity and improve generalization. This study implemented the Sigmoid and LeakyReLU activation function. The Sigmoid is commonly used in output layers for binary classification since it squashes outputs between 0 and 1, as represented in Equation 2.21.

$$\sigma(x) = \frac{1}{1 + e^{-x}} \tag{2.21}$$

Finally, the generator/decoder architecture used in this work will be described as Generative Model (GM). The reason for this is to simplify since the model is an adaptation or extracted part of the complete architecture of VAEs or GANs and still belongs to the same ML classification.

2.2.4 Regularization and Error estimation

A neural network can be mathematically interpreted as a group of functions $f_w : x \rightarrow y$ with trainable weights $w \in W$ where the main goal is to minimize the loss function. The loss function typically combines the expected risk ($\mathbb{E}_{(x,t)\sim p_{\text{data}}(x)}$) of error ($E(f_w(x), t)$) with a regularization term ($R(...)$) that balances accuracy and generalization [127] as shown in Equation 2.22 and Equation 2.23.

$$w = arg \min_{W} Loss \tag{2.22}$$

$$Loss = \mathbb{E}_{(x,t)\sim p_{\text{data}}(x)}[E(f_w(x), t) + R(...)] \tag{2.23}$$

Regularization in a neural network refers to a set of strategies that add constraints or penalties to the learning process, preventing the model from memorizing the training data [229]. They help control the model complexity, preventing it from overfitting and improving its ability to generalize unseen data. They can be categorized based on how they influence the data, model architecture, loss function, or optimization process, where the choice and strength often depend on the specific dataset and network architecture [85].

Therefore, in complement of subchapter 2.2.2, two additional regularization techniques were employed to mitigate overfitting issues arising from the limited data available. Dropout was the first regularization technique employed acting on the model architecture, wherein nodes randomly cease to transmit their forward signal during training with a probability rate. Consequently, following each update during training, the layers are arranged in a marginally altered configuration, allowing network layers to co-adapt in order to rectify errors from the preceding layer [246, 306].

The second regularization technique employed was early stopping, influencing the optimization process. This cross-validation strategy terminates training when the model's performance no longer enhances over multiple consecutive epochs. Traditionally, this involves using a validation set to monitor performance. Nonetheless, the exclusion of a validation set, as implemented in this study, decreases computing time, which is beneficial in scenarios with limited data or noisy labels [263].

Moreover, the error $(E(f_w(x), t))$ quantifies the difference between predicted outputs and true values, guiding the learning process. Two loss functions were used in this work, the Mean Absolute Percentage Error (MAPE) and the Mean Squared Error (MSE). The MAPE measures the average magnitude of errors between predicted and actual values, expressed as a percentage. The MAPE can be defined as shown in Equation 2.24:

$$MAPE = \frac{1}{n}\sum_{i=1}^{n}\frac{|y_i - Y_i|}{|y_i|}.100\% \tag{2.24}$$

where n denotes the number of data points in the training dataset, y_i represents the predicted output value of the DNN model, and Y_i the target value. A value near 0 denotes negligible error. The percentage error will significantly increase in the presence of outliers, as it is particularly sensitive to anomalous results.

The MSE penalizes larger errors more heavily due to squaring, making it sensitive to outliers. MSE is always positive and the smaller the loss value is, the better manages the model to fit the data. It quantifies the average squared difference between the predicted and actual values as defined in Equation 2.25.

$$MSE = \sum_{i=1}^{n}(y_i - Y_i)^2 \tag{2.25}$$

Chapter 3

Influence of Needle-Geometry Design on In-Nozzle Flow Characteristics for Fuel Flexibility in Marine Engines

This chapter is based on the author's second publication, published in the Journal of International Engine Research, doi: 10.1177/14680874251398815.

3.1 Introduction

The single Diesel injector architecture presents technical challenges due to the significant differences in injection and flow characteristics between the two operation modes [40]. The geometrical parameters impose changes in the inflow, which may lead to geometric-induced cavitation [83]. In fuel injectors this can have negative or positive effects on their performance. It can contribute to cycle-to-cycle variations in fuel delivery [156] and enhance the spray cone angle, velocity coefficient and atomization [184, 185]. Nonetheless, its collapse near solid surfaces can inflict damage on the injector walls, lead to erosion, and in severe situations, cause deterioration of injector performance and eventual injector failure [123].

Previous investigations in the literature underscore the importance of geometrical parameters in the design of Diesel injector performance. However, nearly all investigations focused on the nozzle geometry [90, 245, 37, 225], with only a reduced number concentrating specifically on the needle-tip geometry. Even less focused on their influence in marine applications. Due to the market dominance, most of the research topics have historically focused on light-duty applications over marine injectors [298]. Besides, the needle-tip redesign is often simpler to implement, requiring less extensive re-tooling or manufacturing changes and is cost-effective compared to the injector modifications.

In particular, the needle-tip directly influences the flow structure in the sac hole, especially for low needle lifts. It also contributes to the effective volume of the sac hole, which plays a role in vortex formation, cavitation and unsteady flow [7, 38]. Watanabe et al. [273] compared the recirculation zones of three needle-tip designs with different seat angles and imposing different sac volumes in a mini-sac nozzle. They observed that the geometry of the needle-tip affects the vortex flow in the sac hole. The needle with a larger angle increased vortical cavitation. A reduced needle-tip angle results in increased spray penetration and a constant injection rate, accompanied by a smaller spray cone angle. Markov et al. [151] examined the influence of grooves on the needle-tip, which imposed localized hydraulic resistance in a VCO nozzle. This resistance amplified flow turbulence, increased the turbulent kinetic energy at the orifice outlet and induced cavitation within the nozzle. As a result, the fuel atomization was improved. However, it adversely affects the mass flow rate and flow velocity.

Hence, the aim of the current chapter is to investigate and understand the influence of needle-tip design on the in-nozzle flow and cavitation for marine injectors. Furthermore, this study proposes an improved design suitable for fuel flexibility throughout the entire engine operation range. For that, the potential of needle-tip geometrical modifications is investigated through CFD simulations, where three needle-tip designs were proposed and compared to a base design. Moreover, dual-fuel and Diesel-only operation mode were emulated using a fixed set of needle lifts (54 μm and 480 μm) to isolate the geometrical influence on the in-flow conditions. However, it needs to be considered that this does not capture the full range of dynamic behavior during real engine operation.

3.2 Needle-tip geometries

The present work focuses on the impact of the geometry of the needle-tip in marine Diesel injector design provided by Woodward L'Orange (WLO). The base design is a Diesel injector with 7 straight holes (K- factor equal to 0) and a spray hole diameter above 300 μm. The proposed needle-tip geometries were select based on prior WLO design studies. Due to confidentiality restrictions associated with the industrial collaboration, the specific geometric values and rationale process of these geometries cannot be fully disclosed. Nevertheless, the selected configurations were chosen to systematic investigate the hydraulic influence of three principal geometric modifications: introduction of a deflection angle, elongation and smoothing of the needle-tip profile. As consequence, all proposed modification impact on the reduction of the sac volume. Figure 3.1 shows the base design as well as the three proposed modifications, where the geometry of the nozzle and needle seat remains identical in all variations.

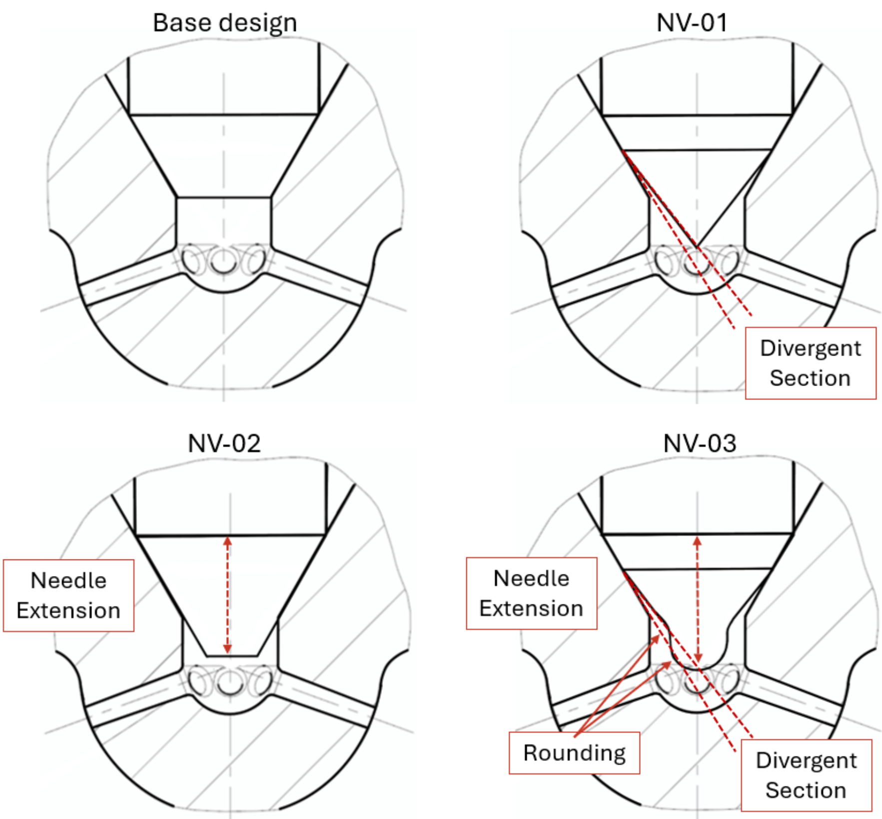

Figure 3.1: Comparative view of the base Design and the three proposed needle-tip modifications.

In the first proposed needle-tip variation, NV-01, a deflection angle was incorporated on the first third of the needle-tip through a minor elevation. This angle creates a diverging section between the needle-tip and needle seat, increasing the cross-section downstream of the throat. In addition, the needle-tip was extended into a conical form, hence reducing the variation of sac volume. After these alterations, the sac volume is reduced by 7.5% compared to the base design.

The second variation, NV-02, focuses on the impact of a reduced sac volume. Therefore, the shape and angles of the base design were kept constant. To achieve a volume decrease, the needle form was elongated along the vertical axis until a total reduction of 21.5% was reached. Finally, the third variation, NV-03, integrates the primary features of the two previously described designs: divergent section, volume reduction, and needle-tip elongation. The deflection angle remained constant in the initial third of the needle-tip, resulting in a significant volume reduction of 27.5% due to the needle's elongation into a spherical form. In addition, some roundness was included in the transition areas to avoid sharp corners.

Although sac volume influences combustion-related phenomena, such as fuel dribble and unburned hydrocarbons emissions [155][155], the present study focuses specifically on internal nozzle flow characteristics and cavitation risk associated with reduced sac volume. During the pre-development design phase, injector hydraulic performance is prioritized over emissions optimization. Combustion and emissions are strongly depend on coupled effects of injector behavior, combustion chamber geometry, injection strategy and transient spray-combustion interactions [50]. Consequently, emissions optimization becomes relevant only when the nozzle hydraulics are matched to piston bowl geometry, targeting and injection strategy. Therefore, this work should be interpreted as a preliminary hydraulic performance investigation aimed at identifying promising needle-tip characteristics for subsequent engine-coupled optimization studies.

3.3 Numerical simulation framework

3.3.1 Simulation setup

Taking advantage of the existing symmetry in the injector design and in order to reduce the computational overhead, only one injector hole is included in the computational domain (1/7 sector of the injector). The computational domain consisted of the inlet, housing wall, needle wall, side surfaces and discharge volume as shown in

Figure 3.2. The outlet domain or discharge volume is a 1.5 mm long conical volume to reduce the influence of the outlet boundary condition on spray propagation.

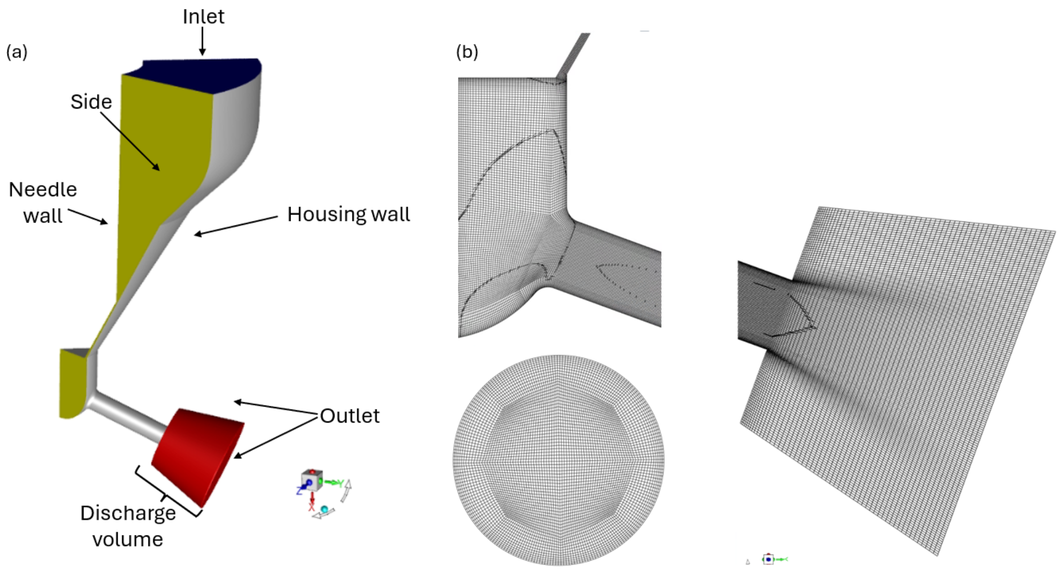

Figure 3.2: (a) Schematic of the computational domain. (b) Section view of the grid topology in the injector hole and downstream-chamber regions. The final grid corresponds to the base design at low lift position.

The computational domain was discretized using a fully hexahedral mesh to control the number of elements and accelerate the convergence. Besides, in order to capture better small-scale cavitation structures, some strict quality criteria were defined to ensure the cell quality and minimize the discretization and model errors [166]. The volume-change ratio between neighbouring cells was kept below 5, with a minimum cell angle of 22,5° and a 3D determinant (normalized triple product of the vectors starting from each cell node) above 0.5 for both key-grids.

The Taylor micro-scales were considered for the cell size definition in the bulk flow region. In this study, the impact of the needle position and shape led to different in-flow velocities. Hence, the Reynolds number based on the spray hole diameter can be estimated to between 61,000 and 92,000 for the four geometries at the two lift positions, where the mathematical description can be found in Appendix A. The Taylor micro-scales can be estimated between 4.1 μm and 3.3 μm. The maximum mesh resolution was defined based on those criteria and the grid independence study. The effect of the mesh resolution and the impact on the velocity at the spray hole exit are presented in Table 3.1. A slight variation can be observed between Grid 3 and Grid 4, demonstrating a reasonable achievement of grid convergence. Based on these results, the Grid 3 with a maximum mesh resolution of 4.2 μm inside the injector spray hole was selected in this study to avoid an excessive cell count. The other geometries presented an equivalent mesh resolution and quality.

Grid	Lift [μm]	Cell Count	Min. Orth. Quality	Velocity [m/s]
1	480	1.42M	0.366	551.59
2	480	2.98M	0.256	554.25
3	480	4.16M	0.251	556.51
4	480	5.76M	0.248	557.38

Table 3.1: Velocity sensitivity at the exit of the spray hole for the different grid resolutions.

Further away from the nozzle exit, the mesh becomes coarse with a maximum resolution of 46.3 μm at the outlet region. Under these constraints, the mesh comprises around 4M elements at 480 μm needle lift and 3M at 54 μm. This mesh strategy and final resolution has been verified at full lift for a different injector from WLO and is able to predict the mass flow rate with a difference below 3% in comparison to the experimental measurements.

In addition, for each geometry, the needle was placed in two positions: high lift at 480μm and pilot lift at 54μm. In total 8 geometries were generated and Table 3.2 summarizes the nomenclature used as well as the numerical grid metrics for each one of them.

Case	**Needle**	**Lift**	**Cell Count**	**Min. Orth. Quality**
1	Base Design	54μm	3.29M	0.325
2	NV-01	54μm	3.41M	0.381
3	NV-02	54μm	3.28M	0.291
4	NV-03	54μm	3.15M	0.291
5	Base Design	480μm	4.16M	0.251
6	NV-01	480μm	4.15M	0.250
7	NV-02	480μm	4.18M	0.285
8	NV-03	480μm	4.02M	0.248

Table 3.2: Geometry annotation and mesh metric for the examined designs.

The modeling approach has been described in Chapter 2 and the boundary conditions were kept constant in all simulations. The in-nozzle region was initialized to contain pure n-dodecane, and the chamber downstream of the injector nozzle to contain nitrogen. Fixed pressure and temperature values of 1600 bar and 343 K were imposed at the inlet, while the respective conditions at the domain outlet were 50 bar and 780 K. A symmetry boundary condition has been applied to the side surfaces. Additionally, the nozzle walls are considered adiabatic. Figure 3.2 depicts the computational domain, boundary conditions and grid topology.

3.3.2 Validation

The implemented numerical methodology was validated via mass flow rate measurements and X-ray phase contrast radiographies, which were highlighting the extent of cavitation in the single-hole Spray C (serial 210037) injector reported in the ECN (Engine Combustion Network) database [57]. The Spray C nozzle has nominal inlet and outlet diameters of 185μm and 208μm, respectively. The orifice length is 1.0 mm and the injector K-factor is -2.5. The orifice was drilled off-center with a sharp inlet corner to disturb the flow, as shown in Figure 3.3, inducing cavitation up to the flow separation.

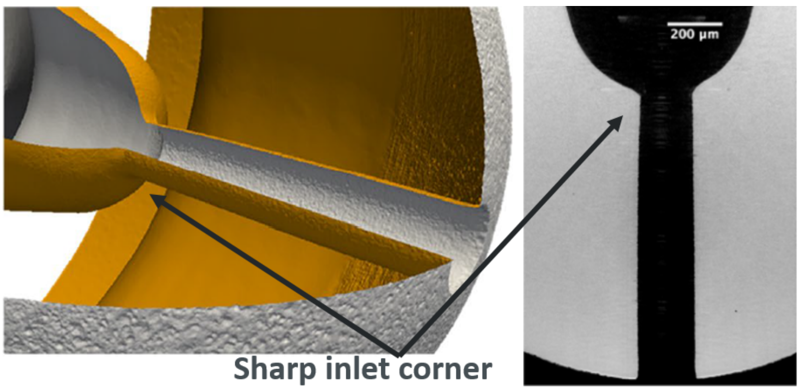

Figure 3.3: ECN Spray C surface representation derived from high-resolution X-ray computed tomography [152]

The injector flow was simulated at a fix needle lift of 271 μm to match the experimental conditions. The injection pressure was kept constant at 1500 bar as inlet boundary condition and the ambient pressure was 20 bar, once again, in consistency with the X-ray experiments. The working medium, dodecane, was modeled at 343 K, while the ambient temperature was set to 303 K. The presence of non-condensable gas was not included in the model. The computational mesh corresponded to a three-dimensional domain with a hexahedral structured topology.

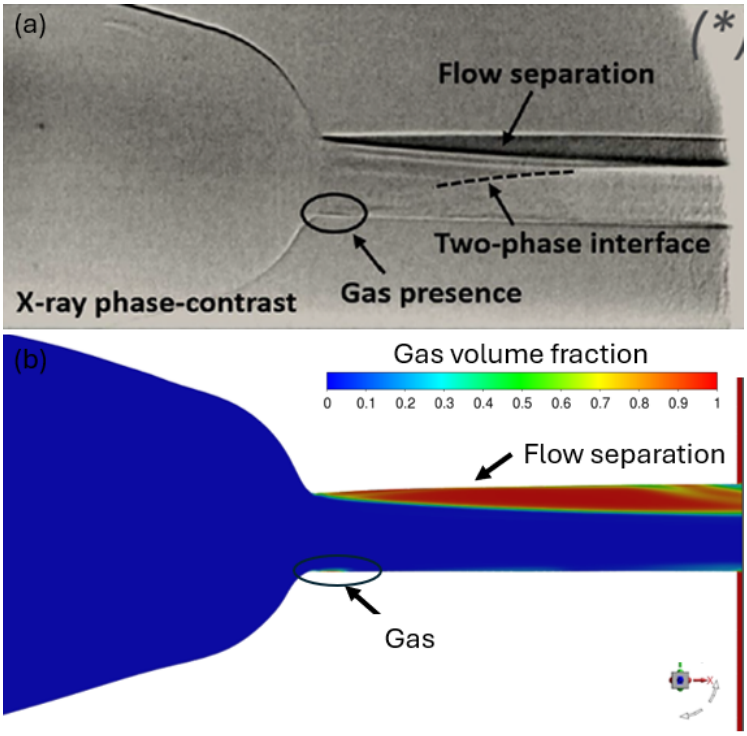

Figure 3.4: Validation of the numerical methodology against X-ray data for the axial development of the two-phase flow field in the Spray C benchmark injector: (a) X-ray phase contrast radiography (used with permission of SAE International, license no: 1683328-1, from Guo et al.[84], permission conveyed through Copyright Clearance Center, Inc.), (b) contour plot of gas fraction at the orifice mid-plane.

Figure 3.4 shows a comparison of the line-of-sight radiography (Figure 3.4a) against a contour plot of the gas volume fraction at a plane passing through the orifice axis of symmetry (Figure 3.4b). The X-ray image illustrates a strong flow separation at the upper region of the injector hole, accompanied by the formation of a cavitation sheet attached to the wall. Vapor starts forming at the sharp hole entrance and is convected downstream all the way to the orifice outlet. In addition, a minor gas pocket can be seen at the lower part of the hole entrance. The numerical results are able to reproduce the two-phase flow topology arising in the injector hole.

Furthermore, numerical data has been compared against X-ray images at six cross-flow planes along the orifice length, as shown in Figure 3.5. Overall, the numerical simulation is able to accurately predict the shape of the vapor region along the injector-hole periphery, even the small liquid film in the upper part of the plane corresponding to -134 μm. Some of the observed differences could be related to shot-to-shot variability and temporal fluctuations during the experimental measurement. The X-ray phase contrast image is a time-averaged measurement.

Finally, to complement this qualitative validation, Payri et al. [187] measured

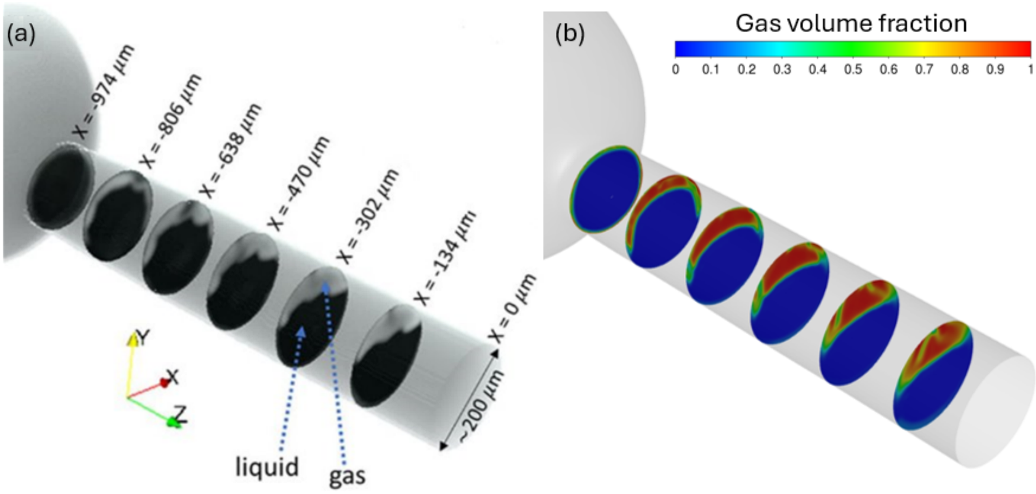

Figure 3.5: Validation of the numerical methodology against X-ray data for the radial development of the two-phase flow field in the Spray C: (a) X-ray radiographies at different cross-flow planes (reprinted from Tekawade et al.[254]); (b) Cross-flow contour plots of the vapor field.

the mass flow rate for the Spray C injector for the operating conditions examined here and found it equal to (10.07 ± 0.11) g/s. The respective value predicted by the numerical simulation is 10.47 g/s. The discrepancy can be attributed to surface roughness and manufacturing tolerances, which are neglected in the numerical model. In summary, the CFD simulation results show good consistency with the experimental data, reproducing the main flow characteristics as well as the in-nozzle gas distribution.

3.4 Results and discussion

In order to facilitate the interpretation of designs, the comparison of the four needle-tip designs were divided into two sections, focusing on the dual-fuel (low-needle position or pilot injection) and Diesel-only operation (high-needle position). The Reynolds number between 61,000 and 92,000 across all configurations indicates a fully turbulent regime. Consequently, small geometric variations in the needle-tip region can substantially alter local flow acceleration, pressure distribution, and cavitation inception. The parameters analysed in this work were mass flow, cavitation morphology, velocity, pressure, and three flow coefficients. The mass flow and flow coefficients were determined at the injector hole exit.

3.4.1 Internal flow characteristics during pilot injection (dual-fuel mode)

The influence of the needle-tip on the internal flow field during pilot injection can be assessed at low needle lift of 54 μm, which is representative of dual-fuel operation. Figure 3.6 shows the influence of the needle-tip design on the velocity field placed at the spray hole mid-plane. The low needle position generates a constricting zone between the needle and the injector seat, which accelerates the flow in this region, allowing it to enter the orifice at high velocities at the bottom half of the spray hole. This restricted passage has an impact on fluid redirection and varies significantly based on the needle-tip design.

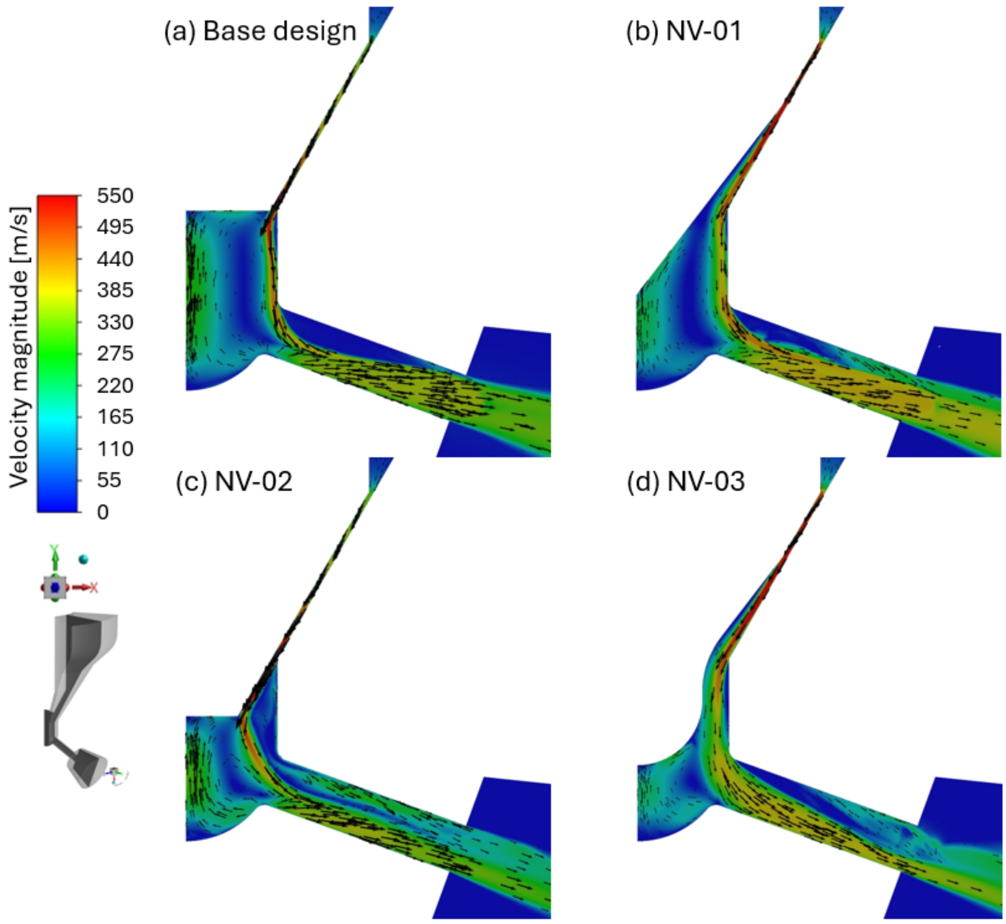

Figure 3.6: Vector-over-contour plots showcasing the velocity field in the nozzle spray hole mid-plane for the four needle-tip designs examined at pilot injection condition.

In the base design and NV-02, the fluid flows closer to the needle and seat wall. The flow remains attached to the sac wall in the base design until a boundary layer separation from the wall occurs due to the redirection of the high-velocity flow at the spray hole inlet. This separation causes a flow contraction that results in a pressure drop within the spray hole, as depicted in Figure 3.7. The pressure threshold plotted in the contours is limited to 5 bar in order to emphasize the reduced static pressure regions. Conversely, the needle elongation on NV-02 results in flow separation from the sac's side wall, as the flow tends to remain attached to the needle wall. The reduced static pressure zone is repositioned within the sac, resulting in a more uniform velocity distribution within the spray hole exit.

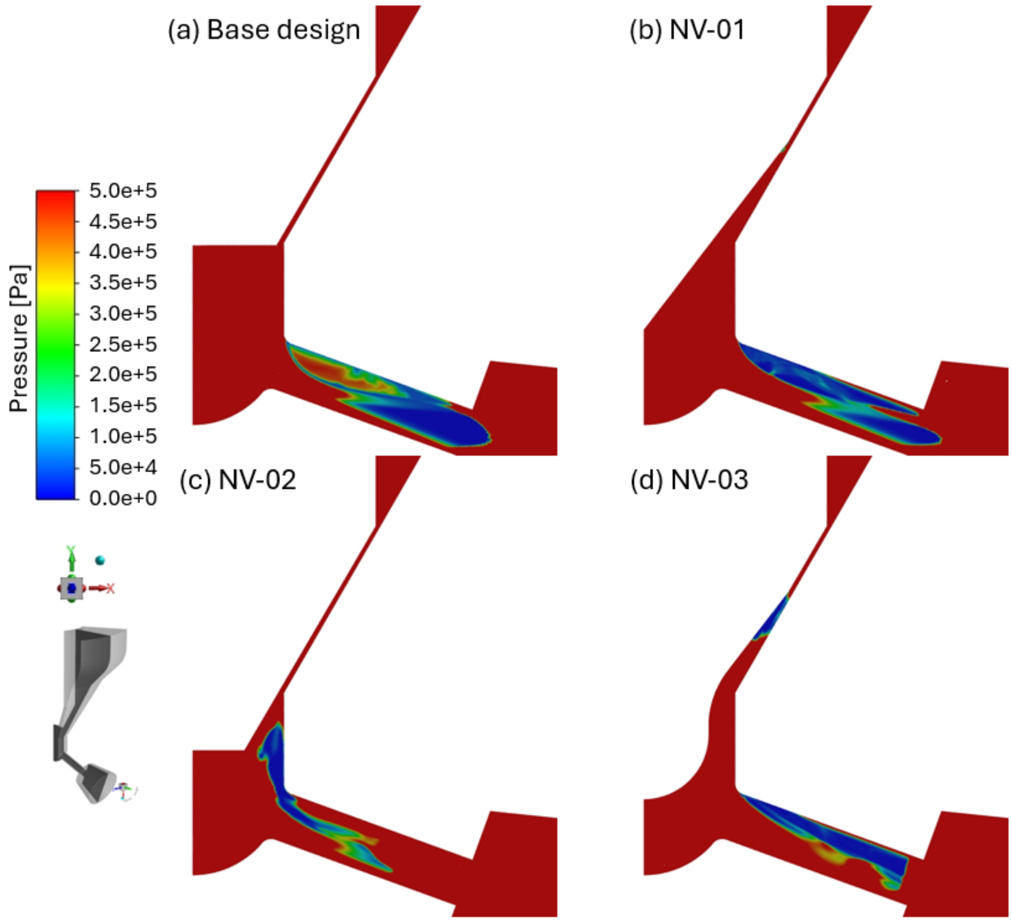

Figure 3.7: Pressure distribution in the nozzle spray hole mid-plane for the four needle-tip designs examined at pilot injection condition.

In the NV-01 and NV-03, the fluid flows closer to the injector seat wall and is detached from the needle wall due to the deflection angle incorporated in those designs. Despite the deflection angle being minor (below 10 degrees), boundary layer separation can be observed due to the low-pressure zone created at both valve seats in Figure 3.7. In both systems, the high-velocity flow remains adjacent to the wall in the sac. Nonetheless, the elongation and roundness transitions of the needle in the NV-03 lead to a flow deceleration as depicted in Figure 3.6, reaching the spray hole with smaller velocity than NV-01. Additionally, a vena contracta is generated in the spray hole, which further enhances the flow acceleration and reduces the pressure in the upper part of the spray hole.

These low-pressure zones are critical for the onset of cavitation when the static pressure drops below the vapor pressure of the continuous fluid [244]. They increase the hydraulic resistance and could lead to violent collapse events of cavitation structures, generating high-pressure peaks that can cause erosion [123]. At the same time, the cavitation structures can enhance fuel atomization and spray formation [14, 7]. Therefore, a balanced approach is essential to harness the benefits of cavitation while mitigating its adverse effects.

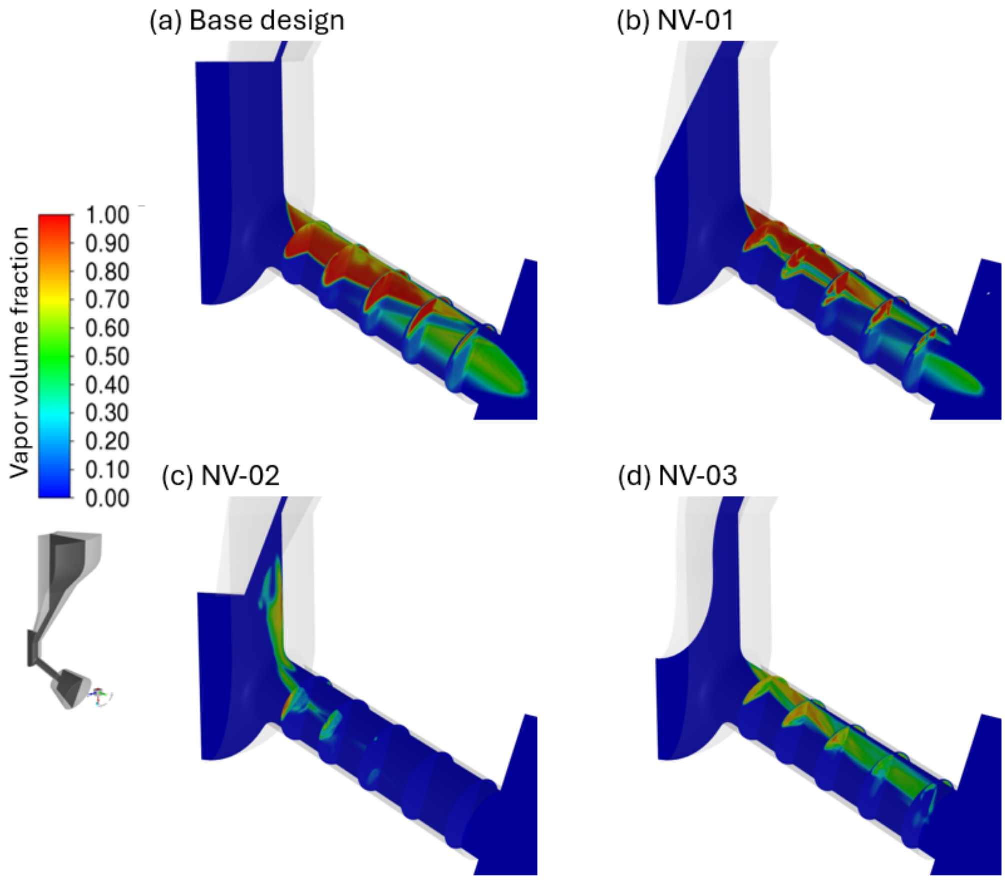

Figure 3.8: Contour plots of the vapor volume fraction at different axial and cross-flow planes in the injector hole for the four needle tip designs examined at pilot injection condition.

The phase transition from the liquid to vapor is illustrated in Figure 3.8. The contour plots of the vapor volume fraction are presented at the orifice plane of symmetry and five equidistant cross-flow planes. The cavitation can be closely associated with the low-pressure zones depicted in Figure 3.7. Furthermore, no significant quantity of vapor was seen in the lower pressure zone of the valve seat for NV-01 and NV-03. Consequently, the contour plots concentrated exclusively on the sac and spray orifices.

As expected, the base design, NV-01 and NV-03 exhibit cavitation at the spray hole inlet, with vapor formation along the upper surface of the spray hole. NV-02 is the only design in which cavitation is mitigated within the spray hole by relocating it to the sac. The cavitation in the sac hole can disrupt the internal flow, resulting in irregular fuel delivery and reduced mass flow rates [150, 93]. This location presents considerable risks in comparison to cavitation occurring in the spray hole. In contrast, regulated cavitation in the spray hole can enhance atomization and improve combustion efficiency [90].

A relevant parameter for cavitation is the cavitation number, where the mathematical description can be found in Appendix A. The four geometries present a cavitation number bellow 0.22. This very low value indicates that the injector operates in a cavitating regime. However, the similar range in global cavitation number cannot explain the differences between the base design and modified ones. Therefore the local effects, controlled by geometry-induced local velocity and pressure minima are more relevant in this study.

A quantitative comparison of the four geometry revels that the proposed designs reduced the cavitation intensity and the vapor quantity within the nozzle as detailed in Table 3.3. To facilitate the comparison of the designs, the vapor volumes were standardized by the total of the sac and spray hole volumes.

Design	**Normalized vapor volume [%]**	$\dot{m}_f$ **[g/s]**
Base	13.58	14.30
NV-01	9.60	15.96
NV-02	5.77	13.03
NV-03	5.98	14.03

Table 3.3: Normalized vapor volume and mass flow rate for different needle-tip designs at pilot injection condition.

The base design produces the highest normalized vapor volume (13.58%), whereas all modified geometries reduce cavitation intensity. Specifically, NV-01 reduces the vapor volume by approximately 29%, while NV-02 and NV-03 achieve reductions of about 57% and 56% respectively relative to the base design. Nonetheless, cavitation intensity and mass flow rate is not a simple linear relationship. The magnitude and location of cavitation are crucial, as seen in Table 3.3. The vapor bubbles reduces the flow area and can increase the flow resistances, typically resulting in a reduction of the mass flow rate [187]. In some cases, properly controlled cavitation can increase the mass flow and consequently the discharge coefficient of the injector, hence enhancing the fuel flow rate and improving the overall efficiency of the injection process [87]. The onset of cavitation and its impact on mass flow rate are also affected by the fuel saturation pressure and heating value [258].

In complement, Table 3.4 shows the relationship between cavitation and injector performance via flow coefficients. The discharge coefficient C_d represents the ratio between the theoretical mass flow and the actual mass flow. It indicates the injector's capacity to deliver the desired amount of fuel. The velocity coefficient C_v represents the ratio of the actual flow velocity to the theoretical velocity. It express the kinetic energy of the fuel jet as it exits the nozzle. The third non-dimensional flow parameter is the area coefficient C_a, which correlates the effective flow area to the geometric orifice area and considers the contraction of the flow streamlines as the fuel passes through the orifice. The mathematical description of the flow coefficients can be found in Appendix A.

Design	C_d	C_v	C_a
Base	0.396	0.478	0.828
NV-01	0.443	0.520	0.853
NV-02	0.363	0.363	0.999
NV-03	0.387	0.391	0.989

Table 3.4: Dimensionless flow coefficients for different needle-tip designs at pilot injection condition.

Since the pressure difference (ΔP) between inlet and ambient pressure remains constant among all cases, the C_d is mainly a consequence of the mass flow rate ($\dot{m}_f$) and the liquid density (ρ_l). NV-01 exhibits the hightest C_d (0.443), corresponding to an increase of approximately 12% compared to the base design, while reducing the normalized volume vapor by 29%. This indicates that NV-01 does not only simple suppress cavitation, rather it modifies its location and intensity in a positive way. In contrast, NV-02 and NV-03 show a reduces C_d, despite their lower overall normalized vapor volume relative to the base design. This indicates that location and morphology of cavitation can be more critical than the volume vapor absolute magnitude. Specially in the case of NV-02, where the cavitation in the sac region can increase hydraulic losses even when the total vapor volume is reduced.

The C_v follows the same trend, with NV-01 achieving the highest value (0.520). NV-02 and NV-03 exhibit lower C_v, although their reduced cavitation intensity in comparison to the base design. This demonstrates that geometric features promoting smoother flow transitions can reduce local acceleration and, consequently, decrease the energy of the emerging jet. In terms of C_a, this metric also takes into account the flow separation areas. The base design, followed by NV-01, have the lowest effective area, which correlates with the normalized volume of vapor in the injector hole in those designs.

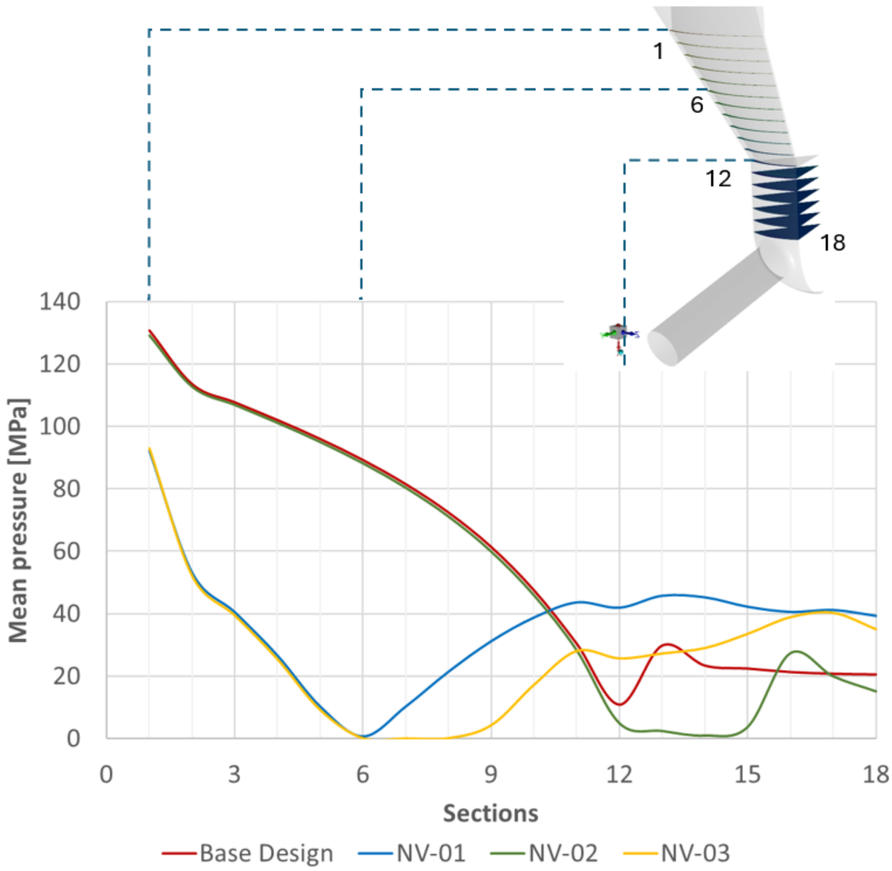

Figure 3.9: Average pressure distribution along the needle seat and sac hole for the four needle-tip designs at pilot injection condition.

Finally, a smooth and higher pressure build up inside the sac hole is a relevant characteristic that may contribute to a stable and consistent injection [150]. Elevated sac hole pressures create a better outward momentum that aids in preventing the ingress of external gases into the nozzle holes [76]. However, injector components may be susceptible to wear and tear as a consequence of excessive high pressure, thereby potentially reducing their lifespan and increasing maintenance costs[148].

The progression of the average pressure in the needle seat and sac hole is quantified in Figure 3.9, illustrating the pressure variation exerted on the fluid before reaching the spray hole. The planes 1-12 denote the average pressure in the seat region, where the deflection angle from NV-01 and NV-03 is located between planes 7 and 8. The sac hole region is covered from plane 12 to 18 and shortly before the spray hole inlet.

The base design and NV-02 exhibited the highest pressure up to the 10th probing plane with intensity progressively diminishing towards the needle-tip. After the 12th section, the base design facilitates pressure recovery within the sac hole. The pressure recovery in NV-02 happened only after the end of the needle-tip elongation and was further delayed due to flow separation and the low-pressure areas in the sac hole. Despite those impacts, the base design and NV-02 maintain the same pressure close to the spray hole inlet. The deflection angle on NV-01 and NV-03 results in a pressure drop along the needle seat compared to the previous designs. Subsequent to the 6th section, the pressure began to recover, resulting in an elevated pressure within the sac hole, which is nearly double that of the base design in the spray hole inlet area. Consequently, this pressure recovery can contribute to improved flow stability and its resistance to backflow or gas ingestion.

Overall, the results demonstrated that needle-tip geometry influences the injector performance at low needle lift position. The needle geometry has effects the on local acceleration and pressure gradients, which control the spatial distribution of vapor structures. Those cavitation clouds are consistent with previous studies. However, the present results show that their relocation and intensity lead to measurable differences in C_d (up to 12%), C_v (up to 24%) and C_a (up to 20%) relative to the base design. Therefore, an optimal injector performance depends on minimizing cavitation globally and also controlling its location and interaction with the main flow.

3.4.2 Internal flow characteristics during maximum needle lift injection (Diesel-only mode)

At high needle lift (480 μm), representative of Diesel-only operation, the flow dynamic differs fundamentally from the pilot injection regime due to the substantially increased effective flow area between the needle and seat. This reduces the severity of upstream throttling and shifts the dominant hydraulic restriction to the spray hole inlet. The impact of the needle tip design on the velocity field is shown in Figure 3.10 at the spray hole mid-plane. The seat region continues to accelerate the flow field, directing it towards the sac and then to the spray hole with elevated velocities compared to the low needle lift cases. However, the redirection of an accelerated flow is less abrupt and as a consequence a boundary layer separation is not created from the wall in the seat and sac hole.

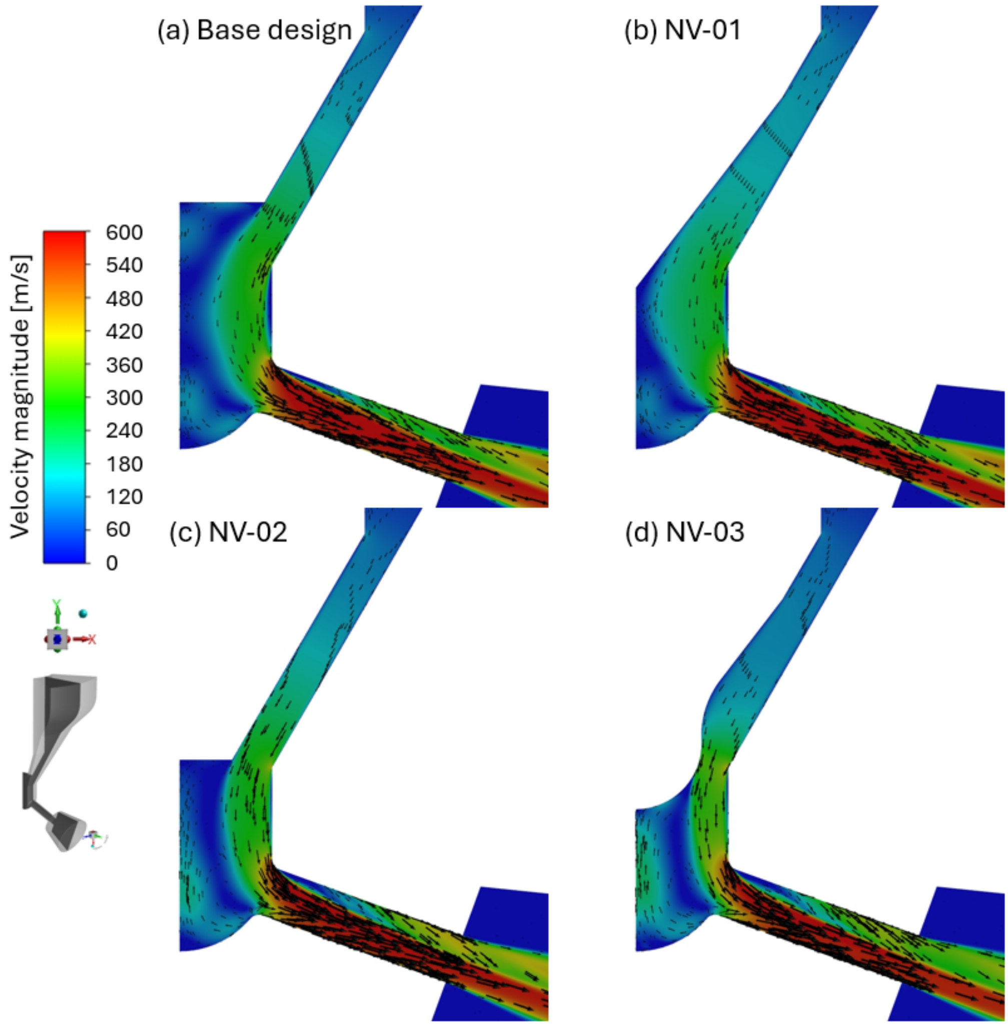

Figure 3.10: Vector-over-contour plots showcasing the velocity field in the nozzle spray hole mid-plane for the four needle-tip designs examined at Diesel-only injection condition.

The spray hole inlet serves as the primary flow constraint in all designs, imposing an abrupt deflection and resulting in flow detachment from the upper wall within the spray hole. The separated boundary layer forces the main flow to redirect, creating a turbulent, low-pressure region behind the separation point. These separation points can be verified via the adverse pressure gradients shown in Figure 3.11. Similar to the low lift investigation, the pressure distribution was also limited to 5 bar.

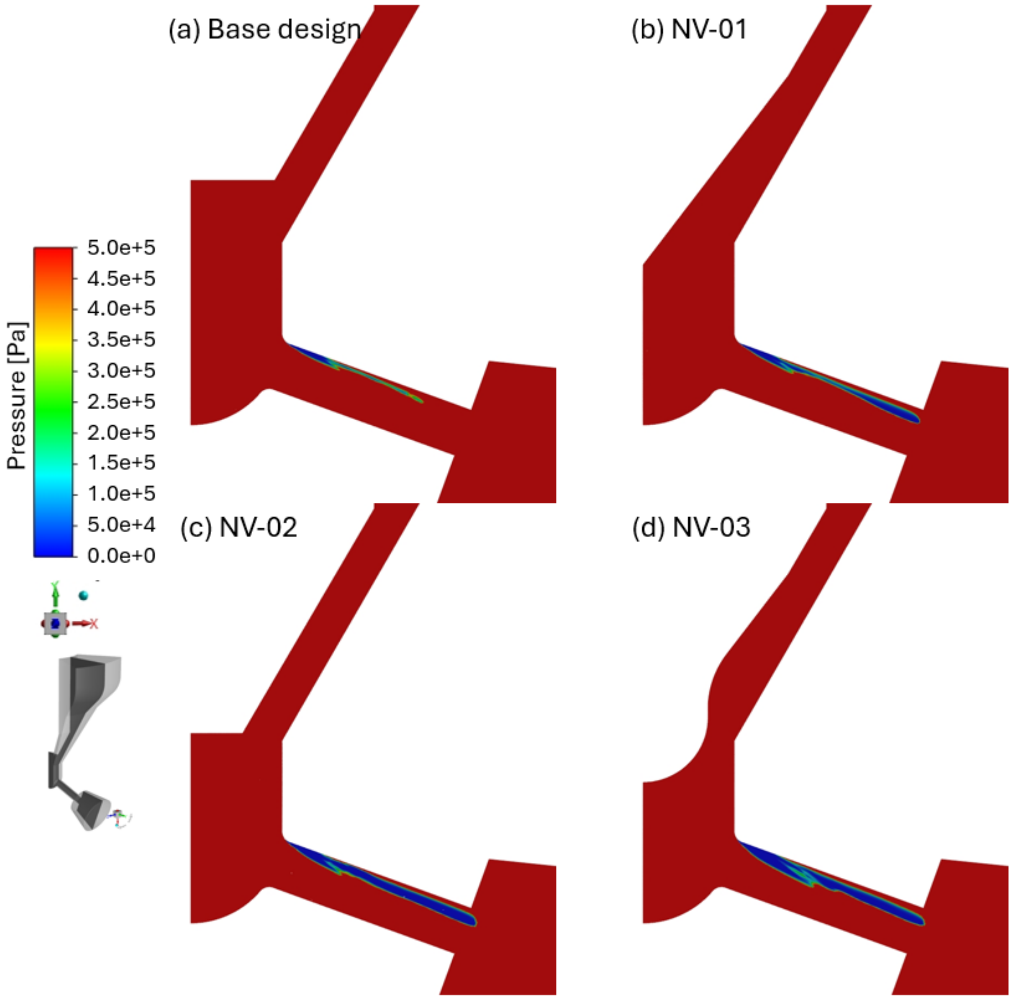

Figure 3.11: Pressure distribution in the nozzle spray hole mid-plane for the four needle-tip designs examined at Diesel-only injection condition.

This adverse pressure gradient further retards the already slow-moving boundary layer. The flow streamlines converge downstream of the separation point, creating a vena contracta in the four geometries. Nonetheless, the influence of additional flow acceleration and low pressure is manifesting with different intensities. The flow field across all configurations remains fully turbulent (Reynolds number above 61,000). Although the global cavitation number remains approximately constant due to fixed operation conditions, the geometric modifications alter the local velocity field and pressure minima. In all configurations, the on-set cavitation is located near the upper edge of the spray hole inlet as illustrated via the vapor volume fraction in Figure 3.12. The proposed designs qualitatively result in an expansion of the vena contracta relative to the base design, which expands towards to the spray hole exit. The larger vena contracta accelerates the flow in the lower part of the spray hole, intensifying the pressure decrease and enhancing the cavitation phenomena.

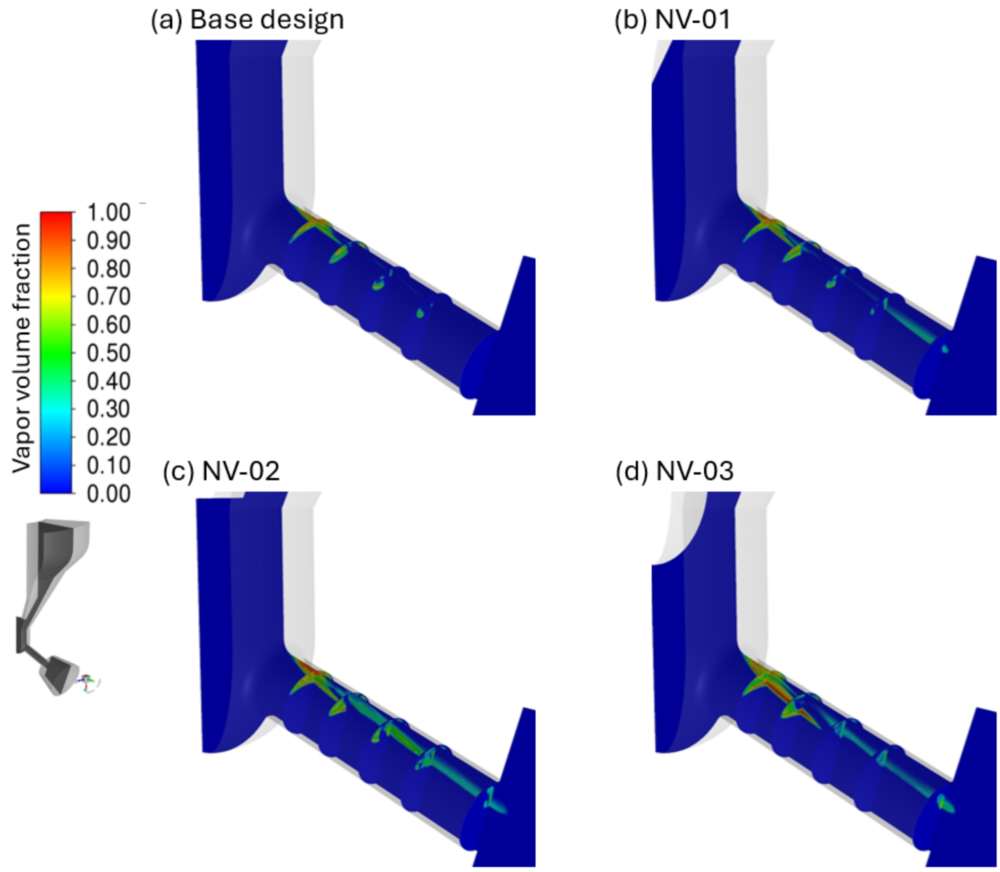

Figure 3.12: Contour plots of the vapor volume fraction at different axial and cross-flow planes in the injector hole for the four needle tip designs examined at Diesel-only injection condition.

A comparison of the normalized vapor volume reveals quantitatively that cavitation is significantly reduced relative to the low lift condition as shown in Table 3.5. As anticipated by the qualitative analyses of the images, the base design presents the lowest cavitation intensity (1.59%). NV-01 shows a nearly identical value (1.61%). This result suggest that the flow deflection introduced by NV-01 design has a negligible effect on cavitation behavior at high lift. In contrast, NV-02 and NV-03 show increased normalized vapor volumes (2.07% and 2.17% respectively). Those amounts correspond a increase of approximately 30-36% relative to the base design. Nevertheless, the absolute vapor volume remains low in both cases.

Similar to Table 3.3, Table 3.6 presents the flow behavior in terms of flow coefficients. Due to the needle being positioned at a high lift, its impact on the lowering of flow rate is less significant than that of the pilot injection discussed in Section 3.4.1.

The base design and NV-01 configuration exhibit nearly identical performance

Design	Normalized vapor volume [%]	$\dot{m}_f$ [g/s]
Base	1.59	31,08
NV-01	1.61	31,13
NV-02	2.07	28,82
NV-03	2.17	27,35

Table 3.5: Normalized vapor volume and mass flow rate for different needle-tip designs at Diesel-only injection condition.

Design	C_d	C_v	C_a
Base	0.832	0.835	0.996
NV-01	0.833	0.837	0.995
NV-02	0.739	0.741	0.997
NV-03	0.777	0.781	0.995

Table 3.6: Dimensionless flow coefficients for different needle-tip designs at Diesel-only injection condition.

in terms of C_d (0.832 and 0.833), confirming that the NV-01 modification does not introduce additional hydraulic losses at high lift. In contrast, NV-02 and NV-03 show reduced C_d (0.739 and 0.777), corresponding to decreases of approximately 11% and 7% relative to the base design. These reductions indicate increased flow resistance due to the higher sac volume reduction in those designs. As a consequence it leads to stronger contraction and less favorable local pressure recovery.

A similar trend is observed in C_v. The base design and NV-01 maintain high values (0.835 and 0.837), whereas NV-02 and NV-03 show reduced values (0.741 and 0.781). Furthermore, the reduction of the effective area of the liquid phase is indistinguishable among all designs as seen by the C_a, indicating that the effective liquid-phase area is only weakly affected by cavitation at high lift. The bubbles at the exit of the spray hole are minimal and neither flow separation nor hydraulic flip is observed at the spray hole exit in those designs. Consequently, the effective area of the liquid phase approaches values near 1.

Finally, the pressure in the needle seat and sac can be quantified prior to the fluid reaching the spray hole, as seen in Figure 3.13. Unlike the low lift regime, pressure variations are more gradual, reflecting the reduced influence of seat throttling. The NV-01 design enhances pressure maintenance in the needle seat and sac hole from

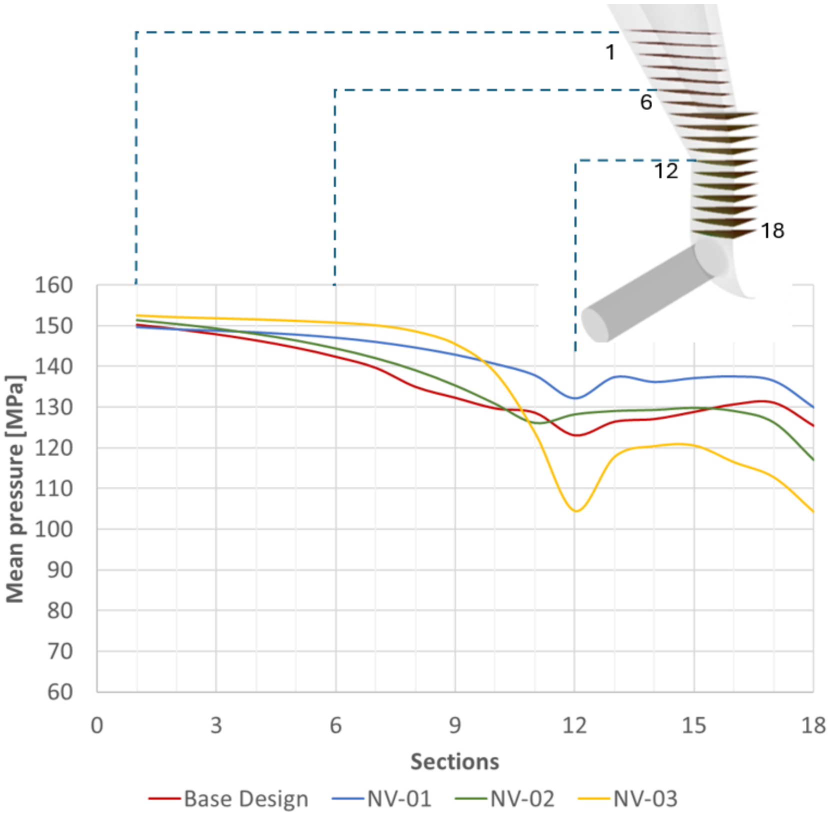

Figure 3.13: Average pressure distribution along the needle seat and sac hole for the four needle-tip designs at Diesel-only injection condition.

the first to the ninth segment, suggesting a improved pressure recovery without introducing significant losses. The NV-02 exhibits comparable performance to the base design for the average pressure. Both designs restrict the pressure drop in the sac to approximately 300 bar relative to the rail pressure. The NV-03 presents the highest pressure in the needle seat area, from the first to the ninth section. After the ninth section the pressure drops considerably, reaching its lowest pressure in the sac hole.

Overall, since the flow restriction at the needle seat is minimal, the spray hole inlet geometry controls the flow contraction and pressure drop. Consequently, modifications to the needle-tip have a limited influence on the hydraulic performance unless they significantly alter the flow approaching to the spray hole. This explains why NV-01 preserves the base line performance. Because its moderate flow deflection and sac volume reduction, NV-01 has only a minor impact on the flow field. In contrast, NV-02 and NV-03 significantly modify the sac geometry and volume, introducing additional hydraulic losses.

3.5 Conclusions from needle tip design modifications

This chapter presents a study on the impact of needle-tip design on internal flow and cavitation in marine Diesel injectors and supports the understanding of the in-flow characteristics of each operation mode. While experimental verification of the proposed geometries remains outside the scope of the present study, the observed trends provide guidance for future experimental campaigns and design optimization efforts with fuel-flexibility marine injectors. The numerical model has been enhanced by incorporating NIST and PC-SAFT EoS calculations through a tabulated thermodynamic method. The inclusion of NIST REFPROP and PC-SAFT EoS provides a good prediction as evaluated against experimental data regarding mass flow and cavitation regions under typical operating conditions of Diesel engines. The fluid properties variation, local depressurization, pressure gradients and phase changes were satisfactorily predicted. In order to enhance the base design that under-performs at dual-fuel conditions and to ensure fuel flexibility across the complete engine operation range, three needle-tip designs were proposed.

The redesign of the needle-tip was selected for its simplicity and cost-effectiveness compared to modifications in the nozzle design. The base design was evaluated against three proposed alternatives to assess performance in two operational modes: Diesel-only and dual-fuel. At low needle lifts (dual-fuel mode), the three proposed needle-tip designs reduce the vapor production within the injector. However, the results demonstrate that cavitation intensity alone is not a sufficient performance indicator. Instead the spatial distribution of cavitation plays a crucial role. NV-01 maintains cavitation condensed in the spray hole while enhancing pressure recovering the sac region. This combination resulted in a cavitation reduction of 29% and increased in C_d of 12% relative to the base design. In contrast, NV-02 shifted the cavitation into the sac volume, leading to increased hydraulic losses and reduction in performance (8% in C_d) despite the highest reduction on vapor volume (57%). Hence, the optimal performance is achieved through controlled cavitation, rather than its complete suppression.

In high needle lifts (Diesel-only mode), cavitation intensity is reduced across all configurations, with normalized vapor volumes below 2.2%. The base design and NV-01 exhibited comparable performance regarding cavitation location, fuel delivery and flow coefficients, indicating that moderated needle-tip modifications do not introduce additional hydraulic penalties in the orifice-controlled regime. NV-02 and NV-03 slightly increased the amount of vapor generated inside the spray hole, also reducing the performance as indicated by the flow coefficients. These results confirm that, under high lift conditions, performance is governed by orifice-induced flow separation and vena contraction formation. The needle-tip geometry plays a secondary role unless it significantly alters the upstream flow field.

Finally, among the tested configurations, NV-01 provides the most favorable trade-off between low and high lift performance for fuel-flexibility marine injectors. This design reduces cavitation intensity and enhances pressure recovery under pilot injection conditions. It also main the baseline hydraulic efficiency at high lift. As an subsequent step, a consistent performance across different operating conditions should be considered in validating the proposed design.

3.6 Critical review

This section critically examines the contributions of the present chapter in the context of research on in-nozzle flow and injector design. Following the submission of the manuscript reporting the present results, few studies have reinforced the importance of injector design as a key factor for more sustainable transportation technologies. For instance, Xie et al. [286] explored the influence of three needle types experimentally and numerically for hydrogen direct injection. They underscored the influence of the geometrical parameters on the spray characteristics and combustion stability. The recent work by Yang et al. [288] analyzed the influence of the grinding radius of methanol injectors to mitigate cavitation, which helps marine applications for fuel flexibility. Furthermore, Tang et al. [253] highlighted in their review paper the advancements and challenges of Natural Gas-Diesel dual-fuel engines for marine applications. The complexity of the fuel injection system is still a main drawback, whereas a single-needle and nozzle Diesel injector for both operation modes provides a more universal solution for all engine sizes and alternative fuel types. Therefore, the fundamental understanding of injector design and its influence on internal flow process remains essential for the advancement of economical and sustainable injection systems.

In this context, this study makes a contribution by demonstrating how relatively small geometric modifications can alter flow structure, cavitation intensity, and injector hydraulic performance. In particular, the NV-01 is identified as providing the most favorable compromise. This needle-tip geometry improves cavitation characteristics and pressure recovery at low needle lift without substantially degrading the performance at high lift. This finding is of practical relevance and demonstrates the importance of needle-tip optimization to enhance injector fuel flexibility.

Another relevant point of this chapter is the numerical methodology, which incorporates high-fidelity thermodynamic properties. In the proposed CFD methodology, the gas phase properties are obtained from NIST REFPROP and the liquid phase derived from PC-SAFT EoS. This represents an improvement to treat compressible fluids in comparison to conventional methods such as constant properties or cubic EoS. Consequently, this methodology is better suited to the high pressure gradients encountered in modern fuel injection systems [126]. In addition, the tabulation strategy provides a practical compromise between physical accuracy and computational efficiency. This strategy enables the use of advanced thermodynamics with engineering design time scales. Furthermore, the validation of the numerical framework against experimental data from ECN Spray C injector demonstrates the credibility of the modeling approach and supports the reliability of the flow predictions.

Despite these strengths, some limitations and uncertainties constrain the general applicability of the conclusions. A primary concern lies in the use of simulations at fixed needle lift positions to represent an inherently transient injection process. In real engine operation, the needle motion is a dynamic process. The associated flow evolves with time, interacting with pressure fluctuations, turbulence and changes on the cavitation structures [83][91]. By neglecting these transient effects, this study introduces uncertainty in the prediction of cavitation onset, evolution, collapse, flow stability and cycle-to-cycle variation [309][138]. The selected low and high lift positions provide useful reference points and support the injector pre-development phase. However, they do not fully capture the complexity of real injection events.

From a numerical perspective, the study employs URANS in the multiphase modeling framework. The use of a homogeneous mixture model along with a diffuse interface approximation, simplifies the physical representation of phase interactions. Under this approach, the phases are treated as interpenetrating continua and avoid explicit interface tracking. These assumptions are common in engineering studies because of their computational efficiency. However, they may limit the accuracy of predictions related to resolution of turbulent structures, bubble dynamics, phase distribution and local thermodynamic non-equilibrium effects [230]. Furthermore, the exclusion of dissolved non-condensable gases in the fuel may affect the realism of the predicted cavitation behavior. Neglecting these gases can alter predictions of bubbles inception, growth and collapse dynamics [18][289]. Although higher fidelity approaches could provide deeper insight into these phenomena, their substantially higher computational cost remains a major drawback for most industrial applications that require rapid and iterative design decisions.

Another important limitation concerns the lack of geometric transparency. Due to confidentiality constrains, the exact dimensions of the injector and needle geometries are not disclosed. This decision is admissible in an industrial collaboration context. However, it restricts reproducibility and limits the ability of other research to verify or build upon the findings. This absence of transparency also makes it difficult to assess the sensitivity of the results to specific geometric parameters such as angles, curvature and sac volumetric variations. Besides, the operating conditions considered in this study are also relatively narrow. This also restricts the applicability of the conclusions to a broader range of real-world conditions, where variations such as fuel properties and injection pressures are common.

In conclusion, the work provides a valuable foundation and contributes to the ongoing effort to develop more efficient and flexible fuel injection system for marine applications. Future work could address some limitations of this chapter by incorporating fully transient simulations with dynamic needle motion to better represent real injection events. Furthermore, enhancements to the multiphase modeling framework could improve the physical realism. However, this level of detail is not relevant in the pre-development design phase, where fast and reliable predictions are more relevant than a high fidelity approach. This deeper insight into the physical phenomena would be relevant in a later stage of the development phase.

Chapter 4

Cavitation prediction for Diesel Marine injectors via CFD-assisted Machine learning surrogate model

4.1 Introduction

The dual-fuel and Diesel-only operation requirement of the single Diesel marine injector presents obstacles in the areas of injector design and durability, especially in terms of cavitation. Cavitation in Diesel injectors has both detrimental and beneficial effects on the performance. It increases hydraulic resistance and causes flow instability within the injector leading to issues such as noise, fuel spray distortion, increased emissions and erosion of the nozzle wall [42, 34, 15]. However, adjustments in injector design can mitigate negative effects by reducing cavitation volume and improve the discharge coefficient [54]. In contrast, cavitation can also enhance spray atomization due to the breakup of fuel into finer droplets and improving the mixing with air, which is crucial for efficient combustion and reduced emissions [90, 35].

The optimization of nozzle geometry could minimize those undesirable effects. The shape and size of the injector nozzle and the arrangement of nozzle holes significantly affect cavitation patterns and flow characteristics, with certain designs reducing negative effects [82]. The movement of the injector needle, including its speed and position, also affects cavitation inception and development [309]. At low needle lifts, cavitation is more pronounced due to increased turbulence and vortex formation [48]. As the needle lift increases, the flow becomes more uniform, reducing cavitation occurrences [227, 196].

Over the past decades, extensive research efforts have been conducted to clarify in-nozzle flow during fuel injection. Numerical simulations and experimental measurements have demonstrated the impact of injector design and needle dynamics on cavitation. However, that characterization can be challenging and time consuming in fuel injectors. In particular, the high fidelity internal flow simulations require significant computational resources, detailed injector geometry, precise needle motion data and robust validation against experimental measurements, which may not always be available [20, 226]. Even simpler models such as RANS, which can provide reasonable accuracy at lower computational cost, require careful calibration to ensure reliable results and thus make their usage challenging in some routine engineering tasks.

The integration of ML with CFD models could enhance the predictive accuracy of cavitation patterns by learning to predict the flow field from simulated results. This joint workflow is particularly useful in scenarios where data is sparse, as it can enforce initial and boundary conditions through the ML model and thus reduce reliance on extensive simulation data. Moreover, they can support optimization tasks, which aim the understanding of the sensibility of each design parameter and the conditions more prone to enhance cavitation. Hence, they achieve speedups of several orders of magnitude compared to CFD, which can take days or weeks per simulation and therefore, enable efficient exploration of large design spaces.

However, one of the primary challenges in applying ML to fluid dynamics is the scarcity of training data, which can limit model generalization. ML models may not accurately predict outcomes for scenarios outside their training data, especially for novel injector geometries or extreme operation conditions. They are best used as surrogates or in combination with CFD, rather than outright replacements.

In the literature, only a few studies have explored the combination of ML methods and CFD simulation in order to analyze injectors. To the best of the author's knowledge, an approach to modeling the in-flow of marine Diesel injectors that use ML methods trained with data from CFD simulations has not been published. Unlike the studies of Mondal et al. [158] and Hwang et al. [101] that mainly focus on the spray simulations of a light-duty injector under different operation conditions, this study aims to obtain a tool that permits rapid assessment of cavitation for parametrically related marine injector designs. Varying designs is an inherently more complex task than modeling a fixed geometry with changing operational conditions because of the dimensionality increment. Each design leads to more complex feature interactions and non-linear relationships.

Besides, the relationship between scalar input parameter and image characteristics is highly non-linear due to the dimensional discrepancy between the input and output spaces. This mismatch makes increases the complexity of the learning task and makes it challenging for the models to identify meaningful pattern from the dataset. To this end, this current chapter presents the development and investigates the feasibility of CFD-assisted ML surrogate models tailored to marine injector design optimization. Particular emphasis is placed on the challenging to map relationships between low-dimensional scalar and image based cavitation representations, especially on limited datasets. Consequently, the study is structured as proof-of-concept surrogate modeling for rapid cavitation assessment rather than conducting an exhaustive CFD parametric optimization study or a universally generalized cavitation predictor.

The surrogate models evaluated in this chapter are schematically depicted in Figure 4.1. The two Deep Neural Networks (DNN) and a Generative Model (GM) are compared and validated in terms of trade-offs in accuracy and interpretability. The most promising models demonstrate the feasibility of rapid cavitation estimation within the investigated injector design space, leveraging both ML and CFD in the most effective strategy and accelerating the design cycle.

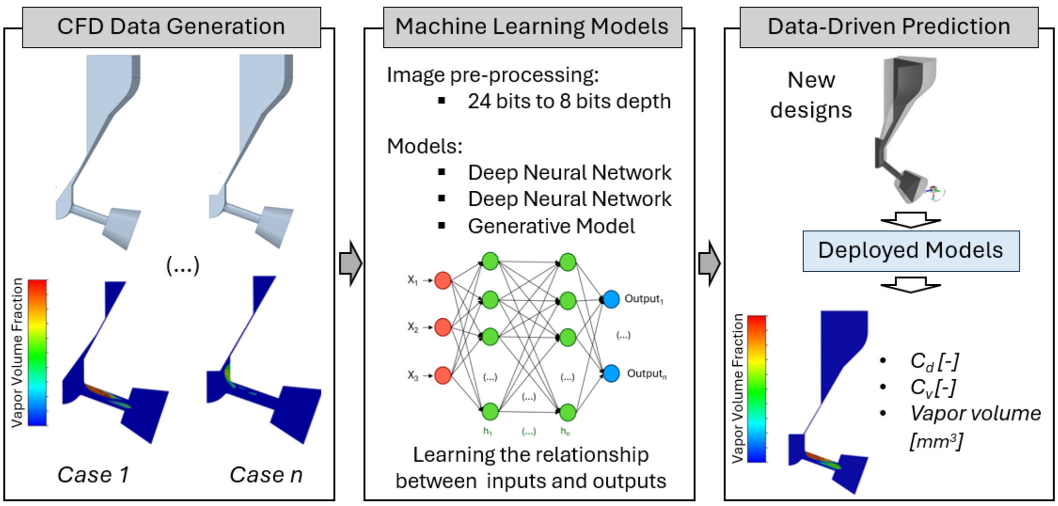

Figure 4.1: Conceptual representation of the CFD-assisted ML framework

4.2 CFD Numerical simulations

The generation of data for training, testing, and validation was performed by using the commercial software ANSYS Fluent©. The main modeling details were discussed in Chapter 2 and Chapter 3 and are summarized in the following subchapter.

4.2.1 Injector Designs and data sampling

The investigated design space was defined through three injector design parameters selected based on their influence on the cavitation behavior: needle-tip geometry, nozzle conicity and needle lift. These parameters directly affect the local pressure gradients, flow separation and contraction phenomena responsible for cavitation inception and vapor-cloud evolution with the injector nozzle. The injector Base Design (BD) and modifications on the needle-tip were discussed in Chapter 3. Figure 4.2 illustrates the geometrical modifications, where the relationship between inlet diameter D_{in} and outlet diameter D_{out} of the spray hole defines the conicity. In this study the conicity varies from 0 to 4.

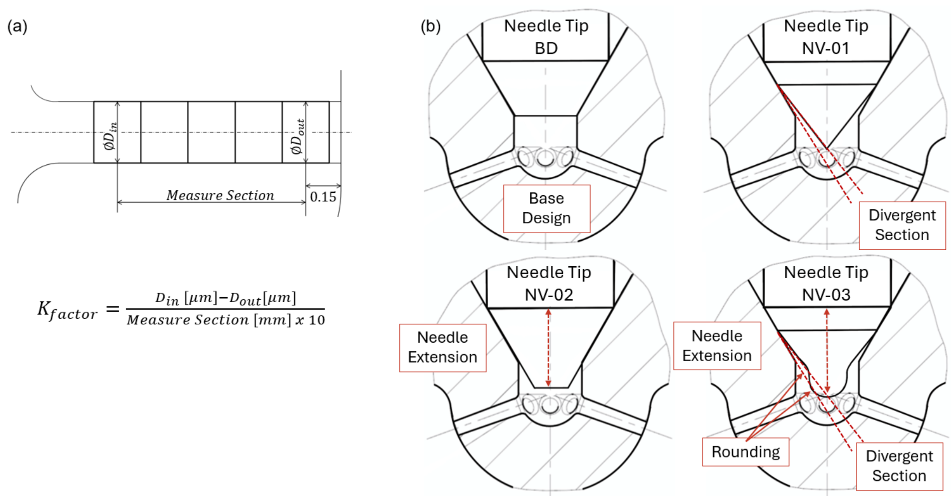

Figure 4.2: Schematic illustration of the injector designs modifications: (a) conicity definition; (b) base design and needle-tip modifications.

The needle lift varies from 54μm to 480μm. The choice for this range of variation for the needle lift was based on the real application of the BD, covering the maximum lift in dual-fuel and Diesel-only mode. Besides, the three design parameters were sampled via the Latin-Hypercube Sampling (LHS). LHS is a Design of Experiment (DoE) approach, tied to the Monte Carlo method. This technique ensures a good representation of the entire range of each variable with a reduced number of samples due to the stratification of the input probability distribution and is therefore a reliable alternative to Random Sampling and Stratified Sampling [95, 96]. A total of 59 CFD simulations were generated using LHS to span the selected injector design parameters space as illustrated in Figure 4.3. The number of samples was selected as a compromise between parameter space coverage and the computational cost associated with the CFD simulations. The complete list of the cases evaluated in this work is detailed in Table B.1 in Appendix B.

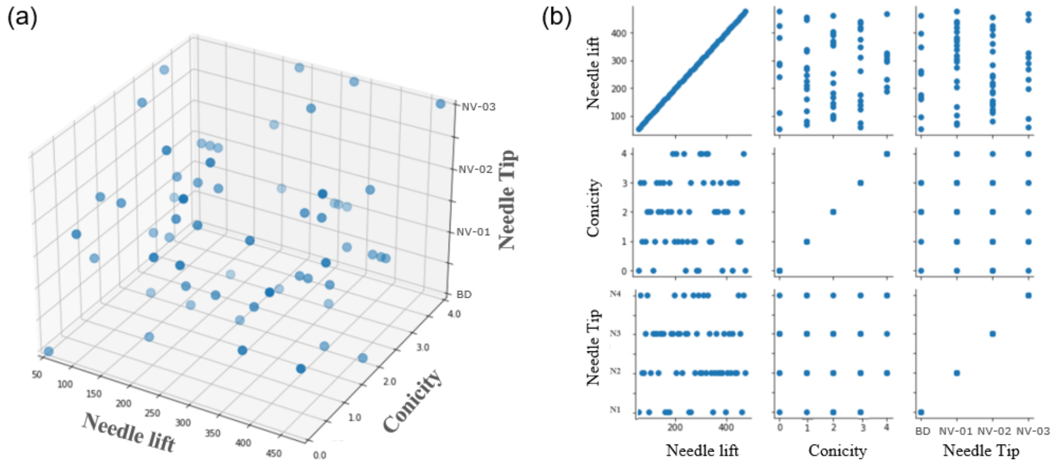

Figure 4.3: Sample points over the design region from the Latin Hyperbolic Sampling (a) 3D projection, (b) 2D projection.

4.2.2 Simulation setup of the internal flow

Each of the 59 designs was modeled as a 1/7 sector of the injector, reducing the computational cost due to the existing symmetry. The computational domain was composed of an inlet, housing wall, needle wall, side surfaces and discharge outlet volume of 1.5mm length with a conical shape. The refinement strategy of the unstructured hexahedral mesh was based on the strict quality criteria and Taylor micro-scales explained in Chapter 3.3, where the maximum mesh resolution inside the injector spray hole was approximately 4.2 μm. Depending on the needle-tip and needle lift, the total cell count varies from 3M to 4.2M elements. Each CFD simulation required approximately 36-121 hours of computation time and were executed on the HPC computer cluster of the City St. Georges's University of London on three computer nodes, each one with 48 cores to simulate 0.3 ms of physical flow time.

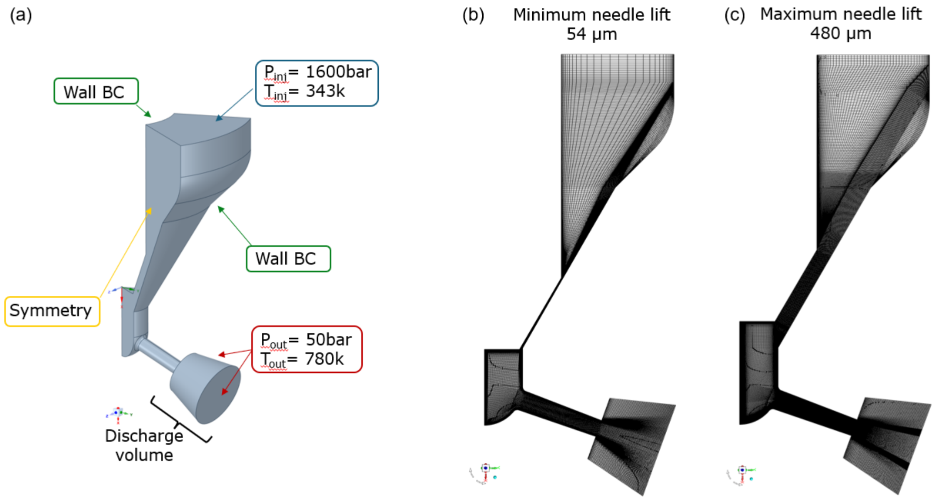

Figure 4.4: (a) Computational domain and boundary conditions, (b) mesh refinement strategy.

The boundary conditions were kept constant in all simulations and the modeling approach has been described in Chapter 2 and subchapter 3.3. The liquid n-dodecane, with 1600 bar pressure and a temperature of 343 K at the inlet, is injected into a nitrogen-filled discharge volume with an ambient pressure of 50 bar and a temperature of 780 K. The nozzle walls are considered adiabatic and the side surfaces as symmetrical boundary condition.

4.3 Image pre-processing and Machine learning models

The following section provides an overview of the pre-processing of the images and the applied ML methods: DNN and GM. All computations were carried out on a workstation computer with an AMD Ryzen 9 7900X 12-Core 24-Thread 4.7 GHz processor, GeForce RTX 5080 (NVIDIA 16 GB RAM) and 64 GB DDR5 RAM.

4.3.1 Image pre-processing

The color of an image can be described in the three primary light colors by specifying the intensity of red, green, and blue (RGB). In digital images, RGB is the most common colour space representation, where each color channel determines the intensity of that color in a pixel. The number of bits assigned to each RGB component determines how many different shades of that color can be represented. The color depth refers to the number of bits of each RGB component assigned to each pixel and a higher value allows more accurate and vivid color representation. In summa, an image with 8 bits per component, the most usual, has a color depth of 24 bits per pixel, allowing 256 possibilities for each color and a total of 16,777,216 true colors.

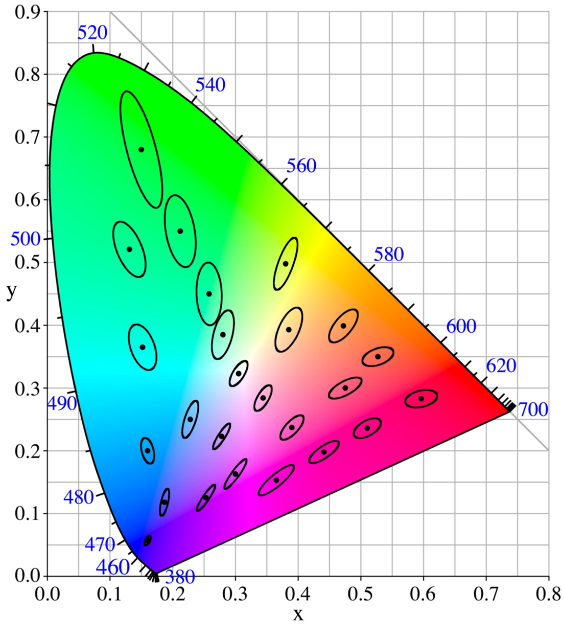

Figure 4.5: Standard deviations of chromaticity sensibility that the human eye can capture proposed by MacAdam [147], where the range of colors where added to the original black and white image [278].

While the color depth is a technical limit, the human perception of color differences is not uniform across all colors. MacAdam [147] studied the sensibility of the human eye to color difference, describing the limits on color discrimination which are known as MacAdam ellipses. The chromaticity differences proposed by MacAdam [147] are illustrated in Figure 4.5, where the position and size of the ellipses corresponds to the regions of noticeable difference of color. Larger ellipses indicate the eye's need for larger color differences to perceive a change [78].

Based on that, the images used in this work were reduced from 24 bits to 8 bits depth, applying a total of 256 true colors. This deepness reduction brings minimal adverse visual loss, while it simplifies the data representation for the ML training. Reducing image depth means fewer output channels and less information per pixel. For the neural network, the learning process becomes simpler and therefore, the complexity and computational cost decrease. The model can process the data faster, reduce the memory footprint, and enable faster processing of floating-point operation while maintaining model accuracy [183]. Besides, the lower depth highlights the essential features, especially when the task does not require full color information. The neural network may be able to focus on the most important patterns and structures in the image, improving its ability to predict images from scalar values and contributing to a better generalization.

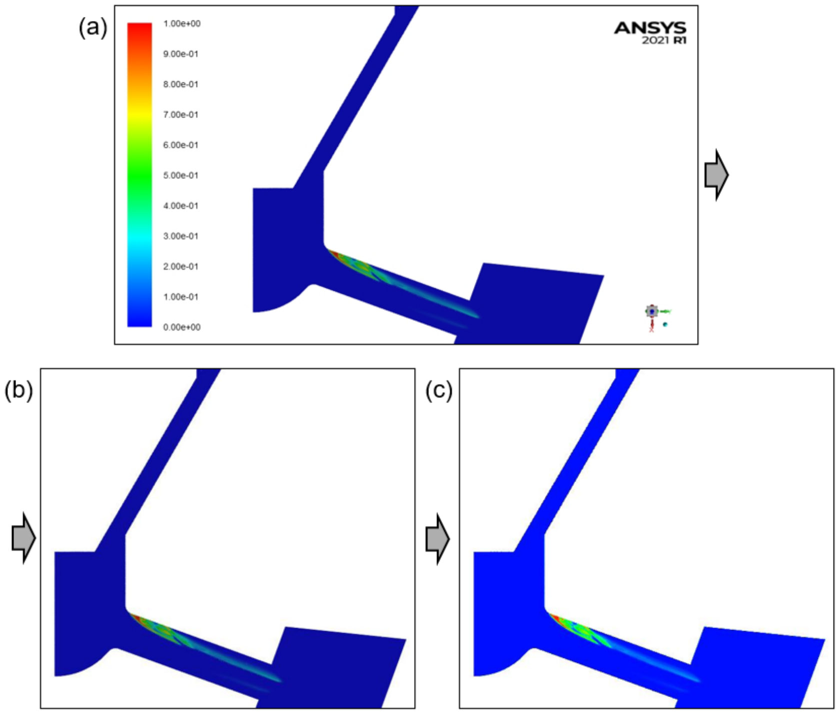

Figure 4.6: Stages of the image pre-processing: (a) Original images result of the CFD simulation, (b) Reduced area of original image in 24 bits, (c) Conversion to 8 bits depth.

All stages of the image pre-processing used in this work are illustrated in Figure 4.6 and Figure 4.7. First, the contour plot of the n-dodecane Vapor Volume Fraction (VVF) distribution at the axial plane was stored as an image for all CFD simulations. The area of the original image (Figure 4.6a) was reduced (Figure 4.6b), eliminating the color bar and the excess of areas that will not bring any additional information. Then, the original color bar was extracted and converted to 256 true colors, creating the 8 bit color palette. Figure 4.6c shows a representation of the CFD image converted to 8 bit depth and their colors mapped to the 8 bit color palette. Besides some small differences in color shading, the two images (Figure4.6b and Figure 4.6c) are identical for the human eye comparison, where all information regarding the VVF distribution is preserved with the image depth reduction.

Then, the 8 bit images are converted to a grayscale representation as shown in Figure 4.7a. Grayscale images have only one channel (intensity), while color images typically have three channels (RGB) [270]. This simplification further reduces the computational cost and complexity of the training process, allowing models to train

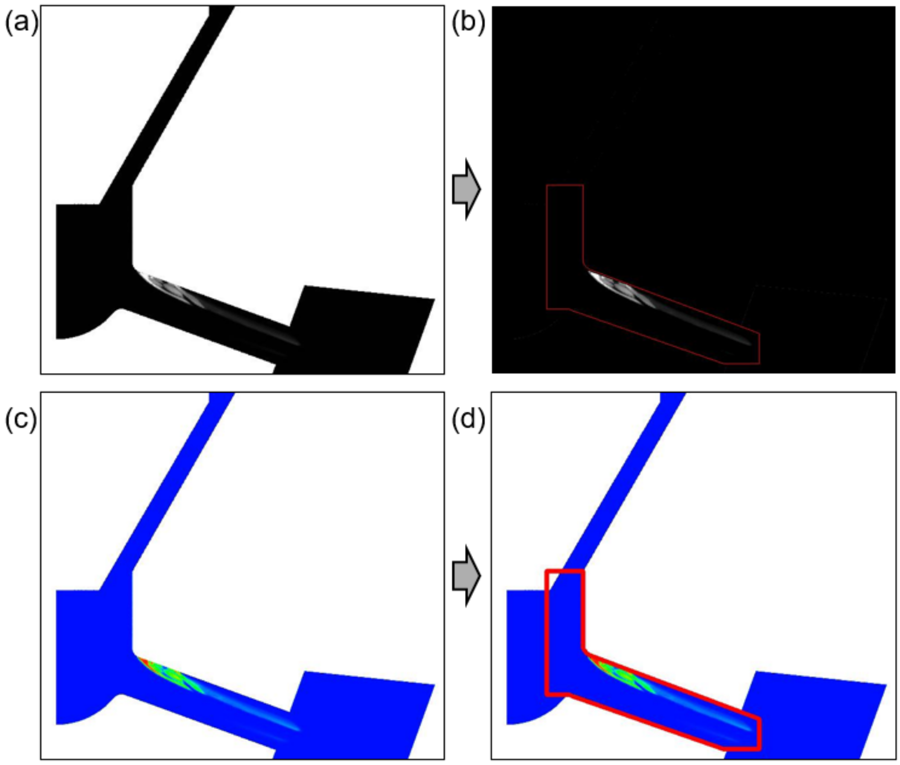

Figure 4.7: Stages of the image pre-processing: (a) 8 bits representation in grayscale, (b) background homogenization and area masking. The parallel representation of image pre-processing mapped to the 8 bits color palette for better visual interpretation: (c) 8 bits representation mapped to the 8 bits color palette, (d) placement of the mask area.

faster and with less memory. Besides, the background (”white” areas or pixel with intensity 255 in a grayscale image) and geometry profile (”black” areas or pixel with intensity 0 in a grayscale image) represent the non cavitation areas and are equivalent for the neural network training. So, those areas were mapped to ”black” (0 intensity in a grayscale) to reduce the complexity during the training, resulting in the final stage of the image pre-processing (Figure 4.7b without the red lines) for the GM. Moreover, in all 59 cases, cavitation was detected within the region around the spray hole inlet and inside the spray hole. Hence, a mask area was delimited based on the average overlap of those images as illustrated by the red lines in Figure 4.7b and d). The pixels inside the mask area were stored in an array and used as output to train the DNN. This strategy reduces the output size for the DNN, lowering the dimensional differences between input and output.

All image manipulations described above reduce the complexity and time for the training process considerably. On average each training of the DNN took 2 hours and 4 hours for the GM. This low time for training speeds up the interactive process of adjusting the hyperparameter for each model.

4.3.2 Deep Neural Network Architectures

Two feedforward neural networks were employed in this work, one has the objective to predict quantitatively the cavitation volume and the performance coefficients (discharge and velocity), and the second, to predict the location of the cavitation morphology via images. The DNNs consist of hierarchical layers: input, hidden and output layers. The first DNN presents a 3-x-3 architecture, where x indicates the number of neurons in the hidden layers. The input layer consists of 3 variables: conicity, needle tip type and needle lift. The output is also composed of three variables, which are discharge coefficient (C_d), velocity coefficient (C_v) and vapor volume. Figure 4.8 illustrates the layout of the first DNN.

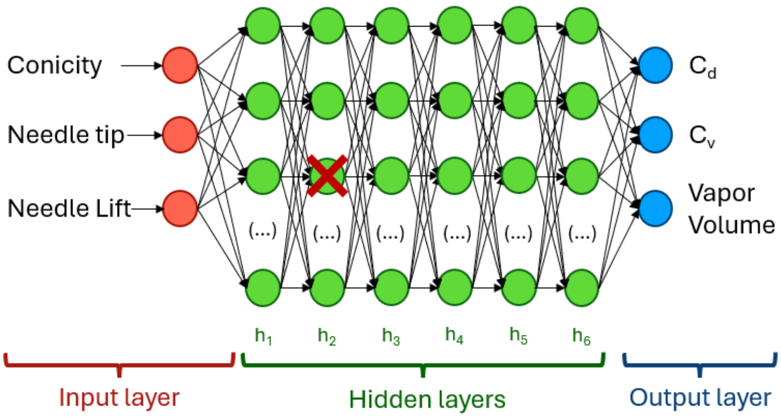

Figure 4.8: Representation of the DNN for quantitatively values prediction that consisted of one input layer, six hidden layers and one output layer with the dropout nodes symbolized by red marks.

During the DNN training the number of hidden layers was tested interactively, where 6 hidden layers provided the optimal balance between accuracy and efficiency. The dropout rate was included in the third hidden layer with a 30% probability as indicatively represented by the red marks in Figure 4.8. The model loss was calculated via MAPE, measuring the mean absolute percentage error between predicted and actual values.

The second DNN is also a deep fully connected feedforward neural network, presenting 3-x-1 architecture as depicted in Figure 4.9 and a complementary description is provided in Appendix C. The input layer was kept the same and the output layer consisted of one vector with 27556 pixels that constitute the vapor volume fraction as an image. In total, 11 hidden layers, with a dropout rate of 30% probability applied in two layers, provided the best compromise between accuracy and efficiency.

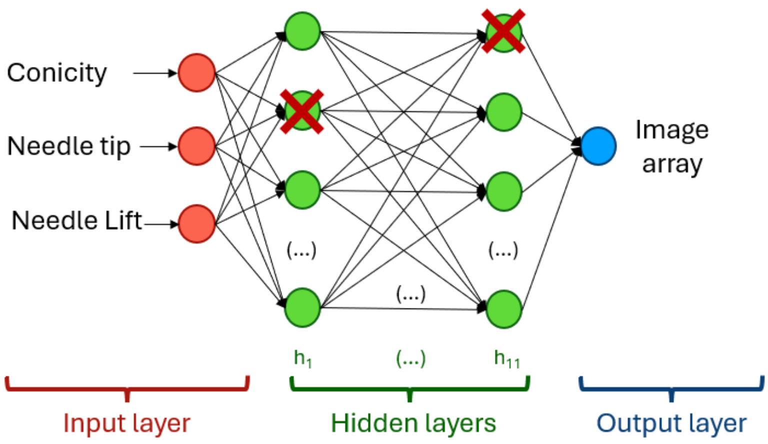

Figure 4.9: Representation of the DNN for image prediction that consisted of one input layer, eleven hidden layers and one output layer with dropout nodes symbolized by red marks.

Besides, the MSE was the selected evaluation metric to measure the model loss, averaging the squared difference between predicted and actual values.

In both DNNs, the LeakyReLU activation function was utilized to introduce non-linearity. Early stopping was employed to prevent overfitting as regularization technique and handle noisy data. Furthermore, the data was normalized to the range [0, 1] which helps to promote sparsity and accelerate convergence. Prior to the training, the data was randomly split into two datasets with 80% for training and 20% for testing. Proper data splitting is essential for unbiased evaluation, the prevention of overfitting and the mitigation of data poisoning.

4.3.3 Generative Model Architecture

The GM employed in this work also aims to predict the location of the cavitation morphology via images. The input layer was the same as the previous network, composed of a latent vector with 3 components: conicity, needle tip, and needle shape. This vector is transformed into a spatial feature map as illustrated in Figure 4.10.

The GM architecture begins converting the input layer into a dense (fully connected) layer without bias, expanding the latent vector to a 66x76 feature map. This stage was followed by LeakyReLU activation, dropout for regularization and reshaping the feature map into a 3D tensor (66, 76, 1). Then, the GM performed progressive upsampling using a series of transposed convolutional layers. The first layer upsamples the feature map to (132, 152, 16), and the second brings it to

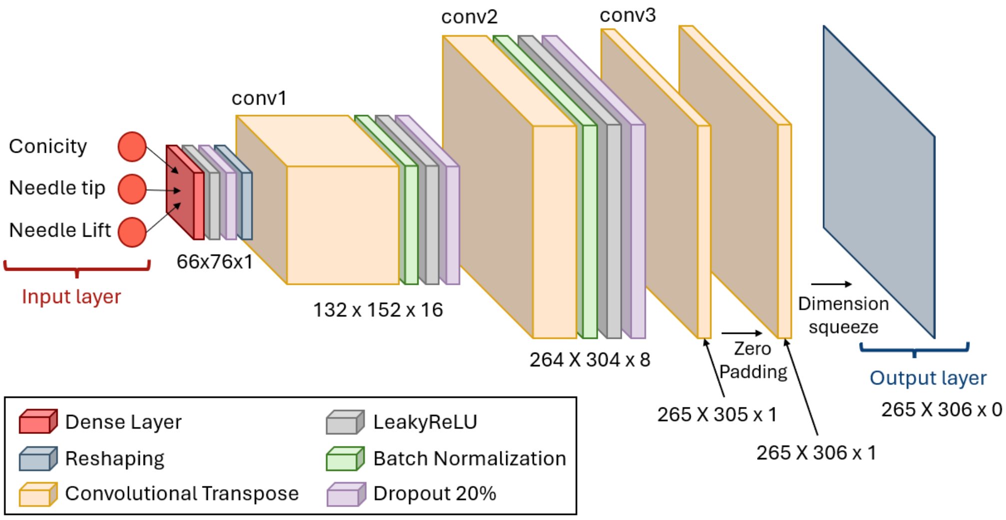

Figure 4.10: Representation of the GM architecture for image prediction that consists of three transposed convolutional layers.

(264, 304, 8). In those layers, the batch normalization, LeakyReLU activation, and dropout were incorporated to maintain stable activation and contribute to the model generalization. The strides and padding were defined as (2, 2) and 'same' in both layers with a (3, 3) kernel.

The final convolutional transposed layer contributed to nearing the desired image size by adjusting the feature map to (265, 305, 1) with a sigmoid activation, a unit stride and a 'valid' padding for a (2, 2) kernel. A zero-padding is added to fine-tune the dimensions, and a lambda layer is used to squeeze the channel dimension, resulting in the final image output. A complementary description of the GM is provided in Appendix C.

4.4 Results and discussion

The following section evaluate the performance of the ML surrogate models. In this chapter, model robustness refers to the capability of the ML models to consistently reproduce the cavitation behavior across the sampled design space, including global flow coefficients, vapor volume trends and cavitation morphology.

4.4.1 Predicting flow coefficients and vapor volume

The training progress and performance of the first DNN in terms of the loss and accuracy are illustrated in Figure 4.11. In simple words, the model loss measures the distance of the predictions from the true values, while accuracy shows the proportion of correct predictions. The steadily decreasing loss curve, in Figure 4.11a, for the training and test data indicates a good training process, where initially issues like overfitting and underfitting were mitigated. As the curves reach a plateau, this indicated that the model has stopped learning. The MAPE of the training data and test data are respectively 3.36 and 6.28. Further training could lead to overfitting issues and due to the early stop technique included in the models, the training terminates after 200 similar results.

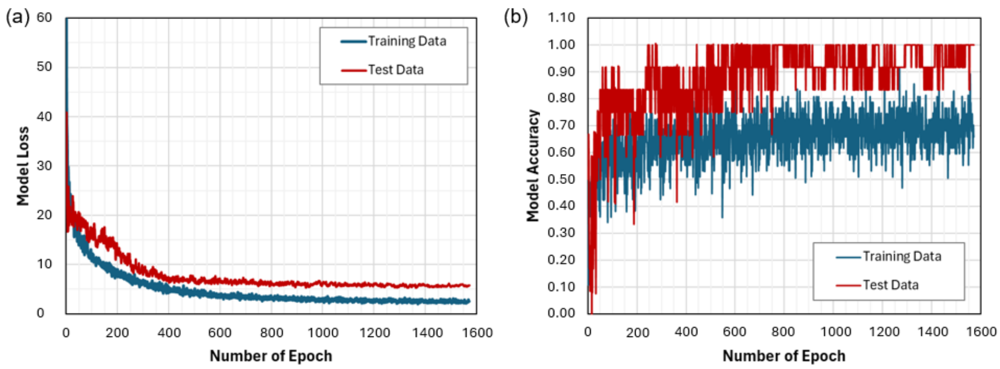

Figure 4.11: Training and test-data (a) loss curve of the DNN as a function of the number of Epochs, (b) accuracy curve of DNN as a function of the number of Epochs.

Moreover, the model accuracy is represented in Figure 4.11b. The training and test accuracy continues to increase in the beginning for the early epochs, indicating a good learning process in the training data, while the test data indicated a good progression of generalization of the unseen data. The two curves reached a plateau, where the training data and test data exhibit an average accuracy of 0.917 and 0.671, respectively. This accuracy difference between the training data and test data could be an indication of overfitting, where the model may start to memorize the training data, including noise and irrelevant patterns.

In addition, the accuracy values present high oscillations during the training. These oscillations can be caused by factors such as quantization effects, noisy training data, or issues with model or training configuration [168]. The main issues that could originate from the neural network architecture were already mitigated. This instabilities cannot originate from inappropriate learning rates since high oscillations around the minimum of the loss function were not detected as shown in Figure 4.11a. The initial learning rate used in the training was 0.00005 combined with a decay rate, which allows the network to shift from rapid exploration to fine-tuned convergence, reducing oscillations due to the rate of learning. Besides, the LeakyReLU activation function eliminates the freezing weights during training, which is another possible source of high oscillations.

Besides, the limitation or imbalance training data is the main reason for the network to memorize specific examples rather than generalize [134]. This behavior can be inspected in terms of the linear regressions of the training and test data categorized by each neuron in the output layer as shown in Figures 4.12, 4.13 and 4.14.

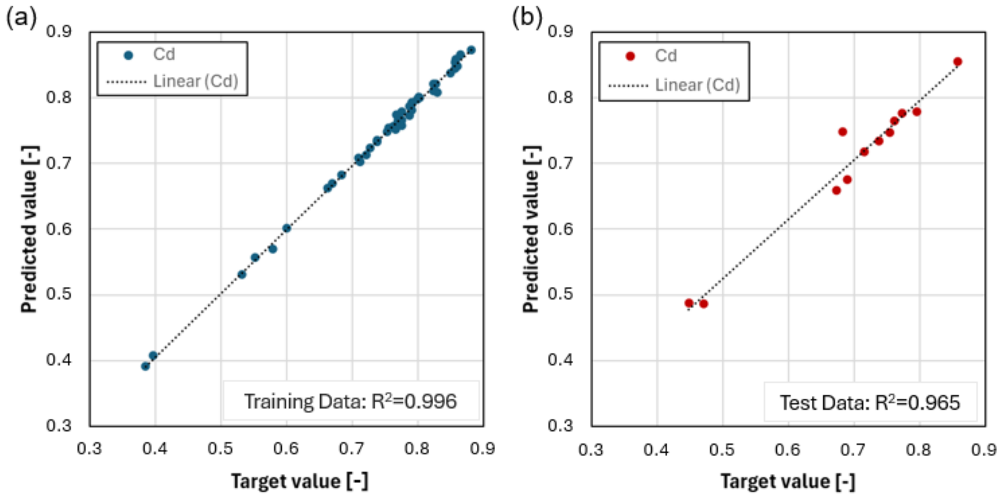

Figure 4.12: Individual contribution of the Discharge coefficient values to the DNN performance in terms of linear regression: (a) Training values (b) Test values.

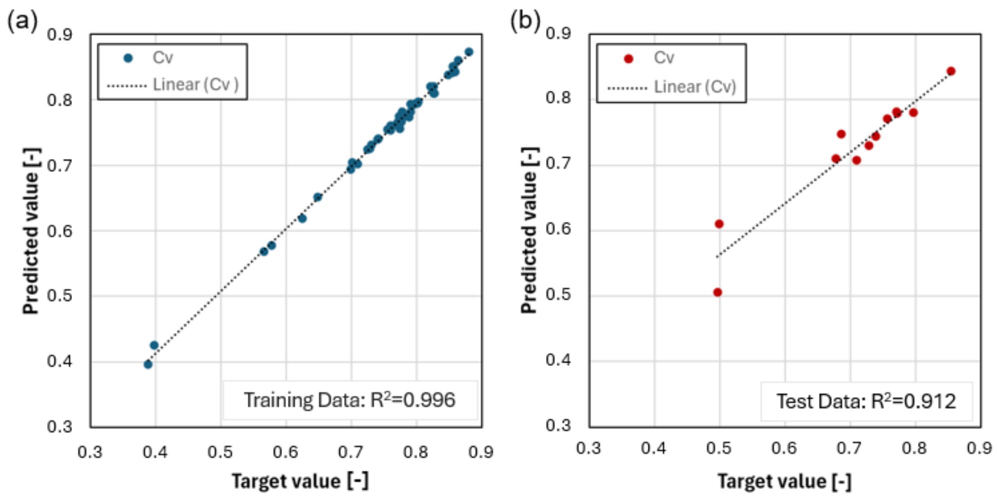

Figure 4.13: Individual contribution of the Velocity coefficient values to the DNN performance in terms of linear regression: (a) Training values (b) Test values.

The regression plots demonstrate an excellent correlation between the output values and targets during the training of the C_d and C_v, with a Coefficient of Determination R^2 of 0.996 for both cases. The training predictions show minimal minor discrepancies and are essentially coinciding with a diagonal line as illustrated in Figure 4.12a and Figure 4.13a). The test predictions, in both cases, replicate the same behavior with minimal over predictions, resulting in a Coefficient of Determination R^2 above 0.91. In other words, the C_d and C_v are well predicted by the DNN, with high accuracy. The precision is superior to what is shown on Figure 4.11b, confirming a good training procedure and enough data sampling for those classes.

However, the vapor volume does not present such a good performance as the previous classes as shown in Figure 4.14. The training data presents a good correlation, with a Coefficient of Determination R^2 of 0.986. Nevertheless, the test data indicates overfitting due to the high discrepancy of Coefficient of Determination R^2, being only 0.628. This class is clearly under-represented which causes the overall reduced DNN accuracy and value oscillations.

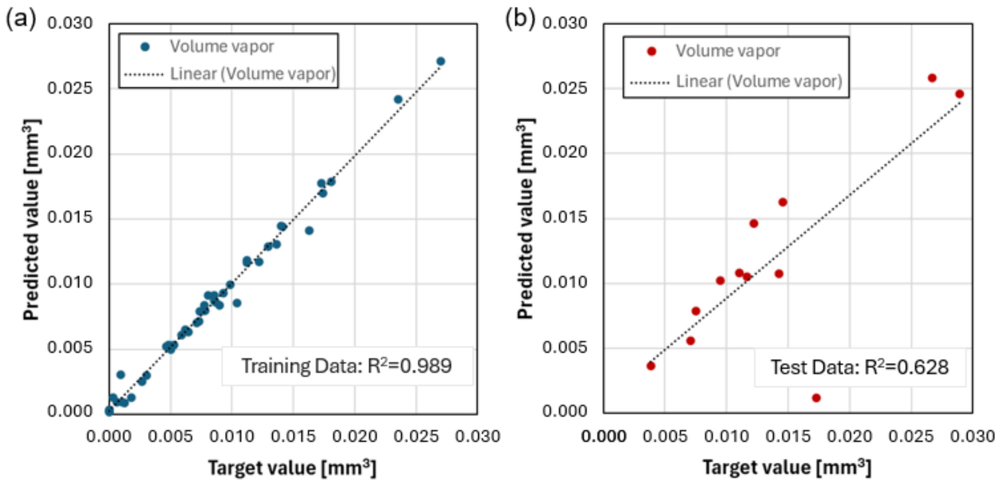

Figure 4.14: Individual contribution of the vapor volume values to the DNN performance in terms of linear regression: (a) Training values (b) Test values.

Very low data values, as in the case of the vapor volume, can present significant issues during the evaluation of the neural network. In cases where actual values are close to zero, even a slight overestimation can result in a very large or undefined percentage error, unnecessarily influencing the overall MAPE score. Other loss functions like Mean Absolute Error or Root Mean Squared Error were also tested, without any improvement. Hence, an expansion of the dataset is the only solution to mitigate the reduced accuracy and value oscillations.

Nevertheless, the model was structured to be incorporated in the pre-development design phase of marine injectors. The 67% accuracy is an acceptable compromise at this initial stage, especially when the computational cost and time are taken into consideration. Once the DNN is trained, those predictions are carried out in milliseconds. The reduced accuracy is only driven by the vapor volume while presenting the C_d and C_v with an elevated precision (above 90%) as illustrated in Table 4.1. Besides, those predictions, in complement to the location of the vapor clouds that will be presented in the next section, allow a full assessment of in-nozzle cavitation.

Test Case [-]	**Target** C_d [-]	**Predicted** C_d [-]	**Target** C_v [-]	**Predicted** C_v [-]	**Target VV** [mm^3]	**Predicted VV** [mm^3]
3	0.673	0.659	0.678	0.710	0.0146	0.0163
9	0.762	0.764	0.771	0.782	0.0142	0.0107
13	0.448	0.488	0.496	0.506	0.0290	0.0246
36	0.690	0.675	0.709	0.707	0.0122	0.0146
47	0.737	0.735	0.740	0.744	0.0095	0.0102

Table 4.1: Target and DNN predicted values of C_d, C_v and Vapor Volume (VV) for selected test cases.

4.4.2 Predicting cavitation morphology

The cavitation morphology and location were predicted via two models: DNN and GM. These predictions were carried out to reconstruct the VVF distribution for different nozzle geometries. The training progress and performance for both models are evaluated in respect of the model loss versus epochs for the training and test data as shown in Figure 4.15 and Figure 4.16. The model's architecture and early stopping strategies result in a different optimal number of epochs to prevent overfitting. The progressive training loss decreasing and converging to a stable minimum indicates that the models are effectively learning the patterns in the training data. Simultaneously, the decrement of test loss suggests that the models are generalizing well to unseen data. In both cases, the magnitude of the loss values reaches low values in the final plateau. The MSE of the training data and test data are respectively 0.007 and 0.034 for the DNN (Figure 4.15). The loss of the GM is also measured via MSE, where the training data and test data are respectively 0.007 and 0.006 (Figure 4.16).

In the context of image processing, model accuracy cannot be directly quantified by metrics such as MSE or linear regression as presented in the previous subchapter. Those metrics focus on pixel-level aspects, which will undervalue the model

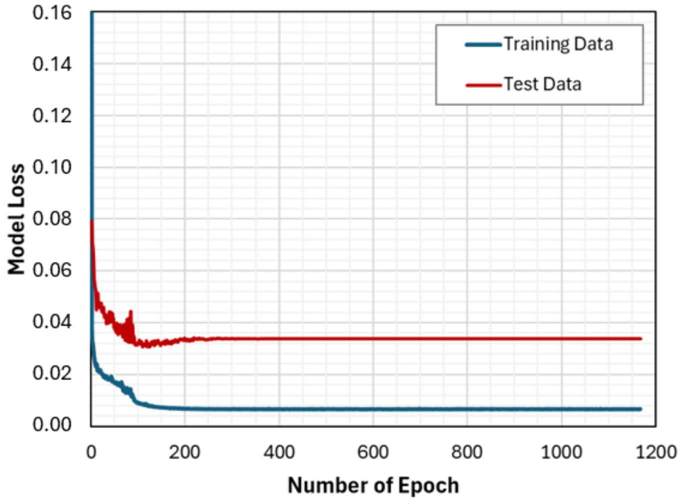

Figure 4.15: Training and test data loss curve as a function of the number of epochs for the DNN.

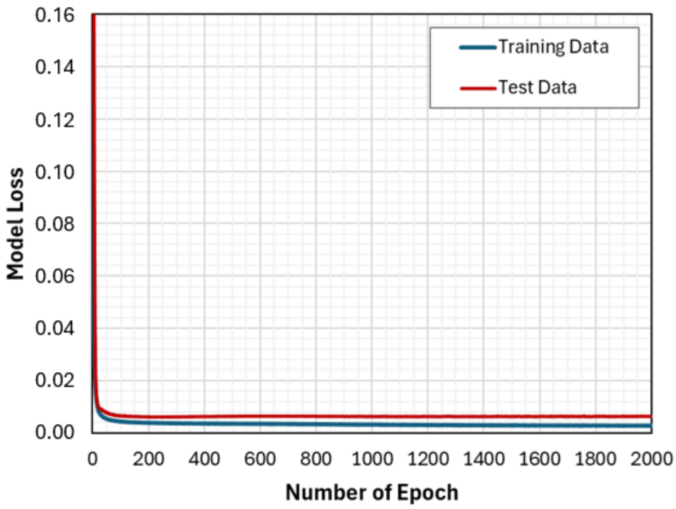

Figure 4.16: Training and test data loss curve as a function of the number of epochs for the GM.

and heavily penalize any deviation. Small changes or simplifications in the reconstructed output are acceptable if the model captures the essential features. Hence, image-based models are typically measured via structural similarity, evaluating the perceptual quality of the reconstructed images to the original input.

The quality of the neural network predictions can be assessed via a direct comparison with the CFD results for the test cases. Figures 4.17, 4.18, 4.19 and 4.20 illustrate an indicative comparison of VVF for two test cases. The grayscale predicted images were mapped to an 8 bit color palette and reconstructed to include the representative parts outside the mask area to facilitate the visual comparison and similarity associations.

The global agreement between the simulations and the neural network predictions are satisfactory related to the onset of cavitation and the location of the main vapor cloud. However, when the vapor intensity is taken into consideration, the precision of the prediction between the neural networks can be differentiated. First, the DNN can smoothy reproduce the VVF gradients and is covering its fraction range as illustrated in Figure 4.17b. Few isolated absolute differences are seen for the high vapor fractions (Figure 4.17c) inside the main vapor cloud. However, those minor discrepancies do not compromise the good performance of the DNN, especially when the fidelity to predict cavitation morphology is taken into consideration. This model covers the onset of cavitation and its main form along the spray hole very well while also predicting the small structure close to the spray hole exit. On the other hand, the GM results show a complete failure to predict the high fractions of vapor volume as seen in Figure 4.18b. The GM predicts the location of the onset of cavitation, the main cloud and the small structures location well. Nevertheless, the gradients of VVF were not possible to be visually recognized, where the cavitation areas are represented for a constant volume fraction share, approximately 0.60.

A second example of the neural network predictions is presented in Figures 4.19 and 4.20 for test case 47 and a similar conclusion can be drawn. Predicting images from scalar values poses several challenges for neural networks due to the inherent information gap: a single scalar value often lacks the richness required to fully capture the complexity of an image. The neural networks may struggle with generating high-resolution or detailed images from limited scalar inputs, where oversimplification of VVF gradients can be explained for the GM (Figure 4.20b). Besides, the cavitation area predicted by the GM is slightly larger than the reality, where an extra cloud is predicted close to the spray hole exit. In this case, more data and further training are still necessary to enhance the GM predictions, allowing the model to differentiate the higher vapor fractions.

From the observations in Figures 4.17, 4.18, 4.19 and 4.20, it can be concluded that the DNN model can achieve better generalization of the unseen data and accuracy than the GM. Moreover, the training progress does not present any instability, resulting in a constant and minimal loss for the training and test data (Figure 4.15). For these reasons, the DNN model proposed in this work is the suitable model for properly replicating the VVF in an early design phase for marine injectors similar to the design space that the DNN was trained on.

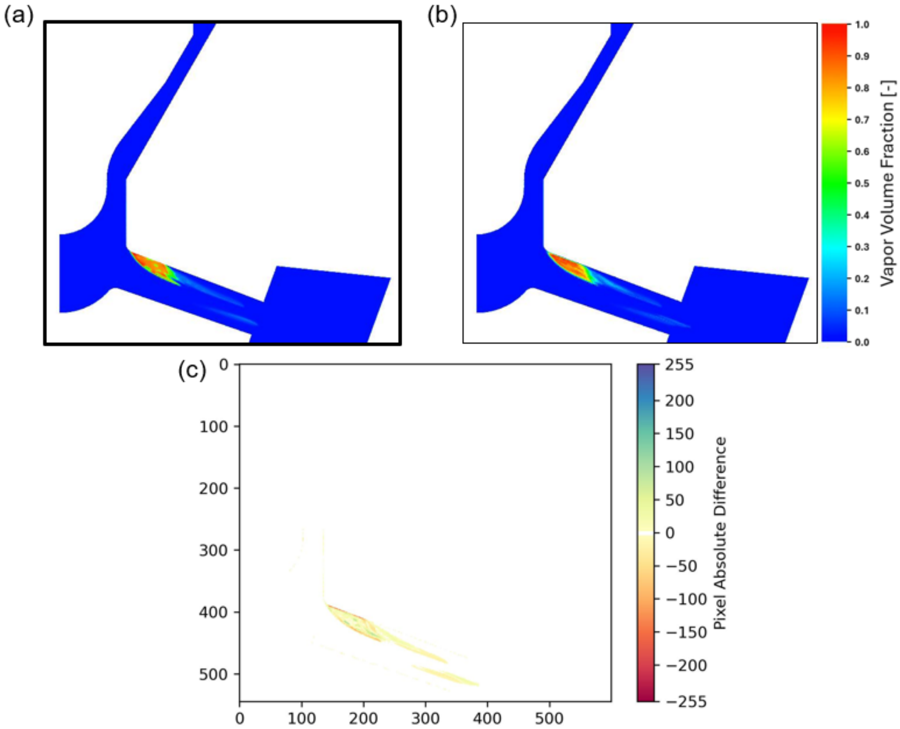

Figure 4.17: Evaluation of the performance of the DNN prediction for the test case 9: (a) VVF distribution from the CFD simulation in 8 bits depth resolution, (b) predicted VVF distribution via DNN, (c) pixel absolute difference in VVF distribution between the two images.

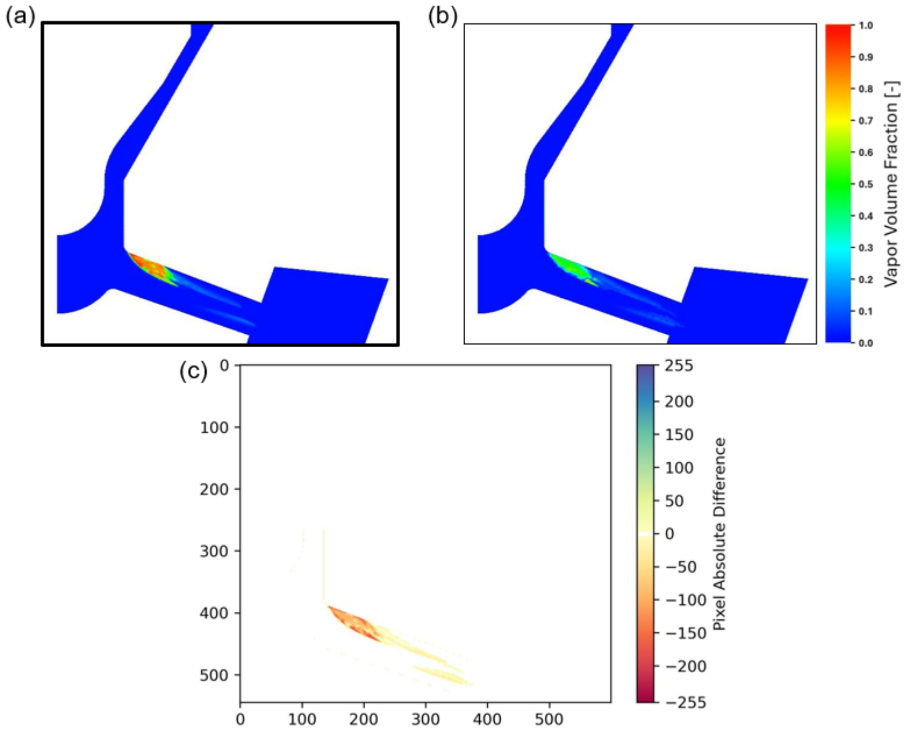

Figure 4.18: Evaluation of the performance of the GM prediction for the test case 9: (a) VVF distribution from the CFD simulation in 8 bits depth resolution, (b) predicted VVF distribution via GM, (c) pixel absolute difference in VVF distribution between the two images.

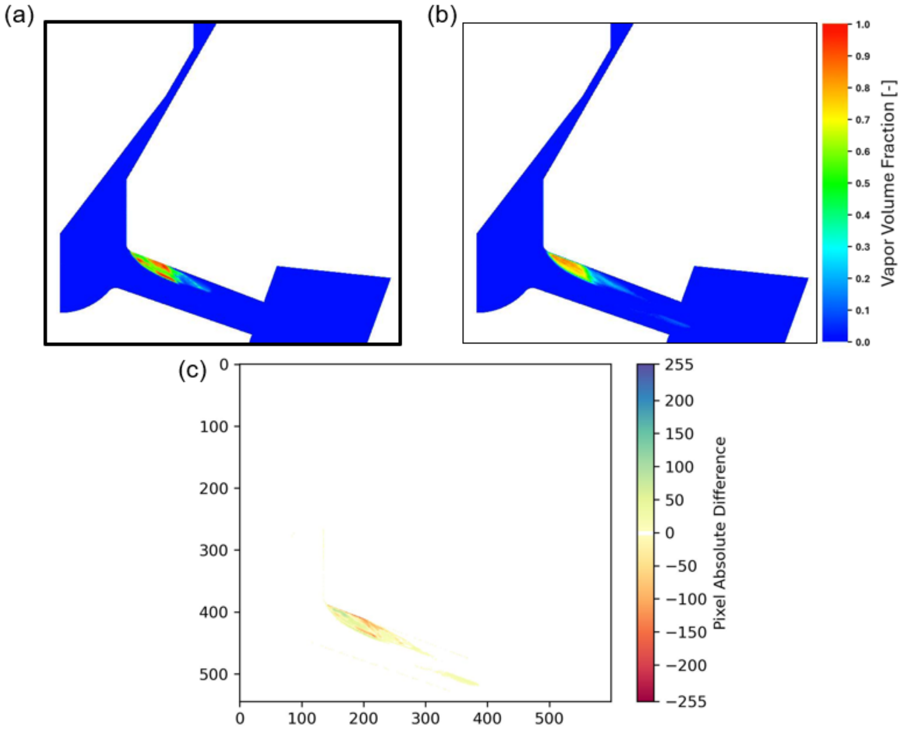

Figure 4.19: Evaluation of the performance of the DNN prediction for the test case 47: (a) VVF distribution from the CFD simulation in 8 bits depth resolution, (b) predicted VVF distribution via DNN, (c) pixel absolute difference in VVF distribution between the two images.

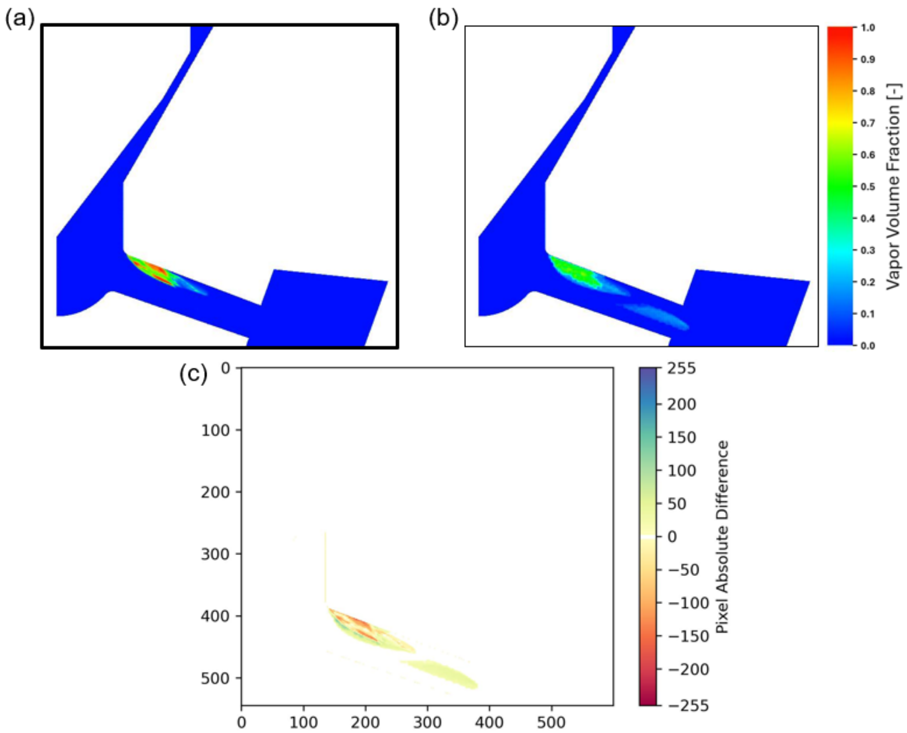

Figure 4.20: Evaluation of the performance of the GM prediction for the test case 47: (a) VVF distribution from the CFD simulation in 8 bits depth resolution, (b) predicted VVF distribution via GM, (c) pixel absolute difference in VVF distribution between the two images.

4.5 Conclusions from CFD-assisted Machine Learning for cavitation prediction

This chapter demonstrates the implementation and feasibility of using a limited CFD-generated dataset to train surrogate ML models capable of reproducing dominant cavitation trends within a marine injector design. Two DNNs and one GM learned patterns to predict flow coefficients and cavitation for marine Diesel injectors, focusing on the applicability of those neural networks to support the early design phase. Cavitation was characterized regarding the vapor volume as a scalar value and the contour plot of VVF, distinguishing the location and morphology of the vapor cloud. The three models were trained with data generated via CFD simulations. The LHS was used to select training data from CFD simulations and ensure a minimal sampling with a good distribution across all dimensions of the input space. The high dimensionality difference and computational cost of generating simulation data were reduced, while clustering or gaps from random sampling were avoided. In total 59 nozzle geometries were simulated via CFD under the same operation condition.

The input parameters were the same for the models: needle lift, conicity and needle tip. The first DNN predicts with high accuracy the C_v and C_d. However, the vapor volume presented a limited accuracy. This data class may is under-represented due to the absolute low data values, and an expansion of the dataset could mitigate this issue. Although the overall accuracy reaches only 67%, this precision is still acceptable for the model application goal, where the gain on prediction time compensates for the limited precision.

The second DNN and GM are image-based models used to predict the cavitation morphology from scalar values. Predicting images from scalar values with neural networks is challenging due to high output dimensionality, while scalar inputs are low-dimensional. This mismatch exponentially increases the model complexity and makes it challenging to distinguish meaningful patterns, especially when the dataset size is small. Reducing image depth from 24 bits to 8 bits can alleviate the curse of dimensionality, where fewer color values are possible to be mapped. This reduction makes the prediction task less complex and helps the model to focus on essential features.

Both models show good precision related to the onset of cavitation and the location of the main vapor cloud. However, the GM is insensible to high VVF values, resulting in blurry or oversimplified gradient variation. The requirement of a square area for the output puts in evidence the high-dimensional issues to maintain spatial smoothness in the predictions. In this case, only data augmentation can contribute to mitigating the current GM imprecision. On the other hand, DNN flexibility allowed to reduce the number of pixels on the output image due to the mask delimitation. This strategy has a positive impact on the quality of the predictions. The DNN can forecast the location, morphology and intensity of the VVF with elevated precision. Besides, the proposed CFD-assisted ML workflow is not inherently restricted to a single two-dimensional plane representation. The same methodology can be extended toward images of a three-dimensional view of flow fields representations, depending on the desired level of detail and engineering application.

Finally, the two DNNs give a complete overview of in-nozzle cavitation for marine injectors. They could be integrated into the early design phase for injectors in a similar geometries and parameter range represented within the training space. Besides, those DNNs exemplify how CFD and ML can supplement each other in an industrial environment, combining the accuracy of physics-based CFD simulations with the speed and adaptability of ML. A similar CFD result for geometries similar to the training dataset can be generated within seconds by the neural network, enabling real-time process optimization. The time gained by using the proposed ML surrogate models for initial design assessment allows the CFD simulation to be used more effectively in the later stages of the design phase, focusing on fine-tuning and validation of the most promising designs identified by the ML model.

4.6 Critical review

This section provides a critical reflection of the present chapter, which introduces a CFD-assisted ML framework for the prediction of cavitation behavior in marine Diesel injectors. The work addresses a relevant engineering challenge: the high computational cost associated with detailed cavitation simulations during the injector design and optimization. To mitigate this limitation, the proposed framework integrates CFD-generated datasets with ML surrogate models. This integration can enable a faster assessment of cavitation during the preliminary design phase. In addition, the chapter demonstrates strong technical competence in CFD modeling, image pre-processing and neural network implementation. In particular, the study tackles the challenging problem of reconstructing cavitation morphology images from a limited set of scalar input parameters, which constitutes a relevant contribution from a surrogate modeling perspective. Nevertheless, conceptual and methodological limitations reduce the robustness and generalization of the proposed framework in its current form.

One of the principal strengths of the chapter lies in its clear industrial motivation. Cavitation continues to represent a major challenge in fuel injection systems due to its influence on injector durability, hydraulic performance, spray atomization and emissions [33][35][99]. The selected geometrical parameters (needle lift, conicity and needle-tip geometry) are physical meaningful and directly influence local pressure gradients, flow contraction and vapor cloud development within the injector nozzle [48][92][151]. In complement, the adoption of LHS to generate the design points across the parameter space is also appropriate and demonstrates awareness of surrogate model sampling strategies from limited CFD datasets.

Furthermore, the image pre-processing methodology constitutes one of the strongest aspects of the chapter. The grayscale conversion, masking strategy and image-depth reduction are effectively implemented to reduce dimensionality and training complexity. As presented in the chapter, the predicted images successfully captures the dominant cavitation morphology by the DNN. Nevertheless, the chapter would benefit from a more explicit positioning of the images as a fully three-dimensional representation of the cavitating flow field.

Besides, at some points the work may lead the reader to interpret it as a cavitation-physics investigation, a generalized ML predictor, or a CFD optimization study. In practice, the work is most scientifically defensible when viewed as a feasibility oriented CFD-assisted surrogate modeling framework. Its central contribution lies in evaluating whether ML models can reconstruct dominant cavitation behavior from low-dimensional scalar input parameters under constrained dataset conditions. Hence, the proposed surrogate models should not be interpreted as a universal and transferrable cavitation predictor. This distinction should be clear because the strong dimensional mismatch between scalar inputs and image based outputs represents one of the key challenges addressed in this study.

Despite it merits, the neural network architectures employed in the chapter also present certain limitations. GM, particularly those based on convolutional architectures or latent-space compression techniques, generally outperform fully connected DNNs in image prediction and reconstruction tasks [304]. These approaches incorporate strong inductive bias, including spatial locality, translation invariance and parameter sharing, which typically improve data efficiency and generalization in image based applications [114][304]. However, when the available training dataset is very small, highly specialized or insufficient to support effective learning of convolutional filters, these architectural advantages may be diminished [115].

As discussed in this chapter, the DNN achieved better predictive performance by more closely fitting the specific input-output relationship present in the data. This outcome is particular plausible when the images are of relatively low dimensionality or when the features have already undergone substantial prepossessing or feature engineering such as the application of an additional mask that restrict the output space of the DNN. Although the DNN demonstrates satisfactory capability in reproducing cavitation onset and dominant vapor cloud morphology within the sampled design space. This performance may be more attributable to problem-specific characteristics, or insufficient training data relative to the complexity of the GM architecture rather than to a general advantage of DNNs in data constrain settings. Furthermore, the predictive capability of the DNN remains limited to interpolation within the investigated parameter space and cannot currently be generalized to substantially different injector geometries or operating conditions.

Another important point concerns the limited dataset size. Only 59 CFD simulations were generated for training and testing the ML models. Although the use of the LHS improves parameter space coverage and ensures better space-filling properties [175], the dataset remains relatively small for deep-learning applications involving high-dimensional image outputs. While the dataset size was defined based on previous studies reported in the literature, the chapter would have benefited from a dataset convergence analysis to justify its adequacy. As indicated by the observed overfitting behavior in the prediction of the scalar vapor volume, the current dataset may not be sufficiently representative relative to the complexity of the learning task. Therefore, a learning curve assessment should be included as part of the future work.

Overall, the chapter demonstrates the feasibility of using CFD-generated datasets to train ML surrogates models capable of reproducing dominant cavitation trends for marine injector design. The work represents a valuable proof-of-concept contribution toward CFD-assisted surrogate modeling and addresses the challenging scalar to image learning problem despite the limited size of the available dataset. However, the current framework should be interpreted as a local surrogate modeling methodology rather than as a universally generalizable cavitation prediction tool. Future work should focus on expanding the CFD database, incorporating learning curve assessment, exploring convolutional architectures and three-dimensional representations to improve model robustness and transferability.

Chapter 5

Data-Driven Prediction of Spray Macroscopic Characteristics for Marine Injectors using Neural Networks

This chapter is based on the author's third publication, published in Fuel, doi: 10.1016/j.fuel.2025.136736.

5.1 Introduction

The fuel flexibility embedded in the DFICE concept entails disadvantages related to the complexity of the injection system. Understanding the relationship between nozzle geometry, flow dynamics, and delivery performance provides additional critical insight on injector optimization and is a necessary step towards optimizing the spray trade-off characteristics for fuel flexible operation. Spray Tip Penetration (STP) is a critical element in the fuel injection process, as it directly influences air-fuel mixing, combustion efficiency, and, consequently, engine performance and emissions [118, 178]. Over the past few decades, researchers have been dedicated to developing mathematical models to predict STP and Spray Cone Angle (SCA). Such efforts have been intensified in recent years owing to the increasing sophistication of computational tools and the introduction of ML techniques.

The traditional methods for predicting STP and SCA often rely on empirical correlations, semi-Empirical models, and high-fidelity CFD simulations. Empirical correlations are frequently derived from experimental data and adjusted to fit certain operating ranges. They are user-friendly and computationally inexpensive. Conversely, their accuracy is limited when applied to conditions that diverge from those employed in their derivation. Semi-Empirical models, such as those derived by Wakuri et al. [269] and Hiroyasu et al. [97], combine simplified physics with empirical correlations. The incorporation of considerations such as momentum theory and jet disintegration theory enables these models to reflect more aspects of the underlying physics, going beyond empirical correlations. Nonetheless, they remain dependent on some empirical attributes and may lack precision in highly varying injection conditions [305].

CFD can be leveraged to model interactions between the liquid fuel jet, surrounding gas, and turbulence, providing comprehensive insights into spray breakup, atomization, and droplet dynamics [107]. However, numerical simulations can be computationally demanding and time-consuming, particularly for high-fidelity approaches [5]. Their precision is significantly influenced by the selected turbulence and break-up sub-models and necessitates validation against experimental data to ensure their reliability [182].

The data-driven modeling techniques, in particular ML, have demonstrated significant potential in accurately predicting the STP and SCA, while effectively capturing intricate interactions among input parameters such as injection pressure, nozzle shape, and fuel characteristics. It serves as an attractive alternative for performing the injection equipment design and optimization, in contrast to costly and time-intensive experimental measurements and CFD simulations [139].

Albeit the previous investigations, the semi-empical models as well as the ML restrict themselves to few designs during their formulation, most of them to one or two injector designs. In addition, those models present a limited number of geometrical parameters as input. Therefore, their use is very restricted during the pre-development phase of injector designs, making it difficult to take advantage of the fast prediction to explore the design range and identify the promising designs effectively during the optimization process. They focus more on the impact of different operation conditions or fuel types. Varying designs is inherently a more complex task than adapting to different operational conditions for a single, fixed geometry because of the dimensionality increment [49, 113]. Each design leading to more complex feature interactions and non-linear relationships, presenting a more challenging task.

Even though ML offers superior flexibility for spray macroscopic prediction compared to semi-empirical models, an elevated number of input parameters imposes an additional cost. The collinearity among geometric parameters can destabilize the model, and the data quantity is normally elevated to generalize effectively [301]. On the other hand, high-quality data acquisition can be expensive and time-consuming, introducing limitations to the data expansion [103, 116]. Setting up experiments or running simulations often requires significant resources. Another option is the usage of historical data and integrating it from different sources, but this task can be very demanding due to differences in data formats and structural inconsistencies [277]. Hence, balancing ML model complexity and generalization ability becomes a critical challenge.

Moreover, models in literature are more commonly developed for light-duty applications due to their dominance in the market. Heavy-duty marine injectors often operate over a much wider range of conditions than light-duty injectors, including variable fuel amounts, high injection pressures, and more severe environments [239]. Consequently, the accuracy of those models is reduced for this specific type of injector, making their extrapolation or tuning a time-consuming process without a guarantee of accurate results.

Therefore, the aim of this chapter is to obtain a tool tailored for marine Diesel injectors that permits reliable predictions of spray macroscopic characteristics (STP and SCA) as well as a relative comparison of different designs under operation conditions relevant for fuel flexibility: Diesel-only and DFICE mode. To this goal, a neural network has been conceived and trained with experimental data from a variety of marine designs and operation conditions. Finally, focusing on their applicability during the pre-development design phase, a total of 14 input parameters have been included in the model where most of them are related to geometrical constraints relevant to the conceptualization phase. To the best of the author's knowledge, this is the first predictive model that focuses on the injector design and includes 10 geometrical parameters as input features for predicting spray characteristics in marine Diesel injectors.

5.2 Experimental data acquisition

This study reviews the past decade of experimental testing, encompassing serial and prototype designs from WLO, to train the neural network. The resulting data acquired using optical methods is described in subsections 5.2.1 to 5.2.3, which offer a concise summary of the optical setup, image processing, and operational conditions for liquid-to-gas measurements.

5.2.1 Experimental configuration

The spray-propagation optical measurements were performed in a sealed cubic Constant Volume Chamber (CVC) with a total capacity of 34 liters. This CVC comprises three optical windows made of fused silica panes, each measuring 200 mm by 200 mm. The pressure and temperature were controlled via a valve-regulated nitrogen supply and cooling- water circulation, respectively. The chamber, designed to withstand pressures up to 60 bar, enabled optical diagnostics of spray behavior under controlled conditions, encompassing representative values of in-cylinder pressure during diesel injection. The chamber temperature was maintained constant at 293.15 K.

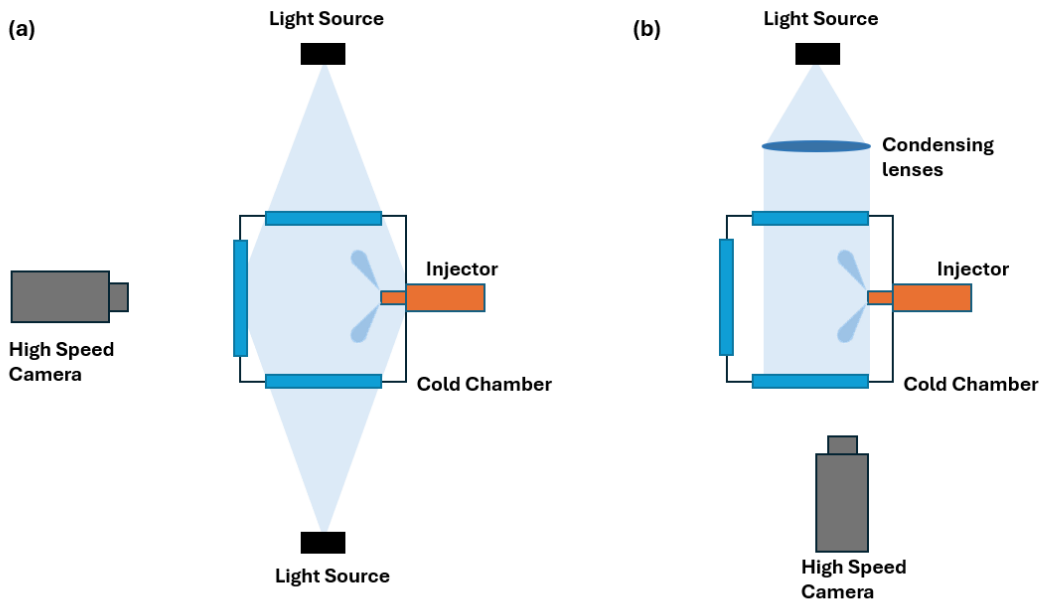

Figure 5.1: Schematic layout for the optical measurements at Woodward L'Orange: (a) Mie-scattering Light, (b) DBI.

Figure 5.1 depicts the schematic of the optical configuration employed for the visualization and quantification of the spray using Mie-scattering (Figure 5.1a) and

Diffuse-Backlight Illumination (DBI) (Figure 5.1b). The camera is positioned perpendicular to the light path and opposite to the injector for the Mie-scattering approach. In DBI, a collimated light beam illuminated the spray, and the resultant back-projections were recorded by the high-speed camera. The camera is a Photron FASTCAM SA5, capable of operating at frequencies up to 775,000 fps, while the injection process is controlled by a custom-engineered ECU system. The synchronization between the injection system and the camera guaranteed precise temporal resolution of the spray development, utilizing the injector trigger signal as a reference for capturing the image sequences.

This adaptable optical configuration facilitated thorough viewing and quantification of spray dynamics, yielding essential data for the validation of computational models and the optimization of injector designs for marine diesel engine applications. The combination of DBI and Mie-scattering enables the visualization of both macroscopic spray attributes and microscopic droplet characteristics.

5.2.2 Image processing method

An in-house software was developed to monitor the spray boundary across numerous frames, offering temporal data regarding the spray evolution. Following image processing, quantifiable data were extracted from the temporal variation of the spray. In general, the image processing is composed of three main stages: acquisition of the background image for comparison of the grey value of the pixels of each image, definition of the spray contour based on a threshold intensity-sensitive method [189] and calculation of the macroscopic variable. The two last stages are repeated for each time step until the end of injection.

Figure 5.2a illustrates an indicative processed image obtained by Mie-scattering. The intensity of the dispersed light correlates with the concentration of droplets. The threshold was selected on the pixel intensity difference based on the background value and empirically determined to differentiate between spray and gas areas. Based on this pixel comparison, the spray border is delineated according to the intensity of dispersed light. This technique enables the viewing and quantification of liquid phase penetration, particularly in dense sprays where DBI may be constrained by the spray's opacity.

In a similar manner, DBI is normally utilized to determine the area of the spray with adequate droplet concentration to be classified as part of the spray plume.

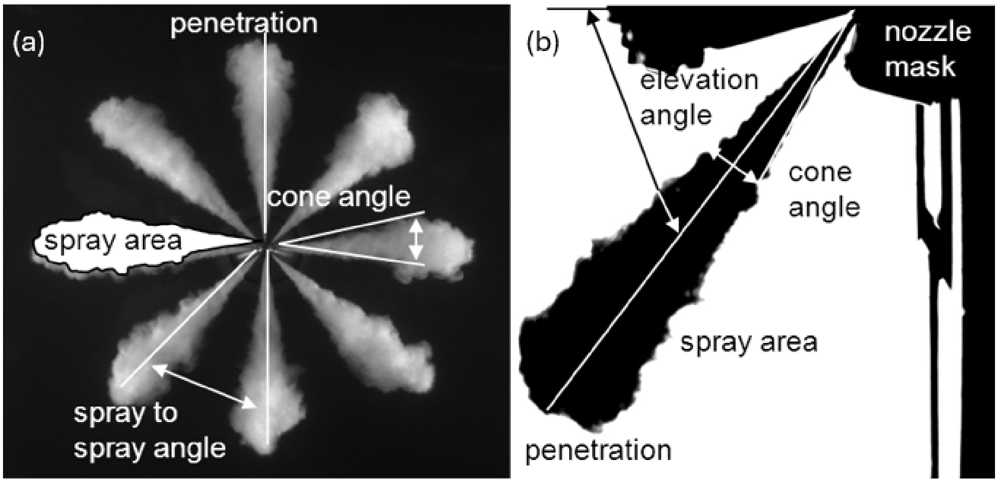

Figure 5.2: Indicative images: (a) Mie-scattering, (b) DBI.

Figure 5.2b illustrates an indicative processed image obtained by DBI. The spray image appears as a darker area contrasted against a lighter background. Image processing is utilized to augment contrast and delineate the spray boundary. Again, the threshold was selected based on the background value and empirically depicted to differentiate between the spray and gas areas. However, DBI cannot discriminate between the liquid core of the spray and the evaporating surrounding area.

These optical techniques are employed to determine STP, SCA, spray area, spray circumference, spray-to-spray deviation, and shot-to-shot deviation. The STP was defined as the furthest pixel from the spray hole exit. In this work, SCA was measured at the intersection of the spray axis and the center of mass based on the 2D representation image of the spray area. This strategy reduces the dependence on arbitrary thresholding or image segmentation choice [27]. Finally, the macroscopic spray variables of the multi-hole injectors are the average of each spray hole in the case of Mie-scattering measurement.

5.2.3 Operation conditions

The CVC facilitates the evaluation of diverse marine injectors, enabling a comparison of their spray characteristics and potential impact on combustion performance. For all cases, diesel fuel was substituted with a SRS Calibration Fluid CV during optical measurements. This fluid presents a very close viscosity tolerance and meets the ISO standard 4113-CV-AW. Calibration fluids are typically formulated to be less opaque than diesel, facilitating clearer viewing of the spray structure by optical techniques. Furthermore, they have well-defined and consistent physical properties, as shown in 5.1. In addition, Calibration Fluids exhibit lower flammability and toxicity compared to diesel and are more economical than specialized research-grade diesel fuels [142]. This substitution is essential to ensure consistency, reliability and results standardization of the testing.

Fuel Properties	SRS	Diesel
Density [kg/m^3]	824^a	$820 - 850^a$
Viscosity [mm^2/s]	2.52^b	$1.9 - 4.1^b$

Table 5.1: Fluid properties of the SRS Calibration Fluid CV in comparison to Diesel (^{a}value at 15°C; ^{b}value at 40°C) [221, 6].

In those measurements, the electronically triggered injectors exhibited an injection duration, excluding latency time, ranging from 220 μs to 1200 μs. A range of injection pressures, from 800 to 2200 bar, was investigated to distinguish the spray behavior throughout different operating regimes. The ambient pressure within the chamber was also altered. The temperature remained constant at 293.15 K due to the properties of this CVC, also referred to as a cold chamber, while the density was regulated by adjusting the pressure between 25 and 60 bar to simulate realistic engine conditions. Prior to each experiment, the chamber was purged and filled with nitrogen to a specified pressure and temperature, guaranteeing a uniform and inert atmosphere. Finally, each measurement was repeated between 5 to 10 times for each working condition to ensure reliability. Table 5.2 summarizes the injection conditions utilized in all experimental measurements.

Parameter	**Min.**	**Min.**
Injection Duration [μs]	220	1200
Injection Pressure [bar]	800	2200
Ambient Pressure [bar]	25	60
Temperature [K]	Constant at 293.15	
Repetitions [-]	5	10
Injector type [-]	27 multi-holes injectors from serial and prototype industrial designs	

Table 5.2: Operating conditions explored in the spray optical measurements.

5.3 Exploratory data analysis

In this study, the integration of historical data from numerous sources proved to be a time-consuming task. The experimental data from multiple projects were cross-referenced with the database of WLO's design department. During data standardization, the main issues encountered were insufficient data descriptions, improper formatting, duplicate entries, and outdated documentation. Consequently, the relevance of the datasets was considered in the data analysis.

Currently, data preparation problems are crucial in machine learning applications. Data collection and cleaning constitute near 80-90% of the total effort [277]. Once the data were curated, ensuring suitable format, size, and quality, 85 experimental measurements were selected, with each measurement varying between 11 and 90 data points based on the injection duration. Those measurements covered a total of 27 distinct injector designs, which include serial and prototype designs. The input features were selected based on feature reduction, profiling (assumptions derived from in-house expertise), and accessibility during the injector conceptualization phase. Consequently, the present formulation does not explicitly incorporate non-dimensional physical similarity groups such as Reynolds or Weber numbers. Although this feature representation facilitates integration into industrial design workflow, it may limit the direct physical interpretability of the learning relationships and may reduce extrapolation capability beyond the explored design space.

The final dataset had 14 input elements, including three operational conditions, ten design parameters, and the time after energization. The temporal reference adopted in this study corresponds to time after energization rather than hydraulic start-of-injection (SOI) due to the industrial collaboration. Consequently, the present formulation incorporates both electromechanical injector dynamics and fluid dynamic spray development. While this choice reflects the structure of the available industrial dataset, it may reduce transferability across injector architectures exhibiting different actuation delays.

The operational parameters are injection duration, injector rail pressure, and ambient pressure as already shown in Table 5.2 and delineate the injection conditions utilized during the experimental measures. The design parameters include sac hole volume, k-factor, number of spray holes, angle between spray holes, Q100, throttle effect, inlet spray hole diameter, outlet spray hole diameter, sac hole area, and minimum distance between spray holes. For reasons of confidentiality, the specific range of design parameters must be undisclosed because of cooperation with an industrial partner.

In addition, three of those features are the result of transforming data into relevant information and the minimum requirements in the early phase of the design process. The k-factor, or conicity, denotes the hole taper degree. The Q100 is the expected mass flow rate of the injector measured at a pressure differential of 100 bar. This number serves as a reference point throughout the injector design conceptual phase and offers a standardized assessment of diesel injector performance.

The throttle effect is the third one and is also a projected performance established at the conceptual phase. This dimensionless quantity is derived from the theoretical velocity according to Bernoulli's Equation and the anticipated mass flow rate as shown in Equation 5.1.

$$Throttle_{effect} = \frac{\frac{Q100}{n_{Holes}}}{A_o} \cdot \sqrt{\frac{\rho}{2\Delta P}} \tag{5.1}$$

where n_{Holes} is the number of spray holes, A_o represents the area of the spray hole, ρ signifies the fluid density, and ΔP indicates the pressure differential, which in this preliminary phase is 100 bar.

Particular attention should be drawn to the fact the some parameters are inherently interconnected because they arise from coupled injector design constrains. For example, outlet spray hole diameter, number of spray holes, sac volume and Q100 are partially co-dependent through hydraulic flow requirements. Consequently, the input features do not represent a fully orthogonal parameter space, and the DNN should be interpreted as learning coupled relationships rather than independent physical effects.

In complement, the redundancy among selected input features can be mathematically assessed by statistical correlation. Feature correlation is essential for the efficacy and interpretability of machine learning models. A reduced correlation among input characteristics could simplify the system equations in training algorithms, potentially facilitating resolution, enhancing convergence rates, and improving generalization [303]. Figure 5.3 illustrates the Kendall tau's rank correlation among the operation conditions and geometrical input features.

Kendall rank correlation is a non-parametric test that assesses the strength of dependence between two variables [199]. Kendall tau is a suitable option for correlation analysis in small datasets, in contrast to other formulations such as Spearman's correlation coefficient (rho) [62]. This method does not presuppose a linear relationship or normal distribution, providing narrower confidence intervals, better control over Type I errors, and robustness to outliers [199, 11]. Kendall tau's rank correlation can be mathematically defined as shown in Equation 5.2.

$$\tau = \frac{n_c - n_d}{n(n-1)/2} \tag{5.2}$$

where n_c reflects the number of concordant pairs, n_d represents the number of discordant pairs, and n signifies the sample size. This formulation results in a value such that $-1 \leq \tau \leq 1$. A coefficient of ± 1 signified a strong monotonic relationship, where a perfect positive correlation corresponds to the joint growth of both features. Conversely, an opposite directional growth is signified by a perfect negative correlation, while 0 indicates the absence of a monotonic relationship between the variables.

As illustrated in Figure 5.3, the majority of the characteristics exhibit weak to moderate correlations, with scores below ± 0.65. Among the operational conditions, only the ambient pressure exhibits strong correlations with certain design parameters, particularly with sac hole volume (0.90) and k-factor (-0.81). Nevertheless, this elevated correlation coefficient is misleading due to the diminished variability of the ambient pressure.

Regarding the design parameters, the k-factor also exhibits a high correlation with sac hole volume (-0.80). The sac hole volume also shows a high correlation with the angle between the spray holes (0.68) and Q100 (0.74). The correlation between the inlet spray hole diameter and the outlet spray hole diameter reaches a value of 0.74, which aligns with the expectations, as they are interconnected through the K-factor specification.

Features that are highly correlated might diminish model interpretability, elevate the danger of overfitting, and induce multicollinearity, complicating the assessment of each feature's individual impact on the target variable [154, 104]. Nonetheless, maintaining them can be advantageous, particularly in scenarios where feature interactions are complex, since eliminating correlated features may result in the loss of critical information [234]. Furthermore, their utilization is justified in contexts

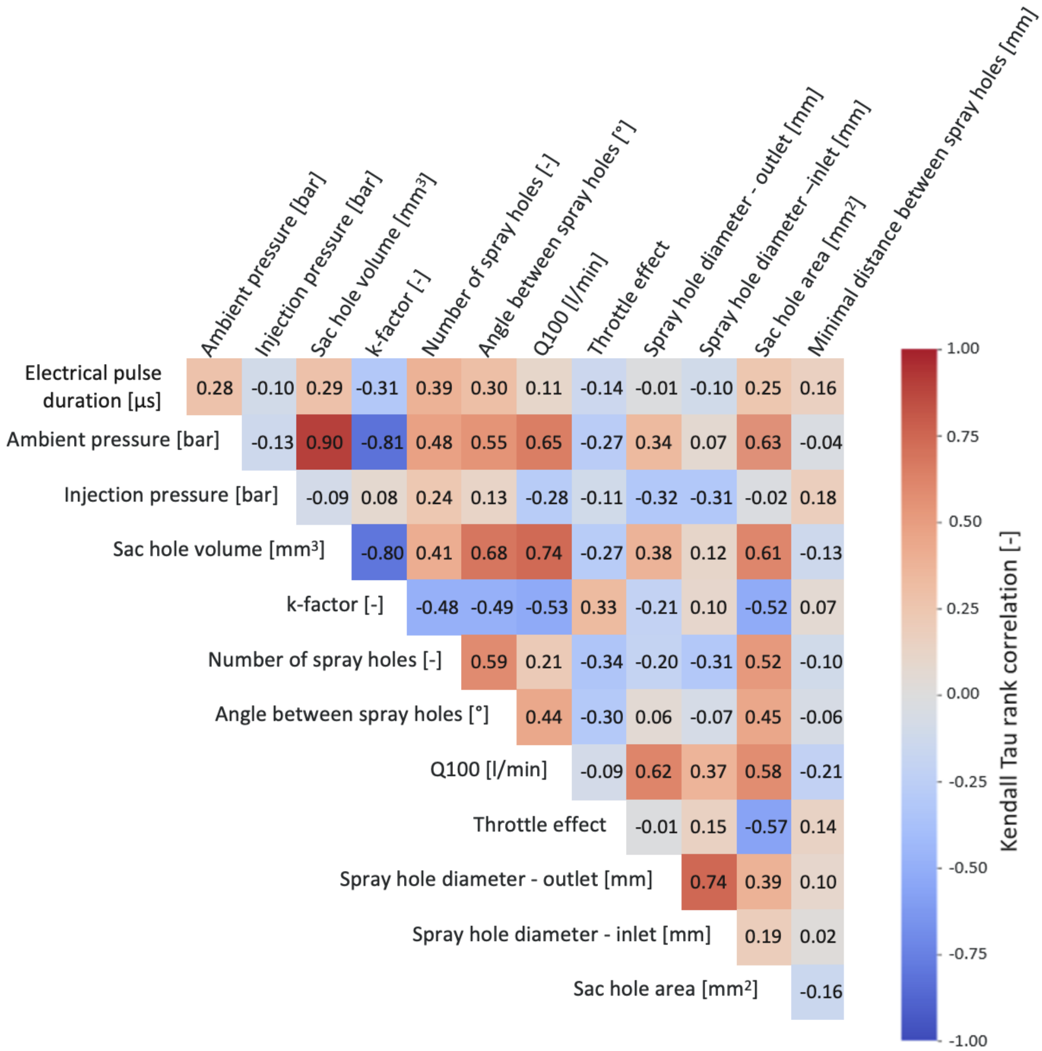

Figure 5.3: Kendall Tau's rank correlation coefficient for the selected features, operating conditions and geometrical parameters.

where they convey critical information and offer substantial insights into the model's interpretation and prediction [108]. Consequently, although certain features exhibited heightened correlation, the choice was made to preserve them owing to their importance in the design process, and derive a single surrogate model. While this reflects realistic engineering workflows, it limits the direct isolation of individual parameter effects.

5.4 Deep Neural Network Architecture

In this work a multilayer perceptron or fully connected, feedforward neural network was employed. The topological configuration of the DNN consists of an arrangement of neurons in a network of hierarchical layers (input, hidden and output layers) with a

14-x-2 architecture, where x represents the variable number of neurons in the hidden layer, while 14 and 2 correspond to the neurons of the input and output layers. The 14 input parameters that constitute the input layer were described in the preceding section. The objective of this DNN is to create a preliminary tool for the injector design process, correlating the geometrical parameters and operational conditions to spray penetration and cone angle. Consequently, the output layer comprises the intended predictions, i.e., spray penetration and spray cone angle.

In the development of the DNN architecture, the number of neurons and hidden layers were adjusted, with 15 hidden layers providing the optimal balance of accuracy and a complementary description is provided in Appendix C. Figure 5.4 shows the schematic structure of the DNN, where based on their connection, the outputs from the previous layer serve as composite features for each neuron in the subsequent layer.

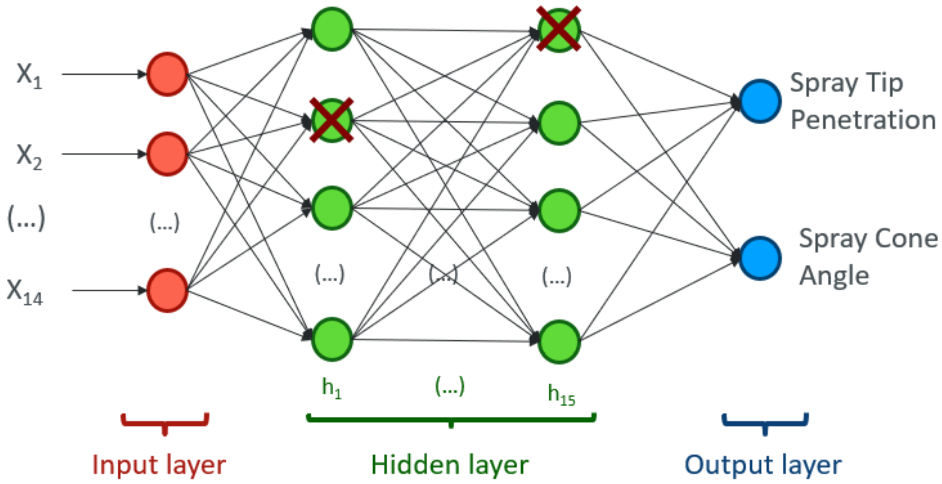

Figure 5.4: Representation of the neural network consisting of one input layer, ten hidden layers and one output layer, with dropout nodes symbolized by red marks.

The LeakyReLU activation function, a variation of the Rectified Linear Unit (ReLU), was utilized in every neuron within a layer to introduce non-linearity. Furthermore, two regularization techniques were employed to mitigate overfitting issues arising from the limited data available. The dropout rate was the first regularization technique employed, wherein nodes randomly cease to transmit their forward signal during training with a 30% probability, refer indicatively to the nodes annotated in the schematic DNN representation of Figure 5.4. The second regularization technique employed was early stopping. The model loss was calculated via Mean Absolute Percentage Error (MAPE).

In the DNN training, the 85 experimental cases were randomly split into two datasets: 80% for training and 20% for testing. The data division was executed with careful precision to guarantee that all penetration ranges (short, medium, and long) were represented in both data sets. The test set was entirely unexposed during the training phase, enabling an objective evaluation of network performance. Additionally, prior to training the DNN model, the input data were standardized to the range [0, 1], providing a uniform scale and appropriately representing the significance of each variable.

5.5 Results and discussion

5.5.1 Deep Neural Network evaluation

A comprehensive view of the training progress and performance of the neural network is illustrated in Figure 5.5. The loss function quantifies the difference between the predicted output of the neural network and the actual target values using MAPE. The downward trend seen with the increasing number of epochs, as depicted in Figure 5.5a, indicates effective error minimization between predictions and actual values for the training data, obtaining a MAPE of 1.67. The respective value for the test data is 2.63. Approximately 300 epochs into training, the model attains a plateau in its predictions, indicating that additional training does not substantially enhance its performance. The model executes 200 additional epochs owing to the patience definition, a hyperparameter employed in the early stopping technique.

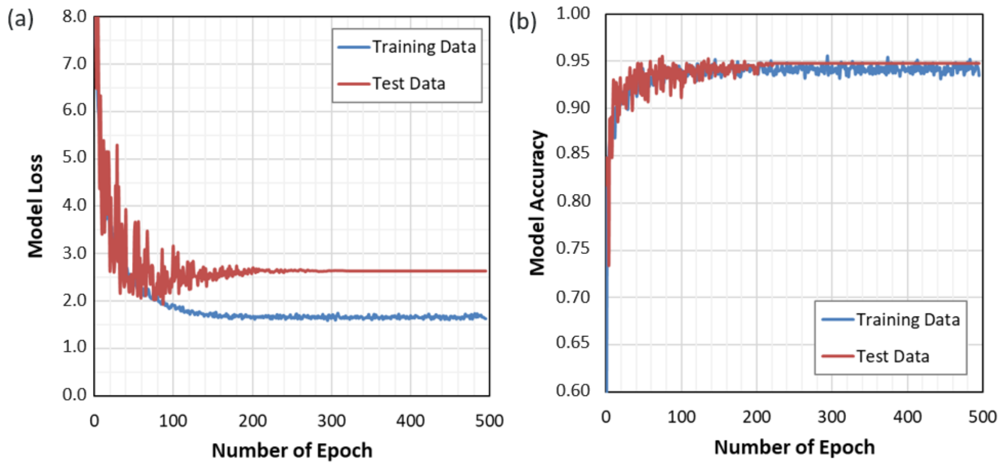

Figure 5.5: Training and test-data (a) loss curve of the DNN as a function of the number of Epochs, (b) accuracy curve of DNN as a function of the number of Epochs.

Early stopping terminates the training process when the loss no longer improves, while the patience value specifies the number of extra epochs to continue training following the last improvement in model loss [297]. Increased patience settings afford the model additional time to potentially enhance performance. In contrast, diminished patience values may cause premature stopping, leading to suboptimal model performance.

Furthermore, the model accuracy is illustrated in Figure 5.5b. The accuracy can be defined as the ratio of true predictions to the total number made by the model. At the beginning of training, accuracy usually increases rapidly as the model begins to learn the basic patterns within the data. Analogous to the loss curve, the accuracy curve likewise attains a plateau, indicating the maximal learning capability for the given data and architecture. The training data and test data exhibit comparable accuracies of 0.942 and 0.948, respectively.

The combination of an increase in accuracy and reduction of loss over time indicates the effectiveness of the DNN training process. The analogous pattern of loss and accuracy for both training and unseen data confirms the model's efficacy, demonstrating its ability to mitigate possible concerns, such as overfitting, a common problem for limited data sets. For instance, overfitting is typically marked by a persistent rise in training accuracy coupled with a plateau or rise in test loss [2]. Furthermore, both metric results corroborate the appropriate selection of hyperparameters, including the number of hidden neurons and learning rate, therefore confirming the correctness and reliability of model predictions.

In addition a linear regression between predicted and target values is depicted in Figure 5.6, quantifying how much of the variance in target variables is captured by the predictions. The regression plots demonstrate a good correlation between the output values and targets, with a Coefficient of Determination R^2 of 0.9845 for the training data and 0.9745 for the test data. The training predictions, shown by markers, essentially coincide with a diagonal line, exhibiting minor discrepancies during the initial phase of spray development (Figure 5.6a). The test predictions replicate the same behavior, with the inclusion of some overpredictions that account for the long spray penetrations and initial phase of the spray, as illustrated in Figure 5.6b. The early stages of spray measurement are characterized by significant flow disturbances and statistical uncertainty, resulting from the embedded complexities of spray formation, turbulence, and measuring difficulties. These factors influence the variability observed in spray characteristics and the quality of the model prediction.

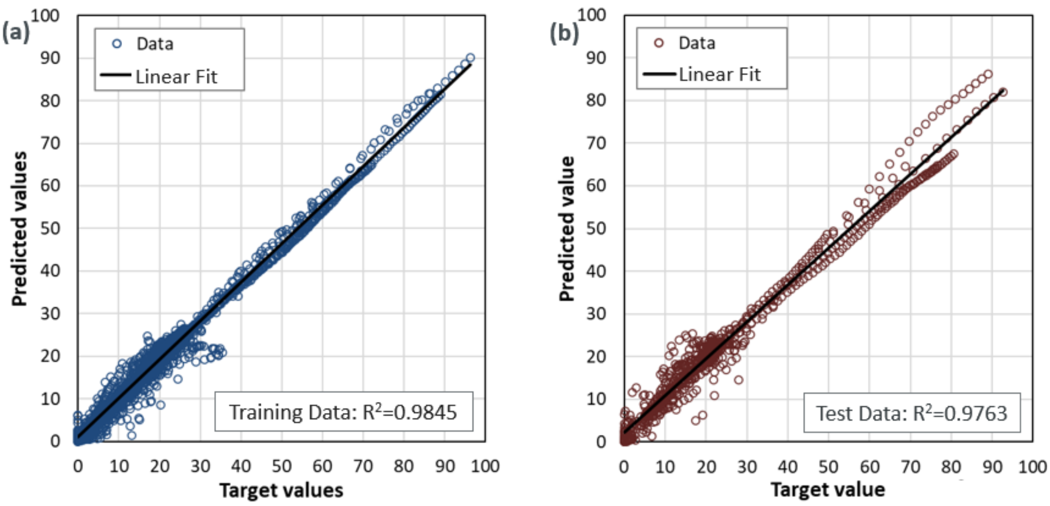

Figure 5.6: Linear regression of the DNN: (a) Training values (b) Test values.

Overall, these disparities can be considered minor across the entire dataset concerning the model's accuracy and reliability. Despite minor differences, the DNN consistently estimated the actual values, exhibiting a balance between fitting and predictive capabilities while avoiding overfitting.

5.5.2 Spray penetration and cone angle prediction

Figure 5.7, Figure 5.8, and Figure 5.9 illustrate the comparison between the observed STP and SCA and their corresponding predicted values generated by the DNN. The graphs exhibit STP and SCA as a function of time after energization, showcasing the versatility of the DNN to forecast the temporal evolution of the spray in three ranges: short, medium, and long penetration length. This range classification was imposed by the author due to the easy assimilation with the results. Besides, they also represent, respectively, a pilot injection for DFICE mode, part-load for Diesel-only mode and high-load for Diesel-only model. It is important to accentuate that pilot injection for DFICE mode is not only limited to a short penetration length. It is a combination of injection pressure and ambient pressure and is mostly driven by the short injection duration, often resulting in a short penetration length.

Experimental values are represented by markers and error bars, whereas the neural network forecasts are shown by only a solid line. The error bars were calculated via the standard deviation of the experiments. The DNN precisely captures the STP during short penetration, as illustrated in Figure 5.7a. Nevertheless, the model slightly overestimates the initial phase of the SCA (Figure 5.7b) and the fluctuation of the spray angle over time. This initial overestimation is a result of averaging 5 to 10 measurements at early injection stages, where low energization duration for the pilot injection in DFICE led to high variation in the injector opening time. After this initial phase, the model persistently exhibited an acceptable precision, however it was still insensitive to the oscillation of the SCA over time for operation conditions in the range of DFICE mode. The discrepancies pertain to the accuracy range, while the DNN effectively estimates the overall trend.

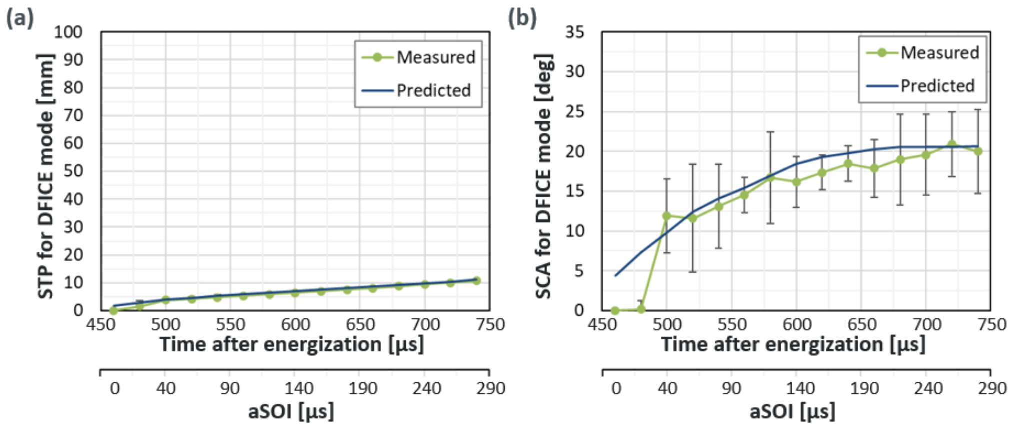

Figure 5.7: Comparison of the measured and predicted STP and SCA in function of time after start-of-injection (aSOI) for short penetration length, a representative test case of Diesel pilot injection for DFICE mode. The injector A was tested under an injection pressure of 800 bar, ambient pressure of 50 bar and injection duration of 360 μs.

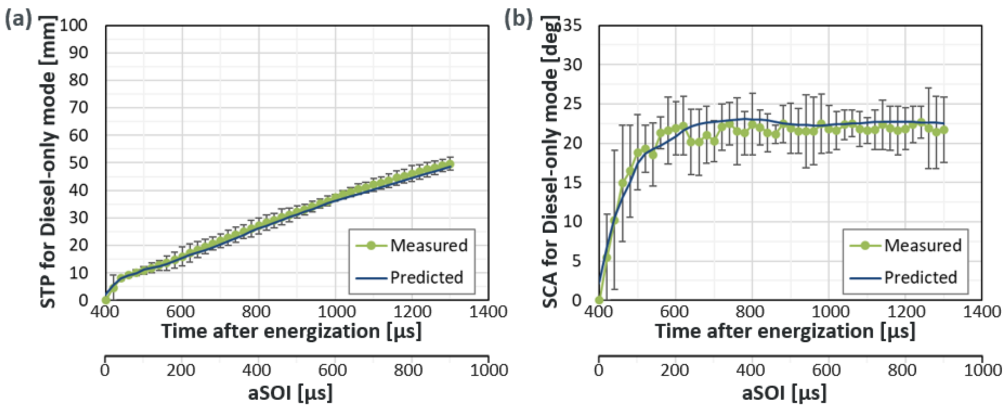

Figure 5.8: Comparison of the measured and predicted STP and SCA in function of time after start-of-injection (aSOI) for medium penetration length, a representative test case of part-load for Diesel-only mode. The injector B was tested under an injection pressure of 1000 bar, ambient pressure of 60 bar and injection duration of 500 μs.

A representative case of medium length or part-load for Diesel-only mode is depicted in Figure 5.8a. The spray length is accurately predicted, aligning with the experimental measurements. Furthermore, a considerable enhancement of the SCA estimation is evident in Figure 5.8b. With an early stabilization of the cone angle, the

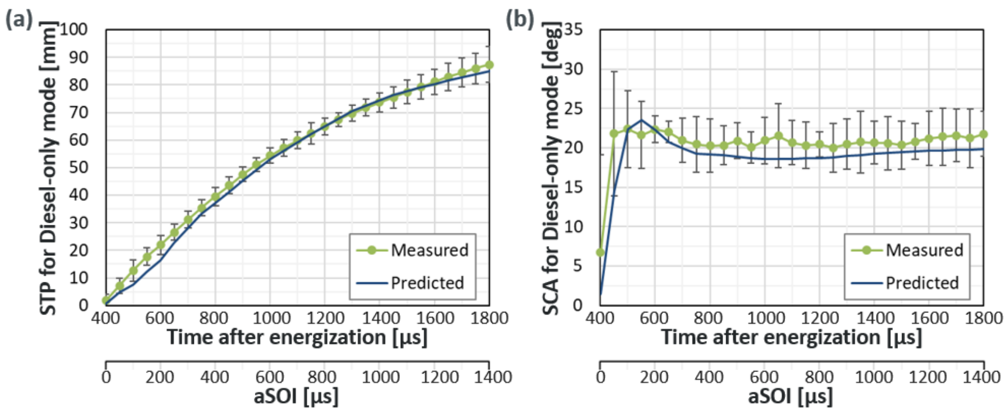

Figure 5.9: Comparison of the measured and predicted STP and SCA in function of time after start-of-injection (aSOI) for long penetration length, a representative test case of high-load for Diesel-only model. The injector C was tested under an injection pressure of 2000 bar, ambient pressure of 47 bar and injection duration of 947 μs.

DNN predicts this region more accurately. However, it still overlooks the dynamics of the cone angle, presenting only the overall trend. The last comparison illustrates a scenario of long spray length or high-load for Diesel-only mode, as shown in Figure 5.9. A consistent correlation between the experimental data and predictions for STP is demonstrated in Figure 5.9a. A marginal underestimation of SCA is noted across most of the time as shown in Figure 5.9b. Nonetheless, the general tendency is well addressed by predictions, respecting the measurement standard deviation.

Overall, the DNN successfully captures the temporal evolution of the spray, precisely reflecting the penetration dynamics during the observed time for the unseen data. An over-prediction of the SCA is noted during the initial phases of spray generation, especially in short spray lengths. This mismatch indicates that the DNN might be overestimating the initial momentum or underestimating the effects on factors like air resistance and droplet interactions during the early expansion phase, in complement to the increased statistical uncertainty to the early stages of spray measurement. Moreover, the DNN seems to only cover the average behavior of SCA. Notwithstanding these deviations, the DNN remains a valuable tool for comprehending and predicting SCA, presenting an attractive strategy to support the optimization of spray systems independent of the operation mode.

5.5.3 Analysis of the input features influence on the DNN and spray macroscopic characteristics

Figure 5.10 presents the feature importance analysis performed on the trained neural network, providing insights into the relative influence of the input features on the predicted values based on the experimental data set of this work. The graph depicts the normalized importance of each feature, ranked from most to least significant. Because the current model is formulated using dimensional engineering variables, the resulting feature importance rankings should be interpreted cautiously and not as direct indicators of fundamental physical dominance.

The injection pressure is a predominant factor among the operational conditions, with an importance of 0.22. As expected, the injection pressure affects the spray momentum and topology, including spray angle [240]. Elevated pressures can result in more transient sprays characterized by greater variability in spray morphology [228]. The injection duration has an intermediate importance of 0.04, since longer injection durations often result in enhanced STP lengths and a broader dispersion pattern.

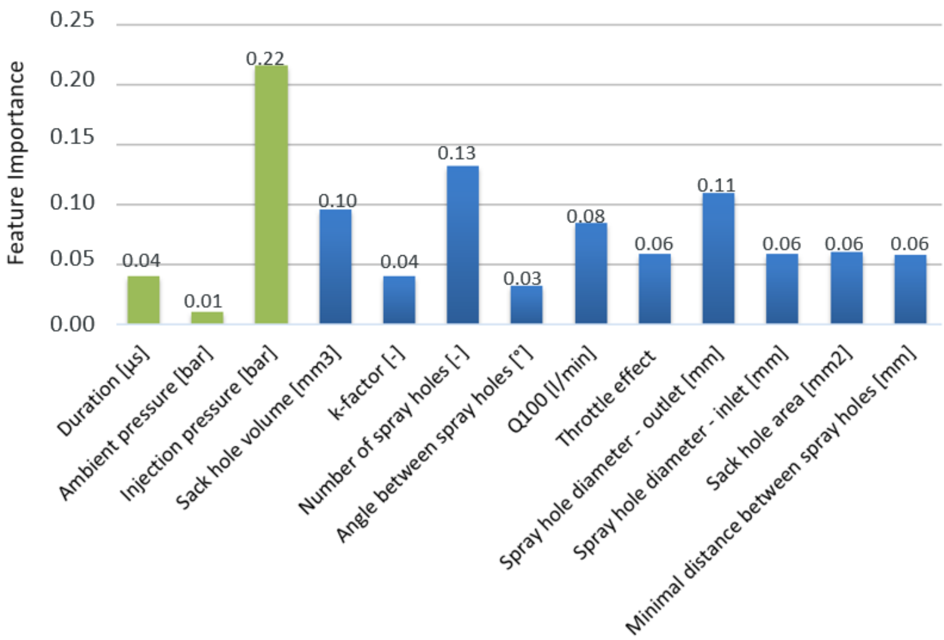

Figure 5.10: Feature importance analysis of the DNN input: green bars represent the operation conditions, while blue bars geometrical parameters

What stands out is the fact that the ambient pressure exhibits the least significance compared to other input features. The low statistical importance of the ambient pressure in the present DNN should not be interpreted as weak physical relevance. Instead, it primarily reflects the relatively narrow range of ambient pressure conditions represented in the training dataset. The experimental measurements were carried out over the last 10 years with similar CVC back pressures. As a consequence, the ambient pressure has low variety in the input set and therefore misleads the DNN to think it has a low relative importance. This analysis only displays the relative importance of each feature, therefore partially reflecting the complete physics behind the spray development.

Since the inclusion of geometrical parameters was one of the distinctiveness of this network, those features present a more balanced relative importance and high variability in the input set. Among the geometrical parameters, the number of spray holes, spray hole outlet diameter and sac hole volume are the predominant geometrical features affecting the learning behavior of the DNN, with respective importance of 0.13, 0.11, and 0.10. The spray hole outlet diameter is the primary geometrical parameter in most semi-empirical and ML models for spray characteristics due to its direct influence on momentum and initial droplet size [140].

Interestingly, Q100 demonstrates a relative relevance of 0.08, while the throttle effect, inlet spray hole diameter, sac hole area, and minimal distance between spray holes show equivalent importance of 0.06, indicating a complex interplay among these features. The K-factor and the angle between spray holes exhibit somewhat diminished significance, suggesting a relatively reduced impact within the examined data set range.

This hierarchical interpretation of feature importance underlines which input features most influence the DNN. This analysis assists on the interpretability and reliability of the ML model, often referred to as "black-box" because of their complex structure [79]. Besides, their interpretation is also a reflection of the training data set and their intricate interaction on the prediction. It can show the relative significance of an input parameter, information valuable for the injector design optimization process. However, the feature importance analysis cannot always be translated into mechanisms that govern spray behavior. Due to this limitation in terms of physical knowledge, PIML has been a growing subarea of ML, where physical laws are incorporated as model constraints or loss terms [287].

For example, PIML or constrained ML could further improve model robustness by embedding constrains directly into the learning process such as conservation laws or flow-capacity relations. Such methods may reduce the influence of dataset specific correlations and enhance extrapolation across injector families. Despite their advantages, the evaluation of high-order derivatives leads to performance loss and robustness issues rendering them, up to the present time, unfit for most real-world problems at engineering scales [242].

As a complement to better understanding the correlations between the variability of the geometrical design parameters and spray characteristics for fuel flexibility, eight training set cases from each range (short, medium and long penetration length) were selected, covering the main attributes of pilot injection in DFICE mode as well as part-load and high-load for Diesel-only mode. This qualitative comparison gives a perception of the geometrical parameters' interactions and a perspective to narrow the design range.

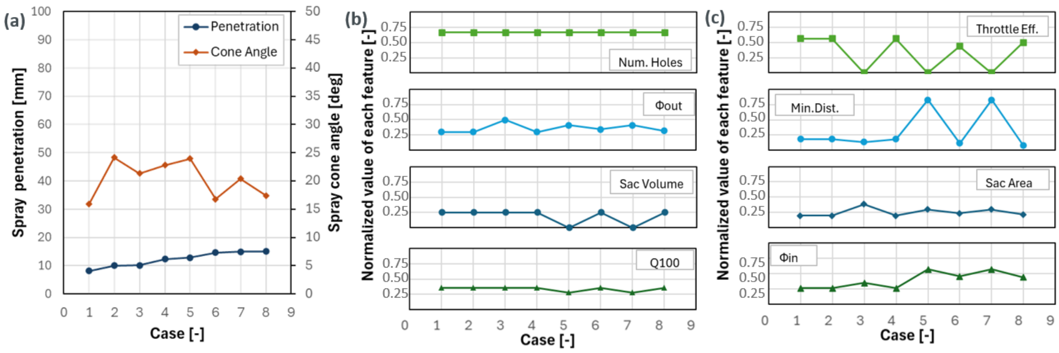

Figure 5.11: Eight selected cases at operation conditions representative of pilot injection in DFICE mode: (a) Spray characteristics per selected case; (b) normalized geometrical feature with higher importance; (c) normalized geometrical feature with 0.06 importance.

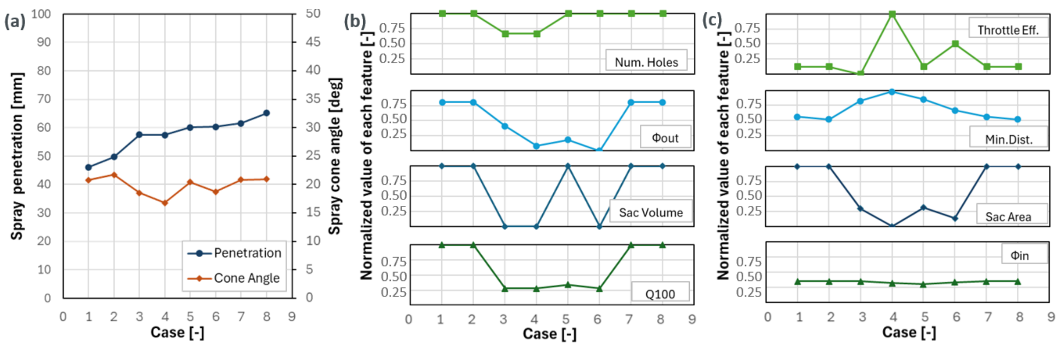

Figure 5.12: Eight selected cases at operation conditions representative of part-load for Diesel-only mode: (a) Spray characteristics per selected case; (b) normalized geometrical feature with higher importance; (c) normalized geometrical feature with 0.06 importance.

Figure 5.11, Figure 5.12 and Figure 5.13 illustrate the nominal STP and SCA of each category alongside the normalized geometrical parameters of the more relevant geometrical input feature. The geometrical parameters are normalized to facilitate direct comparison and preserve WLO proprietary information.

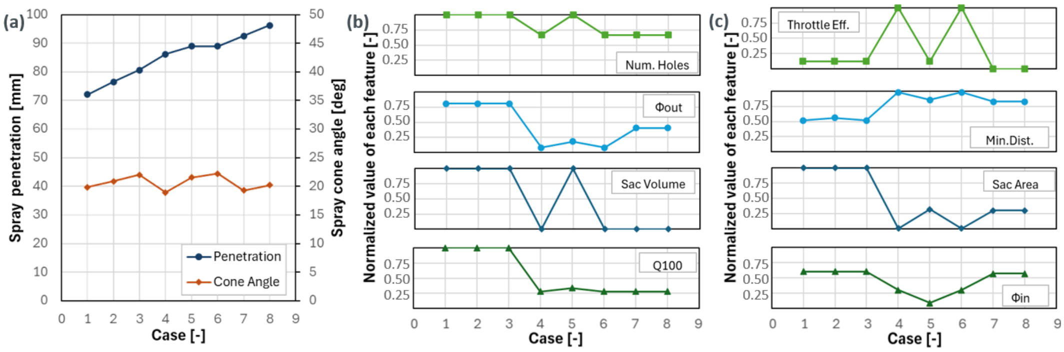

Figure 5.13: Eight selected cases at operation conditions representative of high-load for Diesel-only mode: (a) Spray characteristics per selected case; (b) normalized geometrical feature with higher importance; (c) normalized geometrical feature with 0.06 importance.

Figure 5.11 shows the representative cases of short spray length. The STP below 20 mm was artificially imposed to select those cases where the SCA fluctuates between 15 and 25 degrees, as displayed in Figure 5.11a. The normalized geometrical parameters that have higher to medium importance (greater than 0.07) are presented in Figure 5.11b, while those of medium importance (0.06) are depicted in Figure 5.11c. The number of spray holes, outlet spray hole diameter, sac hole volume, Q100, inlet spray hole diameter and sac hole area showed minimal variation. The throttle effect presented considerable variation, while the minimal distance between spray holes revealed more variability for penetrations over 12 mm. Consequently, when designing injectors for short penetration, most geometrical parameters may be specified within a narrower range, disregarding the operational conditions.

The medium spray length examples are depicted in Figure 5.12, where the STP ranging from 45 to 65 mm was the selected cut, with a corresponding SCA around 20 degrees. The number of spray holes, inlet spray hole diameter and minimal distance between spray holes are the sole characteristics with limited variability. When designing injectors targeting this spray characteristics range, those variables present limited design space, showing a pronounced design tendency. The other geometrical parameters, owing to considerable variability and unclear trends, may provide for broader conceptual flexibility when addressing this performance range.

Finally, the long penetration length is illustrated in Figure 5.13. For penetration ranges above 70 and 80 mm, all geometrical parameters remain at generally steady levels, indicating a strong design tendency. As penetration exceeds 80 mm, the number of spray holes, inlet spray hole diameter, Q100, minimal distance between spray holes and sac area oscillate within a limited range after an abrupt shift in tendency, underlining the need for careful consideration in their design space. Nevertheless, the sac hole volume, throttle effect, and inlet spray hole diameter may provide more conceptual versatility.

5.6 Conclusions from spray development characteristics

In this chapter, a DNN was implemented to predict the macroscopic characteristics of marine diesel injectors, focusing on the fuel flexibility during engine operation in both DFICE and Diesel-only modes. This model was designed as a support tool for the early injector design phase, incorporating a larger number of geometrical characteristics, with 10 design features integrated into the DNN formulation. In addition, the experimental measurements of 27 injector designs under various operational conditions were utilized to train the DNN, which resulted in a total of 85 experimental test cases. The combination of the three operation conditions as input features (injection pressure, ambient pressure and injection duration) covers the range of conditions relevant to fuel flexibility: pilot injection in DFICE mode, part-load and high-load for Diesel-only mode.

The large numbers of input features based on different injector designs bring distinctiveness to this neural network. At the same time, these distinguishing characteristics in combination with the limited experimental data set size have considerably increased the model complexity. The proposed DNN architecture and fine-tuning of the hyperparameters associated with the regularization techniques have ensured a responsive performance, mitigation of overfitting issues and effective generalization. The neural network exhibits strong predictive capabilities for STP and SCA independent of the operation mode, with an accuracy of 95% for the unseen data.

The feature importance analysis performed on the trained neural network offers an additional perspective of the main influences on the DNN for the predictions. This relative comparison does not directly translate into mechanisms that govern spray behavior. However, it underlines the learning behavior of the neural network and the characteristics of the training data set. In this perspective, the injection pressure (operation condition) holds the highest importance among all features. For the geometrical parameters, the number of spray holes and spray hole outlet diameter exhibit the most influence on the DNN. Additionally, certain geometrical parameters can potentially be categorized within a restricted or extensive range concerning design space and injector target performance.

Although the DNN demonstrated strong predictive capabilities within the explored design space, extrapolation outside the training range should be approached careful due to limited variability in some operation conditions and correlations among geometric features. Finally, the proposed DNN can support the marine injector design process due to the fast exploration of the design range in respect of geometrical constraints and identification of promising designs in the early phase more effectively in terms of STP and SCA. This gain in time would contribute to accelerating the optimization process, allowing to focus on fine-tuning and validating the design in the next stages of the development phase.

5.7 Critical review

This section critically evaluates the contributions of the present chapter within the context of established and emerging research on the application of ML techniques to predict spray macroscopic characteristics. Following the submission of the manuscript reporting the present results, no studies have been identified that employ ML models to predict spray characteristics directly from multiple injector geometrical parameters. Nevertheless, recent contributions by Zhang et al. [299, 300] have contributed to the growing body in the field of ML and spray characteristics. In the first study the predictions were done via ANN and the second one compared the predictive performance of the Response Surface Methodology with ANN for automotive applications. In both studies, the input features were the physicochemical properties of the fuel (five alcohol fuels and gasoline) and operation conditions, which were measured experimentally for the same multi-hole injector. The models presented an accuracy above 98% to predict spray characteristics such as STP, SCA, spray area and evaporation index. These studies may provide more insights into the development of fuel injection systems for alcohol-fueled engines.

In this context, this chapter address an important engineering challenge in marine propulsion system: balancing fuel flexibility, injector design complexity and jet development [32][276]. One of the major strengths of this chapter lies in its industrial relevance. Unlike many previous ML studies focused on simplified single-hole injectors [179][101][141][301], this work employs data from 27 industrial multi-hole marine injector designs collected over approximately a decade. This broader design scope significantly enhances the practical applicability of the work. In particularly for marine engine applications where operational conditions are highly variable. The inclusion of ten geometrical parameters in addition to operational conditions is another noteworthy contribution, as many earlier studies considered only limited geometric features. By incorporating this broader set of design parameters, the proposed approach seeks to reduce resilience on resource intensive experimental campaigns, semi-empirical correlations and CFD simulations. Consequently, the work moves beyond proof-of-concept ML applications and attempts to integrate ML assisted prediction directly into the injector pre-development workflow.

Furthermore, this chapter demonstrates a clear effort to address overfitting through the use of dropout regularization and early stopping techniques. Those strategies are especially important given the limited size of the available dataset size. The reported prediction accuracy of approximately 95% for unseen test data suggest that the DNN successfully captures the dominant relationships between injector geometry, operating conditions and spray behavior.

Despite these strengths, this chapter exhibits methodological limitations that reduce the physical interpretability and generalizability of the proposed model. One important issue concerns the temporal reference adopted for the spray evolution. The use of time after energization introduces a coupling between electromechanical injector dynamics and fluid dynamics spray development. Since injector actuation delay can vary significantly across injector architectures and operating conditions, the resulting model may not transfer reliably to injectors with different hydraulic response characteristics. Consequently, the DNN partially learns system-level actuation behavior rather than purely spray physics phenomena.

Another limitation concerns the insufficient variability of certain operational parameters. The ambient pressure range explored in the experiments is relatively narrow due to the standard testing workflow at WLO. This limited variability leads the feature importance analysis to suggest that back pressure has little influence on spray behavior. However, this result contradicts established spray physics, in which ambient density strongly affects jet breakup, penetration and atomization process [21]. This issue highlights a broader limitation of data-driven models: feature importance metrics are inherently local and these scores often reflect statistical variability present within the dataset and model usage of individual features rather than universal physical relevance of the underlying variables [211].

Besides, the DNN presents interdependence among input features and some geometrical variables are inherently coupled through injector hydraulic constraints and engineering design practices. Although the Kendall's tau correlation is presented, the work kept coupled relationships. This methodological choice reflects a more realistic engineering workflow rather than the use of non-dimensional physical similarity groups such as Reynolds number, cavitation number or momentum-flux ratio. On the one hand, this facilitates usability and the integration into engineering workflow. On the other hand, it introduces hidden correlations into the model. The incorporation of non-dimensional groups may enhance physical interpretability and generalization capabilities beyond the current design space and should be taken into consideration for future work.

The analysis could have been further strengthened through the adoption of a more structured experimental design or conditional sampling. Such strategies would facilitate the incorporation of non-dimensional scaling parameters or physical informed models and may enable a clearer separation of the effects associated with individual inputs. However, these potential benefits must be balanced against practical considerations and the integration of surrogate models into routine engineering workflows. Additionally, the reproducibility of this work is restricted due to the confidentiality requirements associated with the industrial collaboration. The ranges of the geometrical parameters are not disclosed and the experimental dataset are not publicly available. While such confidentiality constraints are understandable in the context of industrial collaborations, they inevitably reduce the scientific transparency of the study.

Overall, this chapter represents a valuable contribution to the application of ML in marine injector design. It is particularly relevant from an engineering design perspective because it enables rapid exploration of injector design space during early-stage development. However, the proposed surrogate model remains limited in points related to physical interpretability, interdependent feature selection and restricted parameter variability. Future work should consider the adoption of conditional sampling, physically normalized features and physics-informed ML, which could significantly strengthen the robustness and scientific impact of the methodology.

Chapter 6

Conclusions and recommendations for future work

6.1 Conclusions

In this thesis, the main objective was to develop predictive and efficient numeric models with reduced computational cost to support the design phase of marine Diesel injectors. Those models took detailed geometric parameters into consideration and addressed constraints imposed for fuel flexibility configuration to support early-stage design decisions.

To this goal, the current work incorporated NIST REFPROP and PC-SAFT EoS calculations for the thermodynamic closure, enhancing the CFD model with affortable computational cost due to the tabulation approach. The proposed model has been applied to explore the potential of needle tip shape modifications on in-nozzle flow characteristics for fuel flexibility in marine injectors. Besides, the proposed CFD model has been employed to develop a CFD-assisted ML surrogate model. This second model is able to predict the cavitation morphology of different marine injectors in terms of scalar values and visual distributions. Finally, a third model has been elaborated to predict the spray macroscopic characteristics based on ten geometric parameters and three operation conditions. The development of those models took into consideration their applicability in the early design phase.

The conclusions for each chapter of this thesis are summarized as follows:

In **Chapter 1**, the background and motivation for this study are discussed. Then, a bibliographic study and discussions are carried out on different topics, from understanding the nozzle geometrical parameters influence to the phase change modeling in fuel injectors to machine learning application in fluid dynamics and spray macroscopic characteristics predictions.

In **Chapter 2**, the governing equations along with the employed assumptions are introduced for the CFD model. The turbulent viscosity corrections for the $k - \omega$ model were also discussed, followed by the inclusion of NIST REFPROP and PC-SAFT EoS fluid properties calculations in the thermodynamic closure. Then, the machine learning workflow has been detailed, addressing the requirements for reliable data preparation and discussing model architecture to prevent overfitting.

In **Chapter 3**, the CFD model enhancement is first validated based on the ECN Spray C data, a light-duty, small scale and single hole injector. The phase changes was satisfactorily predicted by the CFD model. Then, the impact of needle tip design on internal flow and cavitation in marine Diesel injectors is discussed, evaluating a base industrial design against three proposed alternatives (NV-01, NV-02 and NV-03). Indeed, the goal here is to apply the CFD model modifications on marine injector designs (large scale, heavy-duty and multi-holes) and to better understand the phase change in both operational models: dual-fuel and Diesel-only. Therefore, the redesign of the needle tip was selected for its simplicity and cost-effectiveness in comparison to other modifications in the injector design. Finally, the NV-01 has offered the best trade-off in terms of flow assessment focusing on the fuel flexibility for marine applications.

In **Chapter 4**, the enhanced CFD model is employed to generate datasets and train computationally efficient ML surrogate models, combining the CFD simulation and neural networks for a reliable assessment of cavitation of different marine injector designs. The LHS sampling has ensured a good sample distribution across all dimensions of the input space and minimized the computational cost of generating data from CFD simulations. Then, this data has been used to train three neural networks: two DNNs and one GM. The first DNN predicts flow coefficients (C_d and C_v) with high accuracy. The vapor volume predictions suffer from under-representation due to the absolute low data values. This has been impacting the overall accuracy of the model, reaching only 67%. In addition, the second DNN and GM predict the cavitation morphology via contour plots of vapor volume fraction.

The strategic data pre-processing and model architecture mitigated any intrinsic structural issues due to the dimensional mismatch. Predicting images from scalar values exponentially increases the model complexity, especially when the data is limited. The image depth reduction from 24 bits to 8 bits has been proven to be crucial to alleviate the dimensionality issues. Both models have been capable of forecasting the cavitation location. However, the GM oversimplifies the gradient variations. The further reduction of pixels on the output image is the leading reason for the DNN's precise predictions of the intensity of the vapor volume fraction. Finally, this chapter has demonstrated the importance of data preparation methods (feature engineering) and knowledge of the neural network requirements in complement to the domain expertise for a successful implementation of a joint workflow to predict cavitation in the early design phase.

In **Chapter 5**, a DNN is proposed to predict the macroscopic characteristics of marine Diesel injectors. Data preparation and feature engineering have been fundamental to ensure quality and consistency of the experimental data. The pre-processing has also contributed to ensuring good generalization independent of possible issues with high-dimensional feature space and a small dataset. This model has included ten design parameters and three operation conditions as input features. In the literature, a high number of input features have been avoided due to exponentially increasing the model complexity and the resulting difficulty to learn meaningful patterns. The DNN exhibits strong predictive capabilities for spray penetration and cone angle, with an overall accuracy of 95% for the unseen data. Finally, this chapter closes with a feature importance analysis of the input parameters, categorizing them within a restricted or extensive range concerning the design space and injector target performance.

In summary, the models developed in this work can contribute to narrowing the gap between scientific solutions and industrial applications. Their conception has taken into consideration the design phases and engineers' usability. Moreover, the possibility of predicting fast and accurate cavitation and macroscopic spray characteristics in the early design phase can contribute to shorter development cycles and better decision-making in the early design phases.

6.2 Future work

Based on the research presented, the suggested future work can be summarized as follows:

- **Expansion of the numbers of input features for the neural networks predicting images from scalar variables.** Increasing the number of input features provides a more comprehensive representation of the underlying system, thereby reducing ambiguity in the image generation process. However, a larger feature space typically necessitates an increase in dataset size to support a effective model training. Therefore a learning curve analysis should be included in the sensitivity study to assess the influence of dataset size on predictive performance.

- **Alignment of the input features of all neural networks proposed in this work, from the prediction of the cavitation morphology to the prediction of the spray macroscopic characteristics.** This alignment would produce a complete and robust tool for the early phases of marine injector design. This integration would provide a comprehensive overview of the synergistic or antagonistic effects of different parameters on spray and cavitation behavior. This would also allow engineers to quickly explore a wide range of design options and operating conditions without having to run computationally expensive simulations or conduct time-consuming experiments for each case.

- **Integration of non-dimensional groups for improved model interpretability and transferability** The possibility of reformulating the feature space using physical non-dimensional groups should be investigated to improve interpretability of the learning relationships. Such a parametrization may enhance physical consistence, facilitate transferability across injector geometries and operation conditions and reduce feature interdependence. However, this approach may compromise model usability and integration into industrial workflows. Furthermore, the incorporation of non-dimensional groups may require conditional sampling strategies to ensure adequate coverage of the resulting parameter space.

- **Expansion of the PC-SAFT tabulation for all working fluids (n-**

dodecane liquid, n-dodecane vapor and nitrogen) in a commercial software. This ternary system for the fluid properties would exclude the vapor liquid equilibrium calculation from the CFD solver and eliminate the requirement of additional models to cover the phase change (e.g. Zwart-Gerber-Belamri). Besides, the reliance on tuning values for the phase change modeling could be minimized or even completely eliminated.

Appendix A

Flow characterization - Non dimensional numbers

Some flow characteristics could be associated in dimensionless quantities. Based on the pressure difference between the inlet and the outlet of the nozzle hole, the Bernoulli's Equation A.1 can be applied to derive the Theoretical velocity (u_{th}) Equation A.2, assuming a negligible inlet velocity:

$$P_i = P_b + \frac{1}{2}\ \rho_l u_{th}^2 \tag{A.1}$$

$$u_{th} = \sqrt{\frac{2\Delta P}{\rho_l}} \tag{A.2}$$

where the inlet pressure is P$_i$, the outlet pressure is P$_b$ and ρ_l is the liquid density

A differentiation needs to be made regarding the cavitating flows. For non cavitating flow the velocity profile at the nozzle exit can be assumed as uniform across the outlet area. In contrast, the same assumption cannot be applied for cavitating flows. It is necessary to neglect the vapor section in order to estimate an effective outlet velocity u_{eff} and effective area A_{eff}. Figure A.1 show the simplifications of velocity profiles.

Once defined effective outlet velocity and effective area under cavitation condition, the mass flux and its integral form at the outlet section of the nozzle hole can be obtained as:

$$\dot{m}_f = \int_{A_o} u\rho\ dA \tag{A.3}$$

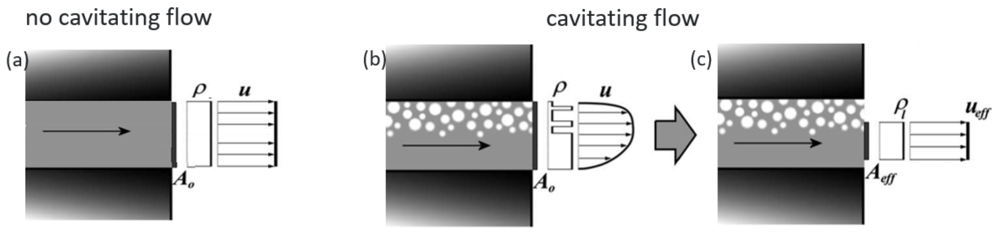

Figure A.1: Simplification of the outlet velocity profile for (a) no cavitating flow; (b) and(c) for cavitating flow (adapt from [186])

$$\dot{m}_f = \rho u_{eff} A_{eff} \tag{A.4}$$

Analog to the mass flux, the moment flux can be mathematically defined as:

$$\dot{M}_f = \int\limits_{A_o} u^2 \rho \, dA \tag{A.5}$$

$$\dot{M}_f = \rho u_{eff}^2 A_{eff} \tag{A.6}$$

Based on the previous equations, other non-dimensional parameters can be derived to characterize the flow. The ratio between mass flow by the theoretical mass flow defines the discharge coefficient C_d:

$$C_d = \frac{\dot{m}_f}{A_o \rho_l u_{th}} = \frac{\dot{m}_f}{A_o \sqrt{2\rho_l \Delta P}} \tag{A.7}$$

The discharge coefficient can be also obtained analysing the loss impost on the flow as:

$$C_d = C_v C_a \tag{A.8}$$

Where C_v is the velocity coefficient, and C_a is the area coefficient. As the name implies, C_v takes into consideration the velocity loss, and C_a include the loss due to reduction in the effective flow cross-section. Those non-dimensional parameters can be derived as:

$$C_v = \frac{u_{eff}}{u_{th}} \tag{A.9}$$

$$C_a = \frac{A_{eff}}{A_o} = \frac{D_{eff}^2}{D_o^2} \tag{A.10}$$

$$A_c = C_c A \tag{A.11}$$

Finally, Reynolds number and cavitation number are fundamental dimensionless parameters used to characterized nozzle internal flow. The Reynolds number characterizes the ratio between inertial and viscous forces acting on the flow and provides an indication of the flow regime inside the nozzle. It is defined as:

$$Re = \frac{\rho_l u_{eff} D_o}{\mu_l} \tag{A.12}$$

where D_o is the nozzle outlet diameter and μ_l is the dynamic viscosity of the liquid. Larger Re indicates that inertial forces dominates over viscous forces, leading to turbulent flow conditions typically encountered in fuel injector nozzles.

The cavitation number is used to characterize the propensity of the flow to cavitate within the nozzle. It relates the available pressure difference driving the flow to the liquid vapor pressure and is defined as:

$$\sigma = \frac{P - P_v}{\frac{1}{2}\rho V^2} \tag{A.13}$$

where P_v is the vapor pressure of the liquid and V is the characteristic flow velocity. Lower values of σ correspond to conditions with a higher tendency for cavitation development, where larger values indicates non-cavitating flow conditions.

Appendix B

Latin-Hypercube Sampling

The cases 59 sampled via the Latin-Hypercube Sampling and evaluated in this work are detailed in Table B.1. The cases 3, 7, 9, 13, 15, 22, 27, 36, 40, 43 and 47 are used as test data set, which are completely unknown to the neural networks.

Case [-]	Needle Lift [μm]	Conicity [-]	Needle Tip [-]		Case [-]	Needle Lift [μm]	Conicity [-]	Needle Tip [-]
1	383	0	BD		31	147	2	NV-01
2	476	0	BD		32	183	2	NV-01
3	68	1	BD		33	218	2	NV-01
4	226	1	BD		34	362	2	NV-01
5	276	1	BD		35	390	2	NV-01
6	340	1	BD		36	125	3	NV-01
7	104	2	BD		37	140	3	NV-01
8	132	2	BD		38	154	3	NV-01
9	355	2	BD		39	412	3	NV-01
10	369	2	BD		40	190	4	NV-01
11	405	2	BD		41	290	0	NV-02
12	75	3	BD		42	197	1	NV-02
13	376	3	BD		43	269	1	NV-02
14	419	3	BD		44	448	1	NV-02
15	433	3	BD		45	89	2	NV-02
16	441	3	BD		46	61	3	NV-02
17	204	4	BD		47	312	3	NV-02
18	297	4	BD		48	233	4	NV-02
19	304	4	BD		49	326	4	NV-02
20	319	4	BD		50	469	4	NV-02
21	111	0	NV-01		51	54	0	NV-03
22	240	0	NV-01		52	161	1	NV-03
23	283	0	NV-01		53	168	2	NV-03
24	426	0	NV-01		54	254	2	NV-03
25	82	1	NV-01		55	398	2	NV-03
26	118	1	NV-01		56	462	2	NV-03
27	211	1	NV-01		57	175	3	NV-03
28	247	1	NV-01		58	261	3	NV-03
29	333	1	NV-01		59	347	3	NV-03
30	455	1	NV-01					

Table B.1: The 59 cases evaluated in this study defined in terms of the Needle lift, Conicity and Needle tip.

Appendix C

Neural Networks

The tables bellow provide a description of the neural network developed in this work.

Parameter	DNN chapter 4
Model Type	Sequential
Input layer	3 neurons
Hidden layer	6 layer with 100 neurons each and bias activated in each
Activation function (for all layers)	LeakyReLu (alpha 0.3)
Kernel initializer (for all layers)	he_normal
Output layer	3 neurons
Early stopping	After 200 epochs
Dropout	Hidden layer 3 droprate 0.2
Learning rate	$0.00005 * 0.9^{(epoch/60)}$
Loss function	Mean Absolute Percentage Error

Table C.1: Parameters of the DNN to predict the volume vapor, C_d and C_v in Chapter 4.

Parameter	DNN Chapter 4
Model Type	Sequential
Input layer	3 neurons
Hidden layer	12 hidden layer with 1000 neurons each and bias activated in each
Activation function (for all layers)	LeakyReLu (alpha 0.3)
Kernel initializer (for all layers)	he_normal
Output layer	27556 neurons e.g. pixel
Early stopping	After 500 epochs
Dropout	Hidden layer 8&10 droprate 0.2
Learning rate	$0.005 * 0.5^{(epoch/25)}$
Loss function	Mean Squared Error

Table C.2: Parameters of the DNN to predict cavitation images in Chapter 4.

Parameter	GM Chapter 4
Model Type	Decoder
Input layer	neurons
Hidden layer	1 hidden layer with 5016 neurons and 3 convolutional 2DTranspose layer (16,8,1) and bias deactivated in each
Activation function (for all layers)	LeakyReLu (alpha 0.3)
Kernel initializer (for all layers)	he_normal
Output layer	265x306 pixel
Early stopping	After 200 epochs
Dropout	Every hidden layer droprate 0.2
Learning rate	$0.005 * 0.5^{(epoch/125)}$
Loss function	Mean Absolute Percentage Error

Table C.3: Parameters of the GM to predict cavitation images in Chapter 4.

Parameter	DNN Chapter 5
Model Type	Sequential
Input layer	14 neurons
Hidden layer	15 layer with 70 neurons each and bias activated in each
Activation function (for all layers)	LeakyReLu (alpha 0.3)
Kernel initializer (for all layers)	he_normal
Output layer	2 neurons
Early stopping	After 200 epochs
Dropout	Hidden layer 1 droprate 0.3
Learning rate	$0.015 * 0.0005^{(epoch/200)}$
Loss function	Mean Absolute Percentage Error

Table C.4: Parameters of the DNN to predict the STP and SCA in Chapter 5.

Bibliography

[1] Experimentally validated dns and les approaches for fuel injection, mixing and combustion of dual-fuel engines, August 2021. [online] https://edem-itn.eu/.

[2] E. Abad-Rocamora, F. Liu, G. G. Chrysos, P. Olmos, and V. Cevher. Efficient local linearity regularization to overcome catastrophic overfitting. *ArXiv*, abs/2401.11618, 2024.

[3] B. Abderrezzak and Y. Huang. Investigation of the effect of cavitation in nozzles with different length to diameter ratios on atomization of a liquid jet. *Journal of Thermal Science and Engineering Applications*, 9, 04 2017.

[4] M. Adil, R. Ullah, S. Noor, and N. Gohar. Effect of number of neurons and layers in an artificial neural network for generalized concrete mix design. *Neural Computing and Applications*, 34:8355 – 8363, 2020.

[5] A. Afzal, Z. Ansari, A. R. Faizabadi, and M. Ramis. Parallelization strategies for computational fluid dynamics software: State of the art review. *Archives of Computational Methods in Engineering*, 24:337 – 363, 2016.

[6] A. Amin, A. Gadallah, A. El Morsi, N. El-Ibiari, and G. El-Diwani. Experimental and empirical study of diesel and castor biodiesel blending effect, on kinematic viscosity, density and calorific value. *Egyptian Journal of Petroleum*, 25(4):509–514, 2016.

[7] A. Andriotis, M. Gavaises, and C. Arcoumanis. Vortex flow and cavitation in diesel injector nozzles. *Journal of Fluid Mechanics*, 610:195 – 215, 09 2008.

[8] Anon. Senate regulation 25: Physical format, binding and retention of theses. **url**: www.city.ac.uk/about/city-information/governance/constitution/senate-regulations, 2015.

[9] ANSYS, Inc. *Ansys Fluent Theory Guide*. ANSYS, Inc., Canonsburg, PA, USA, 2021 r1 edition, 2021.

[10] M. Apolonia, R. Fofack-Garcia, D. R. Noble, J. Hodges, and F. X. Correia da Fonseca. Legal and political barriers and enablers to the deployment of marine renewable energy. *Energies*, 14(16), 2021.

[11] S. Arndt, C. Turvey, and N. C. Andreasen. Correlating and predicting psychiatric symptom ratings: Spearmans r versus kendalls tau correlation. *Journal of Psychiatric Research*, 33(2):97–104, 1999.

[12] J. Arrègle, J. V. Pastor, and S. Ruiz. The influence of injection parameters on diesel spray characteristics. *SAE Technical Paper*, 3 1999.

[13] J. A. Badra, F. Khaled, M. Tang, Y. Pei, J. Kodavasal, P. Pal, O. Owoyele, C. Fuetterer, B. Mattia, and F. Aamir. Engine Combustion System Optimization Using Computational Fluid Dynamics and Machine Learning: A Methodological Approach. *Journal of Energy Resources Technology*, 143(2), 08 2020.

[14] R. Balz, I. G. Nagy, G. Weisser, and D. Sedarsky. Experimental and numerical investigation of cavitation in marine diesel injectors. *International Journal of Heat and Mass Transfer*, 169:120933, 2021.

[15] R. Balz, I. G. Nagy, G. Weisser, and D. Sedarsky. Experimental and numerical investigation of cavitation in marine diesel injectors. *International Journal of Heat and Mass Transfer*, 169:120933, 2021.

[16] Y. Bar-Sinai, S. Hoyer, J. Hickey, and M. P. Brenner. Learning data-driven discretizations for partial differential equations. *Proceedings of the National Academy of Sciences*, 116(31):15344–15349, 2019.

[17] J. Barker, P. Richards, C. Snape, and W. Meredith. Diesel injector deposits – an issue that has evolved with engine technology. *SAE Technical Papers*, 08 2011.

[18] M. Battistoni, D. Duke, A. Swantek, F. Tilocco, C. Powell, and S. Som. Effects of noncondensable gas on cavitating nozzles. *Atomization and Sprays*, 25:453–483, 01 2015.

[19] M. Battistoni, S. Som, and D. E. Longman. Comparison of Mixture and Multifluid Models for In-Nozzle Cavitation Prediction. *Journal of Engineering for Gas Turbines and Power*, 136(6):061506, 02 2014.

[20] M. Battistoni, S. Som, and C. F. Powell. Highly resolved eulerian simulations of fuel spray transients in single and multi-hole injectors: Nozzle flow and near-exit dynamics. *Fuel*, 251:709–729, 2019.

[21] C. Baumgarten. *Mixture Formation in Internal Combustion Engines.* Heat and Mass Transfer. Springer, Berlin, Heidelberg, 2006.

[22] Z. Bei, J. Wang, Y. Li, H. Wang, M. Li, F. Qian, and W. Xu. Challenges and solutions of ship power system electrification. *Energies*, 17(13), 2024.

[23] J. Bergstra, R. Bardenet, B. Kégl, and Y. Bengio. Algorithms for hyper-parameter optimization. In *25th Annual Conference on Neural Information Processing System*, 12 2011.

[24] W. Bick, M. Köhne, U. Pape, and H.-J. Schiffgens. The new deutz tier 41 engines. *MTZ worldwide*, 71(10):4–10, 2010.

[25] Z. Bilicki and J. Kestin. Physical aspects of the relaxation model in two-phase flow. *Proceedings of the Royal Society of London. A. Mathematical and Physical Sciences*, 428:379–397, 1990.

[26] S. Bond-Taylor, A. Leach, Y. Long, and C. G. Willcocks. Deep generative modelling: A comparative review of vaes, gans, normalizing flows, energy-based and autoregressive models. *IEEE Transactions on Pattern Analysis and Machine Intelligence*, 44(11):7327–7347, 2022.

[27] A. Bottega and C. Dongiovanni. Diesel spray macroscopic parameter estimation using a synthetic shapes database. *Applied Sciences*, 9(23), 2019.

[28] C. E. Brennen. *Cavitation and Bubble Dynamics.* Cambridge University Press, 2013.

[29] E. Briscoe and J. Feldman. Conceptual complexity and the bias/variance tradeoff. *Cognition*, 118(1):2–16, 2011.

[30] S. L. Brunton and J. N. Kutz. *Singular Value Decomposition (SVD)*, page 3–46. Cambridge University Press, 2019.

[31] F. Brusiani, S. Falfari, and P. Pelloni. Influence of the diesel injector hole geometry on the flow conditions emerging from the nozzle. *Energy Procedia*, 45:749–758, 2014. ATI 2013 - 68th Conference of the Italian Thermal Machines Engineering Association.

[32] J. Cao, Z. Liu, H. Shi, D. D. S. Kang, and L. Bu. A review of marine dual-fuel engine new combustion technology: Turbulent jet-controlled premixed-diffusion multi-mode combustion. *Energies*, 2025.

[33] T. Cao, Z. He, and J. Wang. Investigation of cavitation phenomenon with different fuel temperatures in diesel nozzles. *Advances in Mechanical Engineering*, 15(10):16878132231202867, 2023.

[34] T. Cao, Z. He, H. Zhou, W. Guan, L. Zhang, and Q. Wang. Experimental study on the effect of vortex cavitation in scaled-up diesel injector nozzles and spray characteristics. *Experimental Thermal and Fluid Science*, 113:110016, 2020.

[35] T. Cao and P. Qu. A review of cavitation phenomenon and its influence on the spray atomization in diesel injector nozzles. *SAE International Journal of Commercial Vehicles*, 17:67–89, 2024.

[36] W. Chapman, K. Gubbins, G. Jackson, and M. Radosz. Saft: Equation-of-state solution model for associating fluids. *Fluid Phase Equilibria*, 52:31–38, 1989.

[37] Z. Chen, Z. He, W. Shang, L. Duan, H. Zhou, G. Guo, and W. Guan. Experimental study on the effect of nozzle geometry on string cavitation in real-size optical diesel nozzles and spray characteristics. *Fuel*, 232:562–571, 2018.

[38] M. Chouak, L. Dufresne, and P. Seers. Large eddy simulation of a double-injection cycle and the impact of the needle motion on the sac-volume flow characteristics of a single-orifice diesel injector. *International Journal of Engine Research*, 22(8):2464–2476, 2021.

[39] P.-Y. Chuang and L. A. Barba. Experience report of physics-informed neural networks in fluid simulations: pitfalls and frustration. In *Proceedings of the 21st Python in Science Conference*, 2022.

[40] M. Coppo, F. Pinkert, C. Negri, and A. Hoppe. Detailed Characterisation and Service Experience of OMT Injectors for Dual-Fuel Medium- and Low-Speed Engines. In *29th CIMAC World Congress*, Vancouver, Canada, June 2016.

[41] D. Cowan. Bias-variance tradeoff. **url**: https://www.ml-science.com/bias-variance-tradeoff, 2016.

[42] M. Cristofaro, W. Edelbauer, P. Koukouvinis, and M. Gavaises. A numerical study on the effect of cavitation erosion in a diesel injector. *Applied Mathematical Modelling*, 78:200–216, 2020.

[43] A. Darwish and A. Nakhmani. Internal covariate shift reduction in encoder-decoder convolutional neural networks. In *Proceedings of the 2017 ACM Southeast Conference*, ACMSE '17, page 179–182, New York, NY, USA, 2017. Association for Computing Machinery.

[44] J. Deng, X. Wang, Z. Wei, L. Wang, C. Wang, and Z. Chen. A review of nox and sox emission reduction technologies for marine diesel engines and the potential evaluation of liquefied natural gas fuelled vessels. *Science of The Total Environment*, 766:144319, 2021.

[45] Y. Deng, X. Leng, W. Guan, Z. He, W. Long, S. Wei, and J. Hu. A numerical study on the in-nozzle cavitating flow and near-field atomization of cylindrical, v-type, and y-type intersecting hole nozzles using the les-vof method. *Green Processing and Synthesis*, 11(1):129–142, 2022.

[46] J. Dent. A basis for the comparison of various experimental methods for studying spray penetration. *Society of Automotive Engineers*, 1971.

[47] J. Desantes, R. Payri, F. Salvador, and A. Gil. Development and validation of a theoretical model for diesel spray penetration. *Fuel*, 85(7):910–917, 2006.

[48] J. M. Desantes, F. J. Salvador, M. Carreres, and J. Martínez-López. Large-eddy simulation analysis of the influence of the needle lift on the cavitation in diesel injector nozzles. *Proceedings of the Institution of Mechanical Engineers, Part D: Journal of Automobile Engineering*, 229(4):407–423, 2015.

[49] B. Dherin, M. Munn, M. Rosca, and D. G. Barrett. Why neural networks find simple solutions: the many regularizers of geometric complexity. In *Proceed-*

ings of the 36th International Conference on Neural Information Processing Systems, NIPS '22, Red Hook, NY, USA, 2022. Curran Associates Inc.

[50] G. Di Blasio, C. Beatrice, R. Ianniello, F. C. Pesce, A. Vassallo, G. Belgiorno, and G. Avolio. Balancing hydraulic flow and fuel injection parameters for low-emission and high-efficiency automotive diesel engines. *SAE International Journal of Advances and Current Practices in Mobility*, 2(2):638–652, 2020.

[51] B. Ding, H. Qian, and J. Zhou. Activation functions and their characteristics in deep neural networks. *2018 Chinese Control And Decision Conference (CCDC)*, pages 1836–1841, 2018.

[52] G. Dober, J.-M. Shi, N. Guerrassi, W. Bauer, and P. Aguado. Study of nozzle design impact on nozzle flow dynamics and spray formation in diesel injection using high resolution les and x-ray imaging. *Conference on Thermo- and Fluid Dynamic Processes in Direct Injection Engines*, 11 2016.

[53] P. Dong, K. Nishida, and Y. Ogata. Characterization of multi-hole nozzle sprays and internal flow for different nozzle hole lengths in direct-injection diesel engines. *Proceedings of the Institution of Mechanical Engineers, Part D: Journal of Automobile Engineering*, 231(4):500–515, 2017.

[54] L. Duan, S. qi Yuan, L. feng Hu, W. ming Yang, J. da Yu, and X. lan Xia. Injection performance and cavitation analysis of an advanced 250mpa common rail diesel injector. *International Journal of Heat and Mass Transfer*, 93:388–397, 2016.

[55] V. Dumoulin and F. Visin. A guide to convolution arithmetic for deep learning, 03 2016.

[56] K. Duraisamy, Z. J. Zhang, and A. P. Singh. New approaches in turbulence and transition modeling using data-driven techniques. In *53rd AIAA Aerospace Sciences Meeting*, 2015.

[57] ECN. Diesel data search page, September 2021.

[58] W. Edelbauer, J. Strucl, and A. Morozov. *Large Eddy Simulation of Cavitating Throttle Flow*. Springer Singapore, 2016.

[59] M. El Hannach, P. Ahmadi, L. Guzman, S. Pickup, and E. Kjeang. Life cycle assessment of hydrogen and diesel dual-fuel class 8 heavy duty trucks. *International Journal of Hydrogen Energy*, 44(16):8575–8584, 2019.

[60] EU. Commission regulation (eu) no 582/2011 of 25 may 2011 implementing and amending regulation (ec) no 595/2009 of the european parliament and of the council with respect to emissions from heavy duty vehicles (euro vi) and amending annexes i and iii to direct. *Official Journal of the European Union*, 2011.

[61] L. Fan, J. Xu, C. Chen, T. Tu, G. Lu, and B. Li. Performance study of an innovative dual injection mode injector for marine low-speed dual-fuel engine. *International Journal of Engine Research*, 26(6):811–825, 2025.

[62] D. J. G. Farlie. The performance of some correlation coefficients for a general bivariate distribution. *Biometrika*, 47(3-4):307–323, 12 1960.

[63] P. Fasching, F. Sprenger, and C. Granitz. A holistic investigation of natural gas–diesel dual fuel combustion with dual direct injection for passenger car applications. *Automotive and Engine Technology*, 2(16):79–95, 2019.

[64] Federal Ministry of Transport and Digital Infrastructure. *LNG as an alternative fuel for the operation of ships and heavy-duty vehicles*. The Herries Press, 2014.

[65] A. Foretich, G. G. Zaimes, T. R. Hawkins, and E. Newes. Challenges and opportunities for alternative fuels in the maritime sector. *Maritime Transport Research*, 2:100033, 2021.

[66] J.-P. Franc and J.-M. Michel. *Fundamentals of Cavitation*. Springer Dordrecht, 2004.

[67] L. Franceschini, D. Sipp, and O. Marquet. Mean-flow data assimilation based on minimal correction of turbulence models: Application to turbulent high reynolds number backward-facing step. *Phys. Rev. Fluids*, 5:094603, Sep 2020.

[68] M. Frank, D. Drikakis, and V. Charissis. Machine-learning methods for computational science and engineering. *Computation*, 8(1), 2020.

[69] K. Fukami, Y. Nabae, K. Kawai, and K. Fukagata. Synthetic turbulent inflow generator using machine learning. *Physical Review Fluids*, 4(6), 2019.

[70] M. Gavaises, A. Andriotis, D. Papoulias, N. Mitroglou, and A. Theodorakakos. Characterization of string cavitation in large-scale diesel nozzles with tapered holes. *Physics of Fluids*, 21, 05 2009.

[71] M. Gavaises, M. Murali-Girija, C. Rodriguez, P. Koukouvinis, M. Gold, and R. Pearson. Numerical simulation of fuel dribbling and nozzle wall wetting. *International Journal of Engine Research*, 23(1):132–149, 2022.

[72] M. Gavaises, D. Papoulias, A. A., and E. Giannadakis. Link between cavitation development and erosion damage in diesel injector nozzles. *SAE Technical Papers*, 04 2007.

[73] P. Geng, E. Cao, Q. Tan, and L. Wei. Effects of alternative fuels on the combustion characteristics and emission products from diesel engines: A review. *Renewable and Sustainable Energy Reviews*, 71:523–534, 2017.

[74] A. Geron. *Hands-On Machine Learning with Scikit-Learn, Keras, and TensorFlow: Concepts, Tools, and Techniques to Build Intelligent Systems*. O'Reilly Media, Inc., 2nd edition, 2019.

[75] H. GM, M. K. Gourisaria, M. Pandey, and S. S. Rautaray. A comprehensive survey and analysis of generative models in machine learning. *Computer Science Review*, 38:100285, 2020.

[76] E. Gomez Santos, J. Shi, M. Gavaises, C. Soteriou, M. Winterbourn, and W. Bauer. Investigation of cavitation and air entrainment during pilot injection in real-size multi-hole diesel nozzles. *Fuel*, 263:116746, 2020.

[77] R. Gramlich, P. Leick, J. Kaleta, A. Miller, T. Bossmeyer, G. Lamanna, D. Schmidt, I. Roisman, and C. Tropea. Air entrainment and momentum distribution in the near field of diesel sprays from group hole nozzles. *Proceedings of the 27th European Conference on Liquid Atomization and Spray Systems (ILASS)*, 09 2016.

[78] J. Gravesen. The metric of colour space. *Graphical Models*, 82:77–86, 2015.

[79] B. I. Grisci, M. J. Krause, and M. Dorn. Relevance aggregation for neural networks interpretability and knowledge discovery on tabular data. *Information Sciences*, 559:111–129, 2021.

[80] J. Gross and G. Sadowski. Perturbed-chain saft: An equation of state based on a perturbation theory for chain molecules. *Industrial & Engineering Chemistry Research*, 40(4):1244–1260, 2001.

[81] W. Guan, Z. He, L. Zhang, A. I. EL-Seesy, L. Wen, Q. Zhang, and L. Yang. Effect of asymmetric structural characteristics of multi-hole marine diesel injectors on internal cavitation patterns and flow characteristics: A numerical study. *Fuel*, 283:119324, 2021.

[82] W. Guan, Z. He, L. Zhang, G. Guo, T. Cao, and X. Leng. Investigations on interactions between vortex flow and the induced string cavitation characteristics in real-size diesel tapered-hole nozzles. *Fuel*, 287:119535, 2021.

[83] G. Guo, Z. He, Q. Wang, M.-C. Lai, W. Zhong, W. Guan, and J. Wang. Numerical investigation of transient hole-to-hole variation in cavitation regimes inside a multi-hole diesel nozzle. *Fuel*, 287:119457, 2021.

[84] H. Guo, R. Torelli, A. Bautista, A. Tekawade, B. Sforzo, C. Powell, and S. Som. Internal nozzle flow simulations of the ecn spray c injector under realistic operating conditions. *SAE International Journal of Advances and Current Practices in Mobility*, 2:2229–2240, 04 2020.

[85] K. Guo, Z. Tao, L. Zhang, B. Hu, and X. Kui. Generalize deep neural networks with adaptive regularization for classifying. *IEEE Transactions on Computational Social Systems*, 11(1):1216–1229, 2024.

[86] X. Guo, W. Li, and F. Iorio. Convolutional neural networks for steady flow approximation. In *Proceedings of the 22nd ACM SIGKDD International Conference on Knowledge Discovery and Data Mining*, KDD '16, page 481–490, New York, NY, USA, 2016. Association for Computing Machinery.

[87] A. Hassanzadeh, M. Bakhsh, and A. Dadvand. Numerical study of the effect of wall injection on the cavitation phenomenon in diesel injector. *Engineering Applications of Computational Fluid Mechanics*, 8, 07 2014.

[88] C. He, Y. Liu, L. Gan, and L. Lesshafft. Data assimilation and resolvent analysis of turbulent flow behind a wall-proximity rib. *Physics of Fluids*, 31(2):025118, 02 2019.

[89] Z. He, W. Guan, C. Wang, G. Guo, L. Zhang, and M. Gavaises. Assessment of turbulence and cavitation models in prediction of vortex induced cavitating flow in fuel injector nozzles. *International Journal of Multiphase Flow*, 157:104251, 2022.

[90] Z. He, G. Guo, X. Tao, W. Zhong, X. Leng, and Q. Wang. Study of the effect of nozzle hole shape on internal flow and spray characteristics. *International Communications in Heat and Mass Transfer*, 71:1–8, 2016.

[91] Z. He, Z. Zhang, G. Guo, Q. Wang, X. Leng, and S. Sun. Visual experiment of transient cavitating flow characteristics in the real-size diesel injector nozzle. *International Communications in Heat and Mass Transfer*, 78:13–20, 2016.

[92] Z. He, W. Zhong, Q. Wang, Z. Jiang, and Z. Shao. Effect of nozzle geometrical and dynamic factors on cavitating and turbulent flow in a diesel multi-hole injector nozzle. *International Journal of Thermal Sciences*, 70:132–143, 2013.

[93] Z. He, H. Zhou, L. Duan, M. Xu, Z. Chen, and T. Cao. Effects of nozzle geometries and needle lift on steadier string cavitation and larger spray angle in common rail diesel injector. *International Journal of Engine Research*, 22(8):2673–2688, 2021.

[94] A. Hegab, A. La Rocca, and P. Shayler. Towards keeping diesel fuel supply and demand in balance: Dual-fuelling of diesel engines with natural gas. *Renewable and Sustainable Energy Reviews*, 70:666–697, 2017.

[95] J. Helton and F. Davis. Latin hypercube sampling and the propagation of uncertainty in analyses of complex systems. *Reliability Engineering & System Safety*, 81(1):23–69, 2003.

[96] F. Hemez and S. Atamturktur. The dangers of sparse sampling for uncertainty propagation and model calibration. *Reliability Engineering and System Safety*, 3:537–556, 10 2011.

[97] H. Hiroyasu and M. Arai. Structures of fuel sprays in diesel engines. *Society of Automotive Engineers*, 02 1990.

[98] M. Hopp and J. Gross. Thermal conductivity from entropy scaling: A group-contribution method. *Industrial & Engineering Chemistry Research*, 58(44):20441–20449, 2019.

[99] B. Hu, Z. He, C. Li, Y. Deng, W. Guan, L. Zhang, and G. Guo. Study of the effect of cavitation flow patterns in diesel injector nozzles on near-field spray atomization characteristics using a les-vof method. *International Journal of Multiphase Flow*, 174:104791, 2024.

[100] W. Huang, S. Moon, Y. Gao, Z. Li, and J. Wang. Eccentric needle motion effect on near-nozzle dynamics of diesel spray. *Fuel*, 206:409–419, 2017.

[101] J. Hwang, P. Lee, S. Mun, I. Karathanassis, P. Koukouvinis, L. Pickett, and M. Gavaises. Machine-learning enabled prediction of 3d spray under engine combustion network spray g conditions. *Fuel*, 2021.

[102] C. Janiesch, P. Zschech, and K. Heinrich. Machine learning and deep learning. *Electronic Markets*, 31:685 – 695, 2021.

[103] T. Jeyaseelan, M. Son, T. Sander, and L. Zigan. Experimental and modeling analysis of the transient spray characteristics of cyclopentane at sub- and transcritical conditions using a machine learning approach. *Physics of Fluids*, 35, 08 2023.

[104] L. Jiang, L. Zhang, C. Li, and J. Wu. A correlation-based feature weighting filter for naive bayes. *IEEE Transactions on Knowledge and Data Engineering*, 31:201–213, 2019.

[105] T. Jin, C. Wang, A. Moro, A. Roell, X. Wu, and F. Luo. The influence of needle eccentric motion on injection and spray characteristics of a two-layered eight-hole diesel injector. *Proceedings of the Institution of Mechanical Engineers, Part D: Journal of Automobile Engineering*, 238(10-11):3308–3327, 2024.

[106] C. K. John, F. O. Ajibade, T. F. Ajibade, P. Kumar, O. G. Fadugba, and B. Adelodun. The impact of international agreements and government policies on collaborative management of environmental pollution and carbon emissions in the transportation sector. *Environmental Impact Assessment Review*, 114:107930, 2025.

[107] O. T. Kaario, S. Karimkashi, A. Bhattacharya, V. Vuorinen, M. Larmi, and X.-S. Bai. A comparative study on methanol and n-dodecane spray flames using large-eddy simulation. *Combustion and Flame*, 260:113277, 2024.

[108] H. Kaneko. Interpretation of machine learning models for data sets with many features using feature importance. *ACS Omega*, 8:23218 – 23225, 2023.

[109] I. Karathanassis, M. Heidari-Koochi, P. Koukouvinis, L. Weiss, P. Trtik, D. Spivey, M. Wensing, and M. Gavaises. Quantification of cavitating flows with neutron imaging. *Scientific Reports*, 14, 11 2024.

[110] I. Karathanassis, J. Hwang, P. Koukouvinis, L. Pickett, and M. Gavaises. Combined visualisation of cavitation and vortical structures in a real-size optical diesel injector. *Experiments in Fluids*, 62, 01 2021.

[111] G. Karim. *Dual-Fuel Diesel Engines*. CRC Press, 03 2015.

[112] M. D. Kass, Z. Abdullah, M. J. Biddy, C. Drennan, Z. Haq, T. Hawkins, S. Jones, J. Holliday, D. E. Longman, S. Menter, E. Newes, T. J. Theiss, T. Thompson, and M. Wang. Understanding the opportunities of biofuels for marine shipping. *Department of Energy's (DOE)*, 12 2018.

[113] T. Kavzoglu and P. Mather. The role of feature selection in artifial neural network applications. *International Journal of Remote Sensing - INT J REMOTE SENS*, 23:2919–2937, 08 2002.

[114] V. A. Kelkar, S. Bhadra, and M. Anastasio. Compressible latent-space invertible networks for generative model-constrained image reconstruction. *IEEE transactions on computational imaging*, 7:209 – 223, 2020.

[115] R. Keshari, M. Vatsa, R. Singh, and A. Noore. Learning structure and strength of cnn filters for small sample size training. In *2018 IEEE/CVF Conference on Computer Vision and Pattern Recognition*, pages 9349–9358, 2018.

[116] S. Khan, M. Masood, M. Medina, and F. Alzahrani. Advancing fuel spray characterization: A machine learning approach for directly injected gasoline fuel sprays. *Fuel*, 371:131980, 2024.

[117] A. Kilic, L. Schulze, and H. Tschöke. Influence of nozzle parameters on single jet flow quantities of multi-hole diesel injection nozzles. *SAE Technical Paper*, 2006.

[118] K. Kim, D. Kim, Y. Jung, and C. Bae. Spray and combustion characteristics of gasoline and diesel in a direct injection compression ignition engine. *Fuel*, 109:616–626, 2013.

[119] G. Kirolivanos and B. Jeong. Comparative reliability analysis and enhancement of marine dual-fuel engines. *Journal of International Maritime Safety, Environmental Affairs, and Shipping*, 6:1–23, 01 2022.

[120] J. Klimstra. 11 - fuel flexibility with dual-fuel engines. In J. Oakey, editor, *Fuel Flexible Energy Generation*, pages 293–304. Woodhead Publishing, Boston, 2016.

[121] C. P. Koci, R. P. Fitzgerald, V. Ikonomou, and K. Sun. The effects of fuel–air mixing and injector dribble on diesel unburned hydrocarbon emissions. *International Journal of Engine Research*, 20(1):105–127, 2019.

[122] K. Kolovos, N. Kyriazis, P. Koukouvinis, A. Vidal, M. Gavaises, and R. M. McDavid. Simulation of transient effects in a fuel injector nozzle using real-fluid thermodynamic closure. *Applications in Energy and Combustion Science*, 7:100037, 2021.

[123] P. Koukouvinis, M. Gavaises, J. Li, and L. Wang. Large eddy simulation of diesel injector including cavitation effects and correlation to erosion damage. *Fuel*, 175:26–39, 2016.

[124] P. Koukouvinis, H. Naseri, and M. Gavaises. Performance of turbulence and cavitation models in prediction of incipient and developed cavitation. *International Journal of Engine Research*, 18:333 – 350, 2017.

[125] P. Koukouvinis, C. Rodriguez, J. Hwang, I. Karathanassis, M. Gavaises, and L. Pickett. Machine learning and transcritical sprays: A demonstration study of their potential in ecn spray-a. *International Journal of Engine Research*, 23, 05 2021.

[126] P. Koukouvinis, A. Vidal-Roncero, C. Rodriguez, M. Gavaises, and L. Pickett. High pressure/high temperature multiphase simulations of dodecane injection to nitrogen: Application on ecn spray-a. *Fuel*, 275:117871, 2020.

[127] J. Kukacka, V. Golkov, and D. Cremers. Regularization for deep learning: A taxonomy. In *Sixth International Conference on Learning Representations*, 10 2017.

[128] A. Kumar, J. Nouri, and A. Ghobadian. Predictions of vortex flow in a diesel multi-hole injector using the rans modelling approach. *Fluids*, 6(12), 2021.

[129] A. Kumar, J. Nouri, and A. Ghobadian. Predictions of vortex flow in a diesel multi-hole injector using the rans modelling approach. *Fluids*, 6(12), 2021.

[130] P. Kundu, C. Xu, S. Som, J. Temme, C.-B. M. Kweon, S. Lapointe, G. Kukkadapu, and W. J. Pitz. Implementation of multi-component diesel fuel surrogates and chemical kinetic mechanisms for engine combustion simulations. *Transportation Engineering*, 3:100042, 2021.

[131] N. Kyriazis, P. Koukouvinis, and M. Gavaises. Numerical investigation of bubble dynamics using tabulated data. *International Journal of Multiphase Flow*, 93:158–177, 2017.

[132] L. Lamport. *Latex, A document preparation system.* Addison-Wesley, Reading, MA, 2^{nd} edition, 1994.

[133] E. Lemmon, M. Huber, and M. McLinden. Nist standard reference database 23: Reference fluid thermodynamic and transport properties-refprop, version 9.1, 2013-05-07 2013.

[134] Z. Li, K. Kamnitsas, and B. Glocker. Analyzing overfitting under class imbalance in neural networks for image segmentation. *IEEE Transactions on Medical Imaging*, 40(3):1065–1077, 2021.

[135] Z. Li, H. Zhang, S. C. Bailey, J. B. Hoagg, and A. Martin. A data-driven adaptive reynolds-averaged navier–stokes k–omega model for turbulent flow. *Journal of Computational Physics*, 345:111–131, 2017.

[136] C. Lin, P. Yang, Q. Wang, Z. Qiu, W. Lv, and Z. Wang. Efficient and accurate compound scaling for convolutional neural networks. *Neural Networks*, 167:787–797, 2023.

[137] J. Ling, A. Kurzawski, and J. Templeton. Reynolds averaged turbulence modelling using deep neural networks with embedded invariance. *Journal of Fluid Mechanics*, 807, 10 2016.

[138] F. Liu, Z. Li, Z. Wang, X. Dai, and C.-F. Lee. Dynamics of the in sac cavitating flow for diesel spray with split injection strategy. *International Journal of Engine Research*, 22(9):3062–3079, 2021.

[139] L. Liu, Y. Peng, D. Liu, C. Han, N. Zhao, and X. Ma. A review of phenomenological spray penetration modeling for diesel engines with advanced injection strategy. *International Journal of Spray and Combustion Dynamics*, 12:1756827720934067, 2020.

[140] L. Liu, Y. Peng, D. Liu, C. Han, N. Zhao, and X. Ma. A review of phenomenological spray penetration modeling for diesel engines with advanced injection strategy. *International Journal of Spray and Combustion Dynamics*, 12:1756827720934067, 2020.

[141] Y. Liu, J. Tian, Z. Song, F. Li, W. Zhou, and Q. Lin. Spray characteristics of diesel, biodiesel, polyoxymethylene dimethyl ethers blends and prediction of spray tip penetration using artificial neural network. *Physics of Fluids*, 34(1):015117, 01 2022.

[142] A. R. Lowe, B. Jasiok, V. V. Melent'ev, O. S. Ryshkova, V. I. Korotkovskii, A. K. Radchenko, E. B. Postnikov, M. Spinnler, U. Ashurova, J. Safarov, E. Hassel, and M. Chorazewski. High-temperature and high-pressure thermophysical property measurements and thermodynamic modelling of an international oil standard: Ravenol diesel rail injector calibration fluid. *Fuel Processing Technology*, 199:106220, 2020.

[143] A. Lozano-Durán and H. J. Bae. Machine learning building-block-flow wall model for large-eddy simulation. *Journal of Fluid Mechanics*, 963:A35, 2023.

[144] K. Lu, Y. Jin, Y. Chen, Y. Yang, L. Hou, Z. Zhang, Z. Li, and C. Fu. Review for order reduction based on proper orthogonal decomposition and outlooks of

applications in mechanical systems. *Mechanical Systems and Signal Processing*, 123:264–297, 2019.

[145] H. Luo, G. Zhang, F. Chang, Y. Jin, K. Ba, Y. Ogata, and K. Nishida. Comparisons in spray and atomization characteristics with/without hydro-erosive (he) grinding in nozzle orifice under non-evaporation and evaporation conditions. *Fuel*, 297:120789, 2021.

[146] O. Lötgering-Lin and J. Gross. Group contribution method for viscosities based on entropy scaling using the perturbed-chain polar statistical associating fluid theory. *Industrial & Engineering Chemistry Research*, 54(32):7942–7952, 2015.

[147] D. L. MacAdam. Visual sensitivities to color differences in daylight∗. *J. Opt. Soc. Am.*, 32(5):247–274, May 1942.

[148] K. Makri, R. Lockett, and M. Jeshani. Dynamics of post-injection fuel flow in mini-sac diesel injectors part 1: Admission of external gases and implications for deposit formation. *International Journal of Engine Research*, 22(4):1133–1153, 2021.

[149] A. Maniatopoulos and N. Mitianoudis. Learnable leaky relu (lelelu): An alternative accuracy-optimized activation function. *Information*, 12(12), 2021.

[150] J. Manin, L. Pickett, and K. Yasutomi. Stereoscopic high-speed microscopy to understand transient internal flow processes in high-pressure nozzles. *Experimental Thermal and Fluid Science*, 114:110027, 2020.

[151] V. Markov, B. Sa, V. Kamaltdinov, V. Neverov, and A. Zherdev. Investigation on the effect of the flow passage geometry of diesel injector nozzle on injection process parameters and engine performances. *Energy Science and Engineering*, 10, 01 2022.

[152] K. E. Matusik, D. J. Duke, A. L. Kastengren, N. Sovis, A. B. Swantek, and C. F. Powell. High-resolution x-ray tomography of engine combustion network diesel injectors. *International Journal of Engine Research*, 19(9):963–976, 2018.

[153] Q. Meng, Z. Jiang, and J. Wang. Artificial neural network-based subgrid-scale models for les of compressible turbulent channel flow. *Theoretical and Applied Mechanics Letters*, 13(1):100399, 2023.

[154] S. Mishra and R. Pradhan. Analyzing the impact of feature correlation on classification acuracy of machine learning model. *2023 International Conference on Artificial Intelligence and Smart Communication (AISC)*, pages 949–953, 2023.

[155] N. Mitroglou and M. Gavaises. Mapping of cavitating flow regimes in injectors for medium-/heavy-duty diesel engines. *International Journal of Engine Research*, 14(6):590–605, 2013.

[156] N. Mitroglou, M. McLorn, M. Gavaises, C. Soteriou, and M. Winterbourne. Instantaneous and ensemble average cavitation structures in diesel micro-channel flow orifices. *Fuel*, 116:736–742, 2014.

[157] C. Mohd Noor, M. Noor, and R. Mamat. Biodiesel as alternative fuel for marine diesel engine applications: A review. *Renewable and Sustainable Energy Reviews*, 94:127–142, 2018.

[158] S. Mondal, R. Torelli, B. Lusch, P. J. Milan, and G. M. Magnotti. Accelerating the generation of static coupling injection maps using a data-driven emulator. *SAE Technical Paper*, 2021.

[159] S. Moon, Y. Gao, S. Park, J. Wang, N. Kurimoto, and Y. Nishijima. Effect of the number and position of nozzle holes on in- and near-nozzle dynamic characteristics of diesel injection. *Fuel*, 150:112–122, 2015.

[160] S. Moon, W. Huang, Z. Li, and J. Wang. End-of-injection fuel dribble of multi-hole diesel injector: Comprehensive investigation of phenomenon and discussion on control strategy. *Applied Energy*, 179:7–16, 2016.

[161] S. Moon, W. Huang, and J. Wang. First observation and characterization of vortex flow in steel micronozzles for high-pressure diesel injection. *Experimental Thermal and Fluid Science*, 105:342–348, 2019.

[162] S. Moon, K. Komada, K. Sato, H. Yokohata, Y. Wada, and N. Yasuda. Ultrafast x-ray study of multi-hole gdi injector sprays: Effects of nozzle hole

length and number on initial spray formation. *Experimental Thermal and Fluid Science*, 68:68–81, 2015.

[163] S. Morgenthaler. Exploratory data analysis. *WIREs Computational Statistics*, 1(1):33–44, 2009.

[164] A. Moro, Q. Zhou, F. Xue, and F. Luo. Comparative study of flow characteristics within asymmetric multi hole vco and sac nozzles. *Energy Conversion and Management*, 132:482–493, 2017.

[165] N. Morozova, F. Trias, R. Capdevila, C. Pérez-Segarra, and A. Oliva. On the feasibility of affordable high-fidelity cfd simulations for indoor environment design and control. *Building and Environment*, 184:107144, 2020.

[166] F. Moukalled, L. Mangani, and M. Darwish. *The Finite Volume Method in Computational Fluid Dynamics: An Advanced Introduction with OpenFOAM® and Matlab®*. Springer Cham, 1st edition, 2015.

[167] J. D. Naber and D. L. Siebers. Effects of gas density and vaporization on penetration and dispersion of diesel sprays. *SAE transactions*, 105:82–111, 1996.

[168] M. Nagel, M. Fournarakis, Y. Bondarenko, and T. Blankevoort. Overcoming oscillations in quantization-aware training. In *Proceedings of the 39th International Conference on Machine Learning*, pages 16318–16330, 2022.

[169] M. Nagoaka, R. Ueda, R. Masuda, E. von Berg, and R. Tatschl. Modeling of diesel spray atomization linked with internal nozzle flow. *RD Review of Toyota CRDL*, 42(2):73–84, 2011.

[170] K. Najar, C. Fink, F. Pinkert, and H. Harndorf. A new spray penetration model developed for large engine diesel injectors. *ILASS – Europe 2014, 26th Annual Conference on Liquid Atomization and Spray Systems*, 10 2014.

[171] K. Najar, B. Stengel, F. Pinkert, B. Buchholz, and E. Hassel. Spray cone angle prediction model considering nozzle hole geometry. *ILASS – Europe 2019, 29th Annual Conference on Liquid Atomization and Spray Systems*, 09 2019.

[172] M. Nareklishvili, N. Polson, and V. Sokolov. Generative modeling: A review, 2025.

[173] F. Nargesian, H. Samulowitz, U. Khurana, E. Khalil, and S. D. Turaga. Learning feature engineering for classification. In *Proceedings of the Twenty-Sixth International Joint Conference on Artificial Intelligence*, pages 2529–2535, 08 2017.

[174] P. Ni, X. Wang, and H. Li. A review on regulations, current status, effects and reduction strategies of emissions for marine diesel engines. *Fuel*, 279:118477, 2020.

[175] I. A. Nikas, V. P. Georgopoulos, and V. C. Loukopoulos. Selective multistart optimization based on adaptive latin hypercube sampling and interval enclosures. *Mathematics*, 13(11):1733, 2025.

[176] B. M. Ningegowda, F. Nadia, F. Rahantamialisoa, A. Pandal, H. Jasak, H. Im, and M. Battistoni. Numerical modeling of transcritical and supercritical fuel injections using a multi-component two-phase flow model. *Energies*, 13:5676, 10 2020.

[177] B. M. Ningegowda, F. N. Z. Rahantamialisoa, A. Pandal, H. Jasak, H. G. Im, and M. Battistoni. Numerical modeling of transcritical and supercritical fuel injections using a multi-component two-phase flow model. *Energies*, 13(21), 2020.

[178] K. Nishida, J. Zhu, X. Leng, and Z. xia He. Effects of micro-hole nozzle and ultra-high injection pressure on air entrainment, liquid penetration, flame lift-off and soot formation of diesel spray flame. *International Journal of Engine Research*, 18:51 – 65, 2017.

[179] H. Nowruzi, H. Ghassemi, E. Amini, and I. Sohrabi-asl. Prediction of impinging spray penetration and cone angle under different injection and ambient conditions by means of cfd and anns. *Journal of the Brazilian Society of Mechanical Sciences and Engineering*, 39:3863–3880, 2017.

[180] O. Obiols-Sales, A. Vishnu, N. Malaya, and A. Chandramowliswharan. Cfdnet: a deep learning-based accelerator for fluid simulations. In *Proceedings of the*

34th ACM International Conference on Supercomputing, page 1–12. ACM, 2020.

[181] D. Panchigar, K. Kar, S. Shukla, R. Mathew, U. Chadha, and S. Selvaraj. Machine learning-based cfd simulations: a review, models, open threats, and future tactics. *Neural Computing and Applications*, 34, 09 2022.

[182] D. Paredi, T. Lucchini, G. D'Errico, A. Onorati, L. Pickett, and J. Lacey. Validation of a comprehensive computational fluid dynamics methodology to predict the direct injection process of gasoline sprays using spray g experimental data. *International Journal of Engine Research*, 21:199 – 216, 2020.

[183] J. Park, S. Lee, and D. Jeon. A neural network training processor with 8-bit shared exponent bias floating point and multiple-way fused multiply-add trees. *IEEE Journal of Solid-State Circuits*, PP:1–1, 08 2021.

[184] F. Payri, V. Bermúdez, R. Payri, and F. Salvador. The influence of cavitation on the internal flow and the spray characteristics in diesel injection nozzles. *Fuel*, 83(4):419–431, 2004.

[185] F. Payri, R. Payri, F. Salvador, and J. Martínez-López. A contribution to the understanding of cavitation effects in diesel injector nozzles through a combined experimental and computational investigation. *Computers & Fluids*, 58:88–101, 2012.

[186] R. Payri, J. García, F. Salvador, and J. Gimeno. Using spray momentum flux measurements to understand the influence of diesel nozzle geometry on spray characteristics. *Fuel*, 84(5):551–561, 2005.

[187] R. Payri, J. Gimeno, J. Cuisano, and J. Arco. Hydraulic characterization of diesel engine single-hole injectors. *Fuel*, 180:357–366, 2016.

[188] R. Payri, J. Gimeno, P. Martí-Aldaraví, and M. Martínez. Transient nozzle flow analysis and near field characterization of gasoline direct fuel injector using large eddy simulation. *International Journal of Multiphase Flow*, 148:103920, 2022.

[189] R. Payri, F. Salvador, G. Bracho, and A. Viera. Vapor phase penetration measurements with both single and double-pass schlieren for the same injection event. In *28th Conference on Liquid Atomization and Spray Systems*, 09 2017.

[190] R. Payri, J. Viera, V. Gopalakrishnan, and P. Szymkowicz. The effect of nozzle geometry over internal flow and spray formation for three different fuels. *Fuel*, 183:20–33, 11 2016.

[191] D.-Y. Peng and D. B. Robinson. A new two-constant equation of state. *Industrial & Engineering Chemistry Fundamentals*, 15(1):59–64, 1976.

[192] A. G. Perez, C. Coquelet, P. Paricaud, and A. Chapoy. Comparative study of vapour-liquid equilibrium and density modelling of mixtures related to carbon capture and storage with the srk, pr, pc-saft and saft-vr mie equations of state for industrial uses. *Fluid Phase Equilibria*, 440:19–35, 2017.

[193] F. Pinket, C. Negri, and A. Hoppe. Detailed characterisation and service experience of omt injectors for dual-fuel medium- and low-speed engines. *CIMAC Congress, Vancouver*, 2016.

[194] S. Posch, H. Winter, J. Zelenka, G. Pirker, and A. Wimmer. Development of a tool for the preliminary design of large engine prechambers using machine learning approaches. *Applied Thermal Engineering*, 191:116774, 2021.

[195] D. Potz, W. Christ, and B. Dittus, editors. *Diesel Nozzle - The determining interface betwwen injector system and combustion chamber*, Valencia, Spain, 2000. Springer.

[196] R. Prasetya, A. Sou, J. Oki, A. Nakashima, K. Nishida, Y. Wada, Y. Ueki, and H. Yokohata. Three-dimensional flow structure and string cavitation in a fuel injector and their effects on discharged liquid jet. *International Journal of Engine Research*, 22(1):243–256, 2021.

[197] R. H. Pratama, W. Huang, and S. Moon. Unveiling needle lift dependence on near-nozzle spray dynamics of diesel injector. *Fuel*, 285:119088, 2021.

[198] A. Prosperetti and G. Tryggvason, editors. *Computational Methods for Multiphase Flow*. Cambridge University Press, Cambridge, UK, 2007.

[199] M.-T. Puth, M. Neuhäuser, and G. D. Ruxton. Effective use of spearman's and kendall's correlation coefficients for association between two measured traits. *Animal Behaviour*, 102:77–84, 2015.

[200] S. Qazi, P. Venugopal, G. Rietveld, T. B. Soeiro, U. Shipurkar, A. Grasman, A. J. Watson, and P. Wheeler. Powering maritime: Challenges and prospects in ship electrification. *IEEE Electrification Magazine*, 11(2):74–87, 2023.

[201] T. Qiu, X. Song, Y. Lei, H. Dai, C. Cao, H. Xu, and X. Feng. Effect of back pressure on nozzle inner flow in fuel injector. *Fuel*, 173:79–89, 2016.

[202] A. Radford, L. Metz, and S. Chintala. Unsupervised representation learning with deep convolutional generative adversarial networks. In *4th International Conference on Learning Representations*, 11 2016.

[203] S. Rakshit and D. P. Schmidt. Simulating cavitating flow in fuel injector nozzles with an equilibrium-based model. *ILASS Americas - Annual Conference on Liquid Atomization and Spray Systems*, 07 2012.

[204] H. Rashidi, N. Tran, E. Betts, L. Howell, and R. Green. Artificial intelligence and machine learning in pathology: The present landscape of supervised methods. *Academic Pathology*, 6:237428951987308, 09 2019.

[205] J. L. Reboud, B. Stutz, and O. Coutier. Two phase flow structure of cavitation experiment and modeling of unsteady effects. *3rd Int. Sym. Cavitation*, 1998.

[206] C. Redtenbacher, C. Kiesling, A. Wimmer, F. Sprenger, P. Fasching, and H. Eichlseder. Dual fuel brennverfahren - ein zukunftsweisendes konzept vom pkw- bis zum großmotorenbereich? In H. Lenz, editor, *Tagungsband, 37. Internationales Wiener Motorensymposium*, volume Nr. 799, pages 403–428, Apr. 2016.

[207] C. Redtenbacher, F. Sprenger, and P. Fasching. Dual fuel brennverfahren – ein zukunftsweisendes konzept vom pkw- bis zum großmotorenbereich? *Internationales Wiener Motorensymposium, Vienna*, 2016.

[208] C. Redtenbachere, M. Kirsten, A. Wimmer, D. Imhof, I. Berger, and J. M. García-Oliver. Detailed assessment of an advanced wide range diesel injector for dual fuel operation of large engines. *CIMAC Congress, Helsinki*, 2016.

[209] R. Reitz and F. Bracco. Mechanisms of breakup of round liquid jets. *Encyclopedia of Fluid Mechanics*, 3, 01 1986.

[210] R. D. Reitz and F. V. Bracco. Mechanism of atomization of a liquid jet. *The Physics of Fluids*, 25(10):1730–1742, 10 1982.

[211] D. Rengasamy, J. M. Mase, A. Kumar, B. Rothwell, M. T. Torres, M. R. Alexander, D. A. Winkler, and G. P. Figueredo. Feature importance in machine learning models: A fuzzy information fusion approach. *Neurocomputing*, 511:163–174, 2022.

[212] B. Richards and N. Emekwuru. Prediction of spray vapor tip penetration of diesel, biodiesel and synthetic fuels using artificial neural networks with confidence intervals. *SAE Technical Paper*, 04 2023.

[213] C. Rodriguez, P. Koukouvinis, and M. Gavaises. Simulation of supercritical diesel jets using the pc-saft eos. *The Journal of Supercritical Fluids*, 145:48–65, 2019.

[214] C. Rodriguez, A. Vidal, P. Koukouvinis, M. Gavaises, and M. McHugh. Simulation of transcritical fluid jets using the pc-saft eos. *Journal of Computational Physics*, 374:444–468, 2018.

[215] A. Roskilly, R. Palacin, and J. Yan. Novel technologies and strategies for clean transport systems. *Applied Energy*, 157:563–566, 2015.

[216] A. Rubino, M. Pini, M. Kosec, S. Vitale, and P. Colonna. A look-up table method based on unstructured grids and its application to non-ideal compressible fluid dynamic simulations. *Journal of Computational Science*, 28:70–77, 2018.

[217] A. K. Runchal and M. M. Rao. *50 Years of CFD in Engineering Sciences: A Commemorative Volume in Memory of D. Brian Spalding*. Springer Singapore, 1^{st} edition, 2020.

[218] I. Ruoff, S. Reinhard, H.-J. Koch, and I. Brasowski. Simplified l'orange fuel injection system for dual fuel engines. Sir Henry Royce Awards for Technical Innovation, 2017.

[219] D. Sacha, M. Sedlmair, L. Zhang, J. A. Lee, J. Peltonen, D. Weiskopf, S. C. North, and D. A. Keim. What you see is what you can change:

Human-centered machine learning by interactive visualization. *Neurocomputing*, 268:164–175, 2017. Advances in artificial neural networks, machine learning and computational intelligence.

[220] M. Sadiq, S. W. Ali, Y. Terriche, M. U. Mutarraf, M. A. Hassan, K. Hamid, Z. Ali, J. Y. Sze, C.-L. Su, and J. M. Guerrero. Future greener seaports: A review of new infrastructure, challenges, and energy efficiency measures. *IEEE Access*, 9:75568–75587, 2021.

[221] J. Safarov, U. Ashurova, B. Ahmadov, E. Abdullayev, A. Shahverdiyev, and E. Hassel. Thermophysical properties of diesel fuel over a wide range of temperatures and pressures. *Fuel*, 216:870–889, 2018.

[222] Safiullah, K. Nishida, Y. Ogata, T. Oda, and K. Ohsawa. Effects of nozzle hole size and rail pressure on diesel spray and mixture characteristics under similar injection rate profile – experimental, computational and analytical studies under non-evaporating spray condition. *Proceedings of the Institution of Mechanical Engineers, Part D: Journal of Automobile Engineering*, 236(2-3):310–321, 2022.

[223] B. Sahoo, N. Sahoo, and U. Saha. Effect of engine parameters and type of gaseous fuel on the performance of dual-fuel gas diesel engines—a critical review. *Renewable and Sustainable Energy Reviews*, 13(6):1151–1184, 2009.

[224] F. Salvador, M. Carreres, D. Jaramillo, and J. Martínez-López. Analysis of the combined effect of hydrogrinding process and inclination angle on hydraulic performance of diesel injection nozzles. *Energy Conversion and Management*, 105:1352–1365, 2015.

[225] F. Salvador, M. Carreres, D. Jaramillo, and J. Martínez-López. Comparison of microsac and vco diesel injector nozzles in terms of internal nozzle flow characteristics. *Energy Conversion and Management*, 103:284–299, 2015.

[226] F. Salvador, J. De la Morena, G. Bracho, and D. Jaramillo. Computational investigation of diesel nozzle internal flow during the complete injection event. *Journal of the Brazilian Society of Mechanical Sciences and Engineering*, 40, 03 2018.

[227] F. Salvador, J. Martínez-López, M. Caballer, and C. De Alfonso. Study of the influence of the needle lift on the internal flow and cavitation phenomenon in diesel injector nozzles by cfd using rans methods. *Energy Conversion and Management*, 66:246–256, 2013.

[228] F. J. Salvador, J. Gimeno, J. Morena, and L. A. González-Montero. Experimental analysis of the injection pressure effect on the near-field structure of liquid fuel sprays. *Fuel*, 292:120296, 2021.

[229] C. F. G. D. Santos and J. a. P. Papa. Avoiding overfitting: A survey on regularization methods for convolutional neural networks. *ACM Comput. Surv.*, 54(10s), Sept. 2022.

[230] R. Saurel and C. Pantano. Diffuse-interface capturing methods for compressible two-phase flows. *Annual Review of Fluid Mechanics*, 50:105–130, 2018.

[231] J. Schmidhuber. Deep learning in neural networks: An overview. *Neural Networks*, 61:85–117, 2015.

[232] D. P. Schmidt and M. L. Corradini. The internal flow of diesel fuel injector nozzles: A review. *International Journal of Engine Research*, 2(1):1–22, 2001.

[233] G. H. Schnerr and J. Sauer. Physical and numerical modeling of unsteady cavitation dynamics. *ICMF, 4th International Conference on Multiphase Flow*, 05 2001.

[234] P. Schratz, J. Muenchow, E. Iturritxa, J. Cortés, B. Bischl, and A. Brenning. Monitoring forest health using hyperspectral imagery: Does feature selection improve the performance of machine-learning techniques? *Remote. Sens.*, 13:4832, 2020.

[235] T. Shan, W. Tang, X. Dang, M. Li, F. Yang, S. Xu, and J. Wu. Study on a poisson's equation solver based on deep learning technique. In *2017 IEEE Electrical Design of Advanced Packaging and Systems Symposium (EDAPS)*, 2017.

[236] P. Sharma, W. T. Chung, B. Akoush, and M. Ihme. A review of physics-informed machine learning in fluid mechanics. *Energies*, 16(5), 2023.

[237] J. Sharples. Lng supply chains and the development of lng as a shipping fuel in northern europe. *The Oxford Institute for Energy Studies*, 02 2019.

[238] J.-M. Shi, P. Aguado, E. Gomez Santos, N. Guerrassi, W. Bauer, M.-C. Lai, and J. Wang. High pressure diesel spray development: the effect of nozzle geometry and flow vortex dynamics. *Triennial International Conference on Liquid Atomization and Spray Systems*, 07 2018.

[239] Q. Shi, Y. Hu, and G. Yan. Fault diagnosis of me marine diesel engine fuel injector with novel ircmde method. *Polish Maritime Research*, 30:96–110, 10 2023.

[240] Z. Shi, C. Lee, H. Wu, H. Li, Y. Wu, L. Zhang, Y. Bo, and F. Liu. Effect of injection pressure on the impinging spray and ignition characteristics of the heavy-duty diesel engine under low-temperature conditions. *Applied Energy*, 262:114552, 2020.

[241] P. Singh. Systematic review of data-centric approaches in artificial intelligence and machine learning. *Data Science and Management*, 6(3):144–157, 2023.

[242] U. Sinha and B. Dindoruk. Review of physics-informed machine learning (piml) methods applications in subsurface engineering. *Geoenergy Science and Engineering*, 250:213713, 2025.

[243] G. Soave. Equilibrium constants from a modified redlich-kwong equation of state. *Chemical Engineering Science*, 27(6):1197–1203, 1972.

[244] S. Som, D. Longman, A. Ramirez, and S. Aggarwal. Influence of nozzle orifice geometry and fuel properties on flow and cavitation characteristics of a diesel injector. *Fuel Injection in Automotive Engineering*, 04 2012.

[245] S. Som, A. I. Ramirez, D. E. Longman, and S. K. Aggarwal. Effect of nozzle orifice geometry on spray, combustion, and emission characteristics under diesel engine conditions. *Fuel*, 90(3):1267–1276, 2011.

[246] N. Srivastava, G. E. Hinton, A. Krizhevsky, I. Sutskever, and R. Salakhutdinov. Dropout: a simple way to prevent neural networks from overfitting. *J. Mach. Learn. Res.*, 15:1929–1958, 2014.

[247] B. Stevens and T. Colonius. Enhancement of shock-capturing methods via machine learning. *Theoretical and Computational Fluid Dynamics*, 34(4):483–496, 2020.

[248] S. Stoumpos, G. Theotokatos, C. Mavrelos, and E. Boulougouris. Towards marine dual fuel engines digital twins—integrated modelling of thermodynamic processes and control system functions. *Journal of Marine Science and Engineering*, 8(3), 2020.

[249] A. Strokach and P. M. Kim. Deep generative modeling for protein design. *Current Opinion in Structural Biology*, 72:226–236, 2022.

[250] Z.-Y. Sun, G.-X. Li, C. Chen, Y.-S. Yu, and G.-X. Gao. Numerical investigation on effects of nozzle's geometric parameters on the flow and the cavitation characteristics within injector's nozzle for a high-pressure common-rail di diesel engine. *Energy Conversion and Management*, 89:843–861, 2015.

[251] R. Tahery and H. Modarress. Lennard-jones energy parameter for pure fluids from scaled particle theory. *Iranian Journal of Chemistry and Chemical Engineering (IJCCE)*, 26(2):1–8, 2007.

[252] E. Tahmasebi, T. Lucchini, G. D'Errico, A. Onorati, and G. Hardy. An investigation of the validity of a homogeneous equilibrium model for different diesel injector nozzles and flow conditions. *Energy Conversion and Management*, 154:46–55, 2017.

[253] Y. Tang, X. Zhao, J. Feng, S. Bai, G. Li, H. Duan, and S. Zhu. Challenges and opportunities of natural gas dual-fuel engines for marine applications. *Fuel*, 400:135808, 2025.

[254] A. Tekawade, B. Sforzo, K. Matusik, K. Fezzaa, A. Kastengren, and C. Powell. Time-resolved 3d imaging of two-phase fluid flow inside a steel fuel injector using synchrotron x-ray tomography. *Scientific Reports*, 10, 05 2020.

[255] A. Theodorakakos, G. Strotos, N. Mitroglou, C. Atkin, and M. Gavaises. Friction-induced heating in nozzle hole micro-channels under extreme fuel pressurisation. *Fuel*, 123:143–150, 2014.

[256] J. Tompson, K. Schlachter, P. Sprechmann, and K. Perlin. Accelerating Eulerian fluid simulation with convolutional networks. In D. Precup and Y. W. Teh,

editors, *Proceedings of the 34th International Conference on Machine Learning*, volume 70 of *Proceedings of Machine Learning Research*, pages 3424–3433. PMLR, 06–11 Aug 2017.

[257] L. Tong, J. Tianyu, S. Yu, W. Shaozhe, T. Dong, and F. Luo. Numerical research on influence of structural parameters of common-rail injector on injection rate of each nozzle hole. *Flow Measurement and Instrumentation*, 85:102158, 2022.

[258] R. Torelli, S. Som, Y. Pei, Y. Zhang, and M. Traver. Influence of fuel properties on internal nozzle flow development in a multi-hole diesel injector. *Fuel*, 204:171–184, 2017.

[259] B. Tracey, K. Duraisamy, and J. Alonso. Application of supervised learning to quantify uncertainties in turbulence and combustion modeling. In *51st AIAA Aerospace Sciences Meeting including the New Horizons Forum and Aerospace Exposition*, 01 2013.

[260] B. D. Tracey, K. Duraisamy, and J. J. Alonso. A machine learning strategy to assist turbulence model development. In *53rd AIAA Aerospace Sciences Meeting*, 2015.

[261] C. Tsonopoulos and J. Heidman. From redlich-kwong to the present. *Fluid Phase Equilibria*, 24(1):1–23, 1985.

[262] P. van Oostrum. Phancyhdr package documentation. **url**: http://texdoc.net/texmf-dist/doc/latex/fancyhdr/fancyhdr.pdf, 2004.

[263] A. Vardasbi, M. de Rijke, and M. Dehghani. Intersection of parallels as an early stopping criterion. *Proceedings of the 31st ACM International Conference on Information and Knowledge Management*, 2022.

[264] K. S. Varde, D. M. Popa, and L. K. Varde. Spray angle and atomization in diesel sprays. *SAE Transactions*, 93:779–787, 1984.

[265] T. Verdonck, B. Baesens, M. Óskarsdóttir, and S. vanden Broucke. Special issue on feature engineering editorial. *Machine Learning*, 113:1–12, 08 2021.

[266] H. Versteeg and W. Malalsekera. *An Introduction to Computational Fluid Dynamics The Finite Volume Method*. Pearson Education, 2^{nd} edition, 2007.

[267] A. Vidal, K. Kolovos, M. R. Gold, R. J. Pearson, P. Koukouvinis, and M. Gavaises. Preferential cavitation and friction-induced heating of multi-component diesel fuel surrogates up to 450mpa. *International Journal of Heat and Mass Transfer*, 166:120744, 2021.

[268] R. Vinuesa and S. L. Brunton. Enhancing computational fluid dynamics with machine learning. *Nature Computational Science*, 2(6):358–366, 2022.

[269] Y. Wakuri, M. Fujii, T. Amitani, and R. Tsuneya. Studies on the penetration of fuel spray in a diesel engine. *Bulletin of JSME*, 3(9):123–130, 1960.

[270] S. Wan, Y. Xia, L. Qi, Y.-H. Yang, and M. Atiquzzaman. Automated colorization of a grayscale image with seed points propagation. *IEEE Transactions on Multimedia*, 22(7):1756–1768, 2020.

[271] W. Wan, S. Mabu, K. Shimada, K. Hirasawa, and J. Hu. Enhancing the generalization ability of neural networks through controlling the hidden layers. *Applied Soft Computing*, 9(1):404–414, 2009.

[272] C. Wang, A. Moro, F. Xue, X. Wu, and F. Luo. The influence of eccentric needle movement on internal flow and injection characteristics of a multi-hole diesel nozzle. *International Journal of Heat and Mass Transfer*, 117:818–834, 2018.

[273] H. Watanabe, M. Nishikori, T. Hayashi, M. Suzuki, N. Kakehashi, and M. Ikemoto. Visualization analysis of relationship between vortex flow and cavitation behavior in diesel nozzle. *International Journal of Engine Research*, 16:5–12, 01 2014.

[274] K. Watanabe. High operation capable marine dual fuel engine with lng. *Marine Engineering*, 50(6):738–743, 2015.

[275] H. Wei, X. Chenand, W. Zhao, L. Zhouand, and R. Chen. Effects of the turbulence model and the spray model on predictions of the n-heptane jet fuel–air mixing and the ignition characteristics with a reduced chemistry mechanism. *Proceedings of the Institution of Mechanical Engineers, Part D: Journal of Automobile Engineering*, 231(14):1877–1888, 2017.

[276] S. Wei, Y. Li, S. Yan, J. Tian, Z. Yu, and Y. Wu. Review of prechamber turbulent jet ignition in marine engines using low-/zero-carbon fuels. *Journal of Marine Science and Application*, pages 1–32, 2025.

[277] S. E. Whang, Y. Roh, H. Song, and J. Lee. Data collection and quality challenges in deep learning: A data-centric AI perspective. *CoRR*, abs/2112.06409, 2021.

[278] Wikipedia contributors. Macadam ellipse – wikipedia, the free encyclopedia. https://en.wikipedia.org/wiki/MacAdam_ellipse, 2025. Accessed: 2025-06-29.

[279] O. Wilhelmsen, A. Aasen, G. Skaugen, P. Aursand, A. Austegard, E. Aursand, M. A. Gjennestad, H. Lund, G. Linga, and M. Hammer. Thermodynamic modeling with equations of state: Present challenges with established methods. *Industrial & Engineering Chemistry Research*, 56(13):3503–3515, 2017.

[280] T. Wu, X. Liu, W. An, Z. Huang, and H. Lyu. A mesh optimization method using machine learning technique and variational mesh adaptation. *Chinese Journal of Aeronautics*, 35(3):27–41, 2022.

[281] X. Wu, B. Xiang, H. Lu, C. Li, X. Huang, and W. Huang. Optimizing recurrent neural networks: A study on gradient normalization of weights for enhanced training efficiency. *Applied Sciences*, 2024.

[282] Wärtsilä. LNG Shipping Solutions. In *Wärtsilä*, 2017.

[283] Wärtsilä. Wärtsilä 34DF Product Guide. In *Wärtsilä*, 2020.

[284] J. Xia, Q. Zhang, J. Wang, Z. He, Q. Zhou, D. Zhou, Y. Qian, and X. Lu. Experimental study on the combustion and soot emission of twin-spray collision at various collision angles and injection pressures under marine engine's conditions. *International Journal of Engine Research*, 24(8):3783–3794, 2023.

[285] C.-N. Xiao, F. Denner, and B. G. van Wachem. Fully-coupled pressure-based finite-volume framework for the simulation of fluid flows at all speeds in complex geometries. *Journal of Computational Physics*, 346:91–130, 2017.

[286] F. Xie, Z. Liang, B. Cui, W. Guo, X. Li, B. Jiang, and Z. Jin. Spray-to-combustion interaction in hydrogen direct injection engines: Effects of injector structure and injection pressure. *Energy*, 333:137514, 2025.

[287] C. Xu, B. T. Cao, Y. Yuan, and G. Meschke. Transfer learning based physics-informed neural networks for solving inverse problems in engineering structures under different loading scenarios. *Computer Methods in Applied Mechanics and Engineering*, 405:115852, 2023.

[288] L. Yang, L. Wen, H. Zhang, G. Lu, et al. Analysis of injection characteristics and structural reliability of marine methanol fuel injectors. SAE Technical Paper 2025-01-7116, SAE International, 2025.

[289] S. Yang and C. Habchi. Real-fluid phase transition in cavitation modeling considering dissolved non-condensable gas. *Physics of Fluids*, 32(3):032102, Mar. 2020.

[290] S. Yang, P. Yi, and C. Habchi. Real-fluid injection modeling and les simulation of the ecn spray a injector using a fully compressible two-phase flow approach. *International Journal of Multiphase Flow*, 122:103145, 2020.

[291] S. Yarlanki, B. Rajendran, and H. Hamann. Estimation of turbulence closure coefficients for data centers using machine learning algorithms. In *13th InterSociety Conference on Thermal and Thermomechanical Phenomena in Electronic Systems*, pages 38–42, 2012.

[292] H. Yu, L. Goldsworthy, P. Brandner, J. Li, and V. Garaniya. Modelling thermal effects in cavitating high-pressure diesel sprays using an improved compressible multiphase approach. *Fuel*, 222:125–145, 2018.

[293] Y. Yu. Experimental study on effects of ethanol-diesel fuel blended on spray characteristics under ultra-high injection pressure up to 350 mpa. *Energy*, 186:115768, 2019.

[294] H. Zenil, N. A. Kiani, A. A. Zea, et al. Causal deconvolution by algorithmic generative models. *Nature Machine Intelligence*, 1:58–66, 2019.

[295] D. Zha, Z. P. Bhat, K.-H. Lai, F. Yang, Z. Jiang, S. Zhong, and X. Hu. Data-centric artificial intelligence: A survey. *ACM Comput. Surv.*, 57(5), Jan. 2025.

[296] C. Zhai, Y. Jin, K. Nishida, and Y. Ogata. Diesel spray and combustion of multi-hole injectors with micro-hole under ultra-high injection pressure – non-evaporating spray characteristics. *Fuel*, 283:119322, 2021.

[297] T. Zhang, T. Zhu, K. Gao, W. Zhou, and P. S. Yu. Balancing learning model privacy, fairness, and accuracy with early stopping criteria. *IEEE Transactions on Neural Networks and Learning Systems*, 34:5557–5569, 2021.

[298] W. Zhang, X. Li, L. Huang, and M. Feng. Experimental study on spray and evaporation characteristics of diesel-fueled marine engine conditions based on optical diagnostic technology. *Fuel*, 246:454–465, 2019.

[299] Y. Zhang, Y. Su, X. Li, F. Xie, Y. Wang, B. Shen, and M. Lang. Modeling of spray characteristics of alcohol fuels using response surface methodology and artificial neural networks. *Fuel*, 392:134936, 2025.

[300] Y. Zhang, Y. Su, X. Li, F. Xie, H. Yu, B. Shen, and M. Lang. Study and prediction on macroscopic characteristics of free spray of typical alcohol fuels through experimentation and the artificial neural network. *Energy*, 316:134610, 2025.

[301] Y. Zhang, G. Zhang, D. Wu, Q. Wang, E. Nadimi, P. Shi, and H. Xu. Parameter sensitivity analysis for diesel spray penetration prediction based on ga-bp neural network. *Energy and AI*, 18:100443, 2024.

[302] Z. Zhang and K. Duraisamy. Machine learning methods for data-driven turbulence modeling. In *22nd AIAA Computational Fluid Dynamics Conference*, 06 2015.

[303] Z. Zhang, Y. Wang, P. K. Jimack, and H. Wang. Meshingnet: A new mesh generation method based on deep learning. In *Lecture Notes in Computer Science*, pages 186–198, 06 2020.

[304] X. Zhao, L. Wang, Y. Zhang, X. Han, M. Deveci, and M. Parmar. A review of convolutional neural networks in computer vision. *Artificial Intelligence Review*, 57(4):99, 2024.

[305] X. Zhou and T. Li. Modeling of the entire processes of diesel spray tip penetration including the start- and end-of-injection transients. *Journal of the Energy Institute*, 98:271–281, 2021.

[306] A. Zunino, S. A. Bargal, P. Morerio, J. Zhang, S. Sclaroff, and V. Murino. Excitation dropout: Encouraging plasticity in deep neural networks. *International Journal of Computer Vision*, 129:1139 – 1152, 2018.

[307] P. Zwart, A. Gerber, and T. Belamri. A two-phase flow model for predicting cavitation dynamics. *ICMF, Fifth International Conference on Multiphase Flow*, 01 2004.

[308] E. Çabukoglu, G. Georges, L. Küng, G. Pareschi, and K. Boulouchos. Battery electric propulsion: An option for heavy-duty vehicles? results from a swiss case-study. *Transportation Research Part C: Emerging Technologies*, 88:107–123, 2018.

[309] F. Örley, S. Hickel, S. J. Schmidt, and N. A. Adams. Large-eddy simulation of turbulent, cavitating fuel flow inside a 9-hole diesel injector including needle movement. *International Journal of Engine Research*, 18(3):195–211, 2017.